The Effect of Diffusion Barriers, Stress and Lateral Diffusion on Thin-film Phase Formation

by

Hendrik S. de Waal

Dissertation submitted in partial fulfillment of the requirements for the degree of Doctor of Philosophy

(Physics)

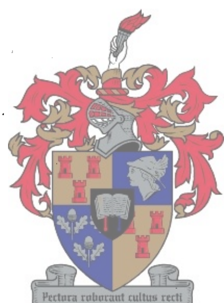

At the

University of Stellenbosch

Promoter: Prof. R. Pretorius

Co-Promoter: Dr. J. C. Lombaard

November 1999

Stellenbosch University https://scholar.sun.ac.za

Declaration

I, the undersigned, hereby declare that the work contained in this dissertation is my own original work and has not in its entirety or in part been submitted at any university for a degree.

Stellenbosch University https://scholar.sun.ac.za

Abstract

Instead of studying phase formation in conventional thin film binary diffusion couples, various unconventional thin film sample structures were used to investigate the influence of certain parameters on phase formation. Iron-silicide formation on Si(100) through metal alloy diffusion barriers, Ti-silicide formation on stressed Si(100) substrates and phase formation in various lateral diffusion couples was studied.

A variety of amorphous alloys were used as diffusion barriers through which Fe reacted with Si(100). It was found that the diffusion barrier did not change the effective concentration at the reaction interface enough to cause the formation of the semiconducting $\beta FeSi_2$ phase instead of $\varepsilon FeSi$ as first phase. There is much technical interest in growing the semiconducting $\beta FeSi_2$ phase epitaxially on Si(100) for use in amongst others infra red detectors and light emiting devices. The use of the diffusion barriers did however control the reaction in such a way as to allow the formation of a uniform film of polycrystalline $\beta FeSi_2$ at 800°C. In the case where Fe reacted directly with Si(100) without a diffusion barrier the Fe film reacted very non-uniformly with the substrate. The uniform polycrystalline thin film of $\beta FeSi_2$ was then converted to epitaxial $Fe_{0.5}Si$[CsCl] using a 0.8J/cm^2 laser pulse from an excimer laser. This was the first time that a continuous film of epitaxial $Fe_{0.5}Si$[CsCl] has been formed on Si(100). The $\beta FeSi_2$ films with large grain sizes formed the best quality epitaxial $Fe_{0.5}Si$[CsCl] after laser annealing. The grain size was dependant on the type of diffusion barrier used.

The influence of stress on Ti-silicide phase formation was also studied. $TiSi_2$ is commonly used in integrated circuits and with the move to smaller devices and linewidth's stress is playing a larger role. Varying amounts of compressive and tensile stress was induced in Si(100) substrates by depositing different thicknesses of SiO_2 or Si_3N_4 on the backside of the Si wafers. These back side films deformed the wafers causing stress throughout the substrates. The stress in the substrates was determined by measuring the radius of curvature of the samples using a laser technique and then relating the radius of curvature to stress using Stoney's equation. It was found that when Ti reacted with a substrate under compressive stress the Si diffusion process was slowed down so that $TiSi_2$[C49] grew 50% slower than when Ti reacted with substrates under tensile stress. In the samples with the most compressive stress in the substrate the Si diffusion was limited so effectively that the Ti-rich Ti_5Si_3 phase formed instead of $TiSi_2$. This is explained using the Effective Heat of Formation (EHF) model.

Lateral phase formation must take place in order to form some of the complex device structures present in the modern integrated circuit. In this study the nuclear microprobe, electron microscope and optical microscope was used to study phase formation in Ru-Al, Pt-Al and Cr-Si lateral diffusion couples. A typical lateral diffusion couple consisted of an island of one material deposited onto a thin film of another. It was found that if the island did not consist of the diffusing species there was no lateral reaction. In the aluminide systems the Al-island geometry always showed lateral reaction. In the Ru-Al system the Ru_4Al_{13} phase was the only phase to grow laterally with reaction limited kinetics while in the Pt-Al system two phases namely Pt_8Al_{21} and $PtAl_2$ grew laterally with diffusion limited kinetics. The EHF model is used to explain how diffusion limited growth causes the simultaneous formation of more than one phase. In the Cr-Si system the Si-island geometry grew laterally forming $CrSi_2$. Oxidation made it impossible to do any kinetic measurements. It is shown how lateral diffusion studies can be used to give information on diffusing species and diffusing mechanism. A summary of all the work done on lateral diffusion couples was also compiled in this study.

Stellenbosch University https://scholar.sun.ac.za

Opsomming

In teenstelling met die ondersoek van konvensionele dunlagie faseformasie is verskeie onkonvensionele dunlagie strukture gebruik om die invloed van sekere parameters op faseformasie te bestudeer. Ystersilisied formasie op Si(100) deur metaal allooi diffusie-versperringslagies, Ti-silisiedformasie op gespanne Si(100) substrate en faseformasie in verskeie laterale diffusie stelsels was bestudeer.

Verskeie amorfe allooie was gebruik as diffusie-versperringslagies waardeur Fe met Si(100) gereageer het. Daar is gevind dat die diffusie-versperringslagie nie die faseformasie op so 'n manier kon beinvloed dat $\beta FeSi_2$ as eerste fase sou vorm in plaas van $\varepsilon FeSi$. Daar is baie industriële belangstelling daarin om $\beta FeSi_2$ epitaksieël op Si(100) te groei vir gebruikstoepassings soos infra-rooi detektore en lig-stralende toestelle. Die gebruik van 'n diffusie-versperringslagie het wel die reaksie op so 'n manier beheer dat 'n uniforme lagie polikristallyne $\beta FeSi_2$ gevorm kon word by 800 °C. In die geval waar Fe direk met Si(100) gereageer het, het die Fe op 'n nie-uniforme wyse met die silikon substraat gereageer. Die uniforme polikristallyne $\beta FeSi_2$ lagie was toe omgesit na epitaksieël $Fe_{0.5}Si$[CsCl] deur die gebruik van 'n 0.8 J/cm^2 puls van 'n excimer laser. Dit is die eerste keer dat 'n ononderbroke lagie epitaksieël $Fe_{0.5}Si$[CsCl] gevorm is op Si(100). Die $\beta FeSi_2$ lagies met groot korrels het die beste gehalte epitaksieël $Fe_{0.5}Si$[CsCl] gevorm na die laserpuls. Die korrelgrootte was afhanklik van die tipe diffusie-versperringslagie wat gebruik was.

Die invloed van spanning op Ti-silisiedformasie was ook bestudeer. $TiSi_2$ is algemeen gebruik in geïntegreerde stroombane en met die neiging na kleiner lynwydtes en toestelgrotes speel spanning 'n al hoe groter rol. Verskillende hoeveelhede druk-en trekspanning is in Si(100) substrate geïnduseer deur middel van die deposisie van SiO_2 en Si_3N_4 op die agteroppervlak van die substrate. Die lagies wat op die agterkant gedeponeer is vervorm die Si sodat 'n spanningsveld ontstaan deur die substraat. Die spanning in die substrate is bepaal deur die meting van die krommingsstraal van die monster m.b.v. 'n laser tegniek. Die spanning kan afgelei word van die krommingstraal deur gebruik te maak van Stoney se vergelyking. As Ti gereageer het met 'n Si substraat wat onder drukspanning was, is die diffusieproses so vertraag dat die $TiSi_2$[C49] 50% stadiger gegroei het as wanneer Ti met Si substrate onder trekspanning gereageer het. In die monsters met die meeste drukspanning in die substraat is die Si diffusie so doeltrefend afgesny dat die Ti-ryke Ti_5Si_3 fase gevorm het in plaas van $TiSi_2$. Hierdie word verduidelik aan die hand van die Effective Heat of Formation (EHF) model.

Laterale faseformasie moet plaasvind om van die komplekse strukture te vorm wat op moderne geïntigreerde stroombaan bestaan. In hierdie ondersoek word die kernmikrosonde, elektron mikroskoop en optiese mikroskoop gebruik om faseformasie te bestudeer in die Ru-Al, Pt-Al and Cr-Si laterale diffusie sisteme. 'n Tipiese laterale diffusie monster bestaan uit eilande van een material gedeponeer op 'n dunlagie van 'n ander material. Daar is gevind dat indien die eilande nie die diffunderende spesie bevat nie, sal daar geen laterale faseformasie plaas vind nie. In al die aluminium sisteme het die aluminium eilande altyd laterale reaksie getoon. In die Ru-Al sisteem is dit gevind dat Ru_4Al_{13} die enigste fase is wat lateraal groei en dat die fase met reaksie-beperkte kinetika groei, terwyl in die Pt-Al sisteem twee fases lateraal groei (Pt_8Al_{21} en $PtAl_2$) met diffusie-beperkte kinetika. Die EHF model word gebruik om te verduidelik hoe diffusie beperkte groei aanleiding gee tot die gelyktydige formasie van meer as een fase. In die Cr-Si sisteem het net die monsters met Si-eilande laterale reaksie getoon. $CrSi_2$ was die enigste laterale fase om te vorm in die sisteem en oksidasie het dit onmoontlik gemaak om enige kinetiese metings te doen. Daar word gewys hoe laterale diffusiestelsels gebruik kan word om inligting te bepaal oor diffunderende spesies en diffusie meganisme. 'n Opsomming van al die werk gedoen op laterale diffusiestelsels is saamgevat in hierdie ondersoek.

Stellenbosch University https://scholar.sun.ac.za

Acknowledgements

A project like this never happens independently and I would like to bring special attention to the assistance provided by the following people.

1. Prof. R. Pretorius for providing the opportunity for this study and for the knowledgeable supervision of the project.
2. Dr. J. C. Lombaard for his valuable input and constant interest.
3. Dr. A. Vantomme (Catholic University Leuven, Belgium) for the very productive discussions concerning especially Mössbauer spectroscopy and the Fe-Si and Ti-Si systems.
4. Prof. C. M. Comrie for his assistance in all aspects of this project.
5. Ms. A. Steegen (IMEC, Belgium) for the manufacture of the stressed samples as well as the stress measurements.
6. Dr. Indira A. for her extreme patience with the co-deposition system and the fun chats we had.
7. Prof. K Bharuth-Ram and Mr. M. Moodley for the Mössbauer analysis.
8. Dr. C. C. Theron for the use of his *in-situ* real time RBS system.
9. The entire technical team of the Van de Graaff group who it sometimes seemed could get absolutely anything done.
10. The financial support from the bilateral agreement between Flanders and South Africa (bil 97/51) is greatly appreciated.
11. My fellow students and buddies in academia who know what its all about.
12. All the staff and collaborators at the Van de Graaff group of the National Accelerator Centre who worked with me through the years and made my time there the wonderful experience that it was.
13. My parents and close family for their continual support, patience and encouragement.

Stellenbosch University https://scholar.sun.ac.za

Table of Contents

1. Introduction and background **1**

1.1. Thin film technology 1

1.2. Kinetics of phase formation 1

1.3. Thermodynamics of phase formation 3

1.3.1. Phase formation sequence 3

1.3.2. Walser-Bene model 3

1.3.3. EHF model 4

1.4. Formation of epitaxial metal silicides 7

1.5. Scope of the investigation 10

2. Experimental **13**

2.1. Sample preparation and processing 13

2.1.1. Standard thin film structures 13

2.1.2. Lateral diffusion couples 14

2.1.3. Stressed structures 14

2.1.4. Films of compounds and alloys 15

2.1.5. Vacuum annealing 15

2.1.6. Laser annealing 16

2.2. Sample characterisation 16

2.2.1. X-ray diffraction 16

2.2.2. Rutherford Backscattering Spectrometry (RBS) 17

2.2.3. Nuclear Microprobe (NMP) 24

2.2.4. Scanning Electron Microscope (SEM) 24

2.2.5. Energy Dispersive Spectrometry (EDS) 26

2.2.6. Optical microscopy 27

2.2.7. Mössbauer Spectroscopy (MS) 28

2.2.8. Stress measurements in thin films 31

3. Fe-silicide formation from alloys and through diffusion barriers **33**

3.1. Introduction 33

3.2. Sample preparation 42

3.3. Effect of the Fe-V alloy composition in diffusion barriers 44

3.4. Effect of different alloys as diffusion barriers 47

3.5. Summary and conclusions 56

Stellenbosch University https://scholar.sun.ac.za

4. Effect of stress on $TiSi_2$ formation **60**
4.1. Introduction 60
4.2. Sample preparation and stress measurements 61
4.3. Kinetic measurements 64
4.3.1. *In situ* real time RBS 64
4.3.2. Conventional isothermal Anneals 67
4.3.3. XRD analysis 73
4.3.4. Effect of capping films on $TiSi_2$ formation 76
4.3.5. Discussion 78
4.4. Summary and conclusions 83

5. Ru-Al, Pt-Al and Cr-Si lateral diffusion couples **87**
5.1. Introduction 87
5.2. Ru-Al system 89
5.2.1. Thin film couples 89
5.2.2. Lateral diffusion couples 92
5.3. Pt-Al system 99
5.3.1. Thin film couples 99
5.3.2. Lateral diffusion couples 100
5.4. Cr-Si system 106
5.4.1. Thin film couples 106
5.4.2. Lateral diffusion couples 107
5.5. Summary and conclusion 118

6. Summary and conclusion **122**

Appendix A Stress calculations in thin films using Stoney's equation **129**
Appendix B X-ray and crystallographic data of phases **134**
Appendix C Standard Mössbauer parameters of Fe-silicide phases **133**
Appendix D Mechanical properties of some materials **138**

References **139**

Stellenbosch University https://scholar.sun.ac.za

1. INTRODUCTION AND BACKGROUND

1.1. Thin film technology

Layered thin film structures are the building blocks for technologies such as integrated circuits, solid state lasers and opto-electronic devices (e.g. photovoltaic cells). To create a transistor, diode or solid state laser thin films are grown on a semiconductor substrate. In integrated circuits thin metal films that are patterned into micron wide lines connect these semiconductor devices. In lasers and photovoltaic cells multilayer semiconductor structures are made which are sandwiched between metallic conductors. All these applications utilize the same thin film solid state technology. The study of thin film solid state interactions therefore plays an important role in the development of all these processes.

1.2. Kinetics of phase formation

A typical example of a thin film reaction couple is shown in **Fig. 1.1**. The thickness of the two thin films ranges from several hundred to several thousand angstroms. When the system is heated the materials in the two films (A and B) mix to form a chemical compound phase of a different composition ($A_{\alpha}B$). This could be an equilibrium compound phase, an amorphous phase or metastable phase. In thin film systems only one phase usually grows at a time and will continue to grow until one of the components has been consumed. During phase formation there are three processes which play an important role namely nucleation, reaction and diffusion. The process that is the slowest in a given system characterises the kinetics of the phase formation.

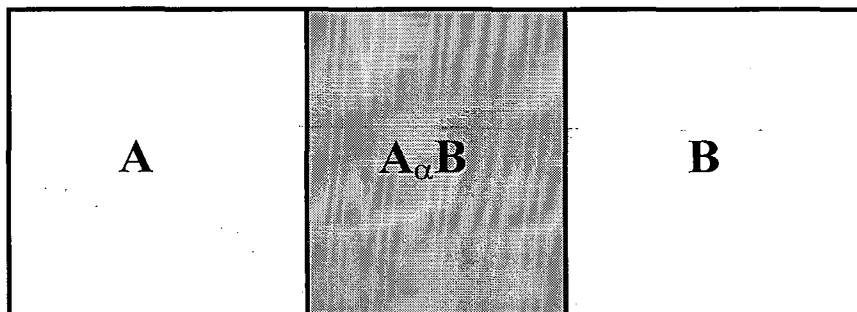

Fig. 1.1. Schematic representation of a thin film binary reaction couple. The two thin films composed of A and B respectively react to form a thin film of the $A_{\alpha}B$ phase. The thickness of A and B range from several hundred to several thousand angstroms.

Stellenbosch University https://scholar.sun.ac.za

Nucleation is the process whereby $A_\alpha B$ first forms at the A-B interface. At this point neither A nor B has to move in order to take part in the reaction. The phase will only nucleate if its formation causes a drop in free energy that is larger than the increase in surface energy, which results from the extra interface which is formed. In some systems there is a nucleation barrier which must first be overcome. The energy needed to overcome this barrier is the activation energy of nucleation and such systems are governed by so called nucleation-limited kinetics. Due to the high temperatures needed to overcome the nucleation barrier and initiate reaction in these systems subsequent phase growth is usually very fast.

The actual chemical reaction in which the new phase is formed occurs at one of the interfaces. Whether the $A/A_\alpha B$ or the $A_\alpha B/B$ interface is the actual reaction interface depends on whether A or B is the dominant diffusing species through the $A_\alpha B$ phase. If A is the dominant diffusing species for example there will be a movement of A atoms through the already formed $A_\alpha B$ film to the $A_\alpha B$-B interface where the combination of A and B atoms will occur. The relationship between the rate at which the $A_\alpha B$ phase increases in thickness and the time is dependent on whether the diffusion or the reaction is the slowest part of the phase formation process. The slower of the two processes will dominate the kinetics.

In the diffusion-limited case the kinetics is described by the simple phenomenological relation $x^2=k_Dt$, whereas in the reaction-limited case the relation is $x=k_Rt$. Here x is the thickness of the growing phase, t is the time and k_D and k_R are the respective rate constants. Both k_D and k_R have been experimentally found to be of the form $k_D=k_{D,0}exp(-E_D/k_BT)$ and $k_R=k_{R,0}exp(-E_R/k_BT)$. With $k_{D,0}$ and $k_{R,0}$ the respective pre-exponential factors, k_B Boltzmann's constant, T temperature and E_D and E_R the activation energies of diffusion and reaction respectively.

When the dependence of layer thickness to time has been measured at a constant temperature the kinetics of the system can be determined by plotting x versus $t^{1/2}$ and x versus t. If the x versus $t^{1/2}$ graph gives a straight line the kinetics is diffusion controlled or non-linear. If the kinetics is reaction controlled the second plot will give you a straight line graph (linear kinetics). In the non-linear case the gradient of the

Stellenbosch University https://scholar.sun.ac.za

$\ln(x^2/t)$ versus $1/k_BT$ curve gives the activation energy E_D. In the linear case the activation energy E_R can be extracted from the slope of the $\ln(x/t)$ versus $1/k_BT$ curve.

1.3. Thermodynamics of phase formation

1.3.1. Phase formation sequence

Binary equilibrium phase diagrams usually show several chemically stable equilibrium compound phases. In a bulk system any of these equilibrium phases could be produced given the correct composition pressure and temperature. If bulk pieces of two materials A and B were joined to form a bulk diffusion couple several and in some cases all the compound phases on the phase diagram would be present if the two materials were allowed to react with each other. A striking feature of phase formation in thin film diffusion couples (several hundred nanometers of material) is that usually only one compound phase grows at a time (say $A_{\alpha}B$). This phase then grows until one of the materials has been consumed (e.g. A). If there is still B left then this will react with the phase $A_{\alpha}B$ to form a new more B-rich phase $A_{\beta}B$. This will continue until either B or $A_{\alpha}B$ has been consumed. It is necessary to try and understand the actual mechanisms of interaction in these thin film systems in order to be able to forecast, which phases will form first and also what the subsequent phase formation sequence will be. In the thin film industry it is often desirable to form a second or third phase directly as a first phase. In order to manipulate phase formation the driving forces and influencing factors should be understood. The following thermodynamic models attempt to give the necessary tools to do this.

1.3.2. Walser-Bene′ model

One of the first rules for predicting phase formation was that of Walser and Bene′ [Wa-76] which stated: ***The first compound phase nucleated in planar binary reaction couples is the most stable congruently melting compound adjacent to the lowest temperature eutectic on the bulk equilibrium phase diagram.*** This rule was relatively successful in predicting first phase formation in metal silicon systems. It was later extended by Tsauer *et. al.* [Ts-81] to subsequent phase formation sequence

Stellenbosch University https://scholar.sun.ac.za

in metal-silicon systems. Their rule stated: ***The second phase formed is the compound with the smallest ΔT that exists in the phase diagram between the composition of the first phase and the un-reacted element.*** ΔT is defined as the temperature difference between the liquidus curve and the peritectic point (point where a solid breaks up into a liquid and a solid, both with new composition) of the phase. For so called congruently melting compounds ΔT is zero. Bene′ subsequently extended the Walser Bene′ rule to metal-metal reactions [Be-82] by relaxing the requirement that the first phase should be a congruently melting phase.

1.3.3. EHF model

A much more fundamental approach in predicting first phase formation was taken by Pretorius in 1984 [Pr-84] with a recent review article [Pr-93] giving an extensive description of the Effective Heat of Formation (EHF) model. The model shows how heats of formation when expressed as effective heats of formation ($\Delta H'$), can be used in conjunction with the composition of the lowest eutectic (or liquidus minimum) of the binary system, to predict both the first phase and subsequent phases which form. This model combines thermodynamics with the availability or effective concentration of the elements at the interface.

Since thin film reactions occur in the solid state the Gibbs free energy can be approximated by the standard enthalpy of reaction alone, as the change in entropy may be considered to be close to zero for the majority of systems. Therefore $\Delta G_T^0 \approx \Delta H_{298}^0$.

According to the Neumann-Kopp rule [Ku-79] the standard values (T=298 K) of enthalpy and entropy in solids can be used for thermodynamic calculations at any temperature. An effective heat of formation [Pr-93] is defined as

$$\Delta H' = \Delta H^0 \times \left(\frac{\text{effective concentration of limiting element}}{\text{compound concentration of limiting element}} \right) \qquad (1.1)$$

Where $\Delta H'$ and ΔH^0 are expressed in kJ per mole of atoms. For example if the effective concentration at the interface was 18 at % Si and formation of CrSi is

Stellenbosch University https://scholar.sun.ac.za

considered, then Si would be the limiting species. If ΔH^0 = -30.2 kJ per mole of atoms for CrSi then:

$$\Delta H' = -30.2\left(\frac{0.18}{0.50}\right) = -10.87 \text{ kJ (mole. at)}^{-1}$$

From equation (1.1) it can be seen that there is a linear relationship between the effective heat of formation (or heat released) and the concentration of the limiting element. Using this approach a heat of formation diagram can be drawn for any binary system (see **Fig. 1.2**).

From the model the following rule to predict first phase formation has been formulated: ***The first silicide phase to form during metal-silicon interaction is the congruent phase with the most negative effective heat of formation ($\Delta H'$) at the concentration of the lowest eutectic temperature of the binary system [Pr-84].*** The effective heat of formation rule is extended to incorporate phase sequence by stating that: ***After first phase silicide formation, the next phase formed at the interface between the compound and the remaining element is the next congruent phase richer in the unreacted element, which has the most negative effective heat of formation. If the compounds between a formed phase and the remaining element are all non-congruent, the next phase that will form is the non-congruent phase with the most negative effective heat of formation [Pr-93].*** In the case of metal-metal systems the constraint of congruency is dropped because in metal-metal systems both congruent and non-congruent phases usually form.

The EHF model has been successfully used in metal-metal, metal-silicon and metal-germanium systems to predict first phase formation as well as phase formation sequence [Pr-93]. As an example **Table 1.1** shows that according to equilibrium thermodynamics Cr_5Si_3 could be expected to form as the first phase as it has the most negative standard heat of formation -35.0 kJ(mol at.)$^{-1}$. Experimentally in thin film systems however $CrSi_2$ is found to form first [Pr-93], which corresponds to the lowest effective heat of formation of -13.95 kJ(mol at.)$^{-1}$ which was calculated with the effective concentration as that at the liquidus minimum.

Stellenbosch University https://scholar.sun.ac.za

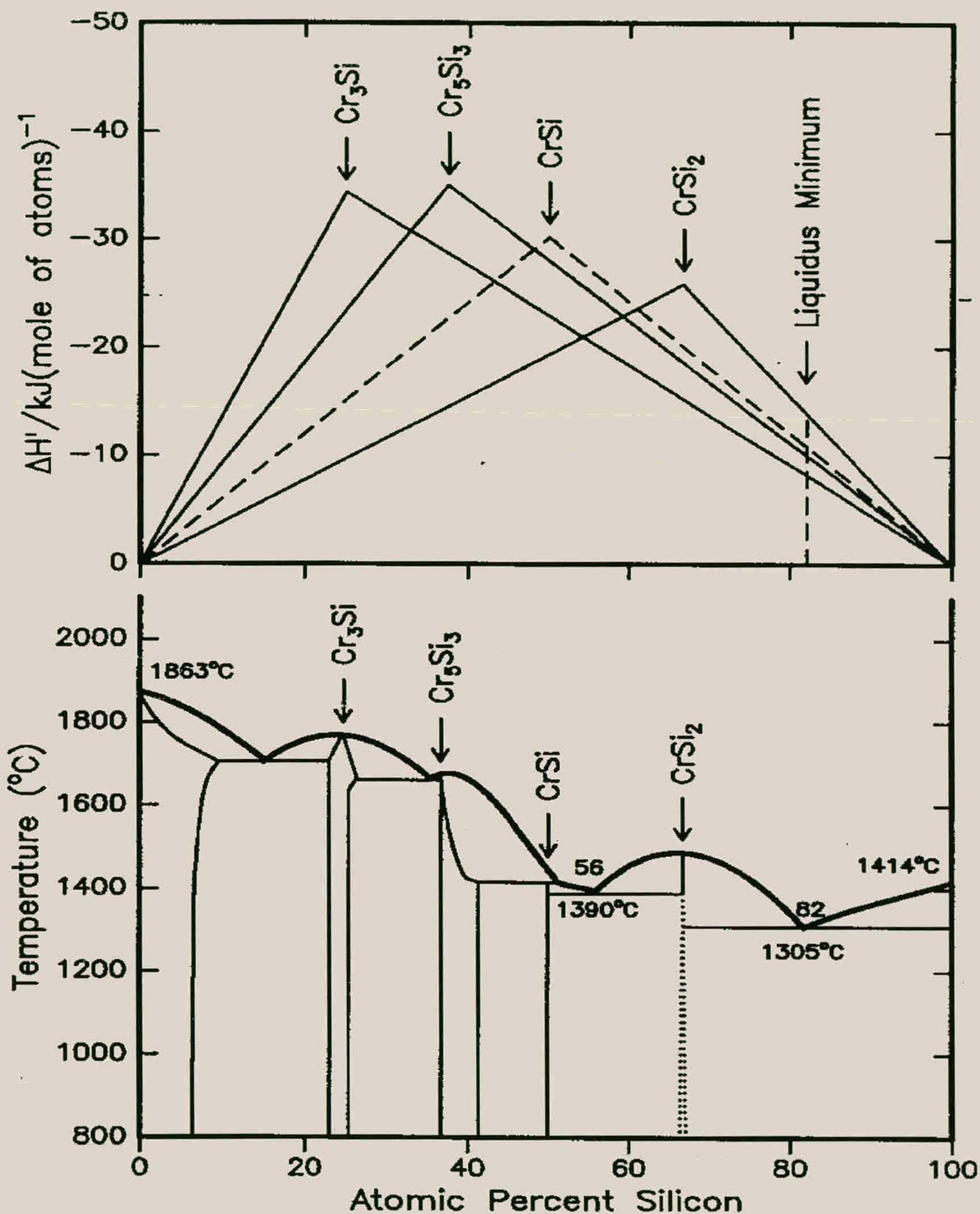

Fig. 1.2 Phase diagram plus EHF diagram of the Cr-Si system showing linear relationship between effective heat of formation (or heat released) and the concentration of the limiting element

Stellenbosch University https://scholar.sun.ac.za

Table 1.1 *Showing comparison between normal and effective heats of formation for the Cr-Si system. The underlined is experimentally found as first phase.*

Phase	Congruency	Composition	ΔH^0 (kJ(mol at.)$^{-1}$)	Limiting Element	$\Delta H'$ (kJ(mol at.)$^{-1}$)
liquidus minimum		$Cr_{0.180}Si_{0.820}$			
Cr_3Si	C	$Cr_{0.75}Si_{0.250}$	-34.4	Cr	-8.26
Cr_5Si_3	C	$Cr_{0.625}Si_{0.375}$	-35.0	Cr	-10.08
CrSi	NC	$Cr_{0.500}Si_{0.500}$	-30.2	Cr	-10.87
$CrSi_2$	C	$Cr_{0.333}Si_{0.667}$	-25.8	Cr	-13.95

1.4. Formation of epitaxial metal silicides

Epitaxial growth occurs when the atoms in the silicide are aligned with the atoms in the underlying single crystal Si substrate. Epitaxial films are used in a variety of applications including semiconductor devices, detectors, optical electronics (e.g. photovoltaics) and light sources (e.g. solid state lasers). Homoepitaxy is the term used when the epitaxial film is grown on a substrate of the same material (e.g. p or n type Si on intrinsic silicon substrates in photovoltaics). Heteroepitaxy is the term used when the thin film and substrate are different materials (e.g. any silicide forming on a silicon substrate). **Fig. 1.3** shows a list of silicides that can be grown epitaxially on silicon. The lattice match η is very important in determining if a silicide will grow epitaxially or not and is defined as

$$\eta=(a_{silicide}-a_{Si})/a_{Si}$$

where $a_{silicide}$ is the lattice parameter of the crystalline plane of the silicide that is being latticed matched to the silicon and a_{Si} is the lattice parameter of the silicon substrate.

Stellenbosch University https://scholar.sun.ac.za

For good quality epitaxial growth the lattice mismatch should not be more than a few percent. **Fig. 1.4** shows the lattice mismatch that various transition metal silicides will encounter if they were grown on silicon (100), (110) and (111). The silicides with small unit cell areas and small lattice mismatches (e.g. $NiSi_2$ and $CoSi_2$) are easiest to grow epitaxially and form high quality silicides. Epitaxial thin films tend to grow in a number of different orientations with respect to the different silicon substrates. A and B type $NiSi_2$ and $CoSi_2$ (CaF_2 structure) grown epitaxially on Si<100> are good examples of this. A type is a continuation of the Si lattice planes whereas B type results from a single stacking fault caused by a 180° rotation of the silicide with respect to the substrate.

	22 Ti $TiSi_2$ 13 ortho	23 V VSi_2 50 hex	24 Cr $CrSi_2$ 0.35* hex 0.13	25 Mn $MnSi_{1.7}$ 0.5* tetr 1.8	26 Fe β-$FeSi_2$ 0.85* ortho 1.4	α-$FeSi_2$ 250 tetr 0.7	27 Co $CoSi_2$ 14 cub -1.2	28 Ni $NiSi_2$ 50 cub -0.4
39 Y YSi_{1-x} 50 hex 0.0	40 Zr $ZrSi_2$ 100 ortho	41 Nb $NbSi_2$ 50 hex	42 Mo $MoSi_2$ 90 hex				45 Rh Rh_3Si_4 ortho	46 Pd Pd_2Si 30 hex
60 Er $ErSi_{1.7}$ 35 hex -1.2		73 Ta $TaSi_2$ 45 hex	74 W WSi_2 70 hex	75 Re $ReSi_2$ 0.13* tetr 0.2	76 Os $OsSi_2$ 1.8* ortho	77 Ir $IrSi_{1.7}$ 1.2* mono	77 Ir $IrSi_3$ 400 hex	78 Pt $PtSi$ 30 ortho

*band gap (eV)
lattice mismatch (%)
electrical resistivity ($\mu\Omega$ cm)

Fig. 1.3 Crystal structures, lattice mismatches and electrical resistivities of selected metallic silicides that grow epitaxially on silicon [Ma-95].

Stellenbosch University https://scholar.sun.ac.za

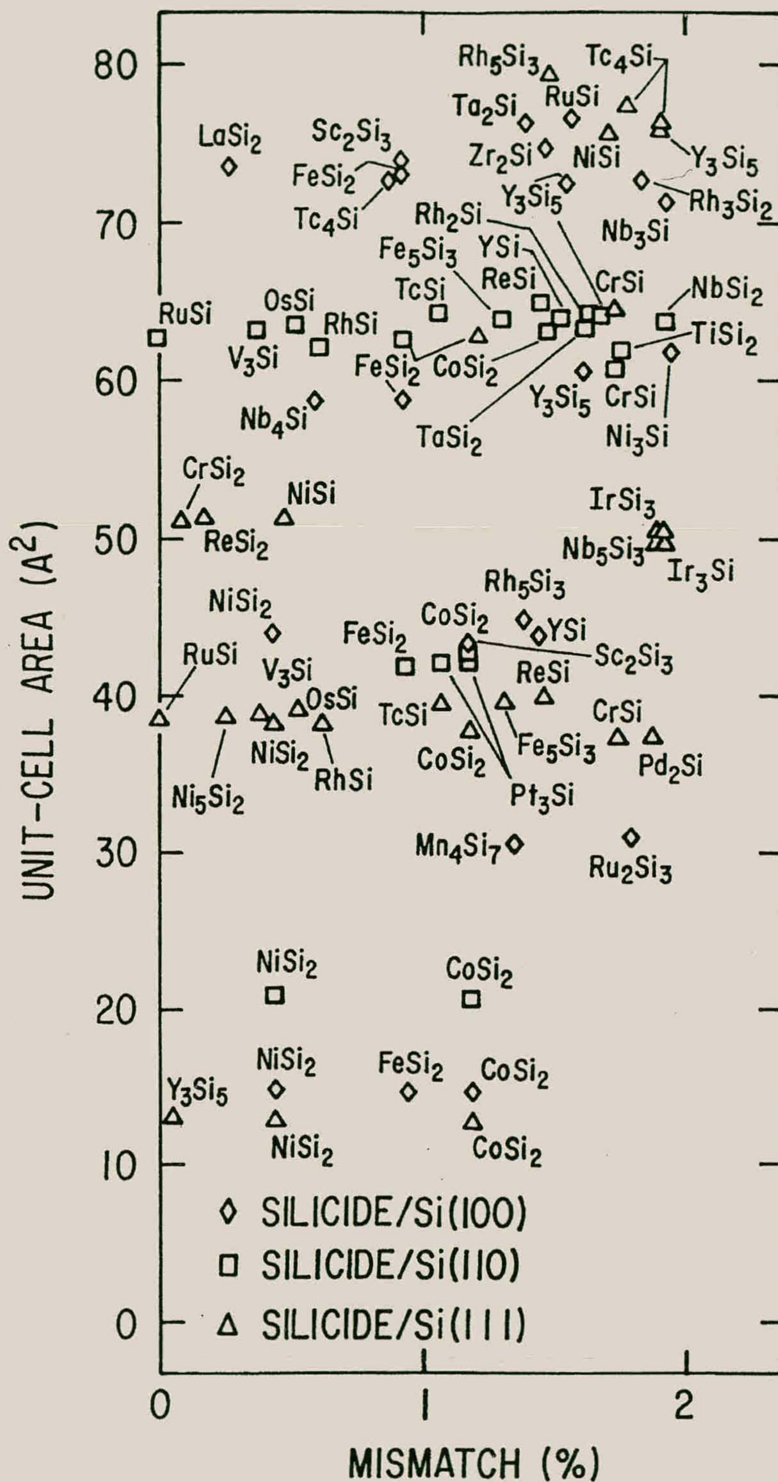

Fig. 1.4 Lattice mismatches of transition metal silicides on silicon (100), (110) and (111) at room temperature.

UNIVERSITEITSBIBLIOTEEK U. S.

Stellenbosch University https://scholar.sun.ac.za

1.5. Scope of the investigation

The main aim of this investigation was to improve the basic understanding of phase formation by solid state interaction in thin film structures. Solid state phase formation through diffusion barriers, the effect of stress on phase formation and phase formation in lateral diffusion couples was studied. The results were discussed in terms of the effective heat of formation model, which describes phase formation in terms of thermodynamics and the effective concentration of the reactants at the growth interface. The samples studied consisted of a variety of metallic thin film structures deposited onto Si substrates. The depositions were done using various vacuum deposition techniques including electron beam deposition and Molecular Beam Epitaxy (MBE). Reaction was usually induced in the samples by annealing in a vacuum furnace at pressures below 2×10^{-7} Torr. This was done to limit oxidation or any other forms of contamination. In some cases an excimer laser was used to irradiate samples with a laser pulse. This is a useful highly non-equilibrium heating technique that can be used to induce the system into forming metastable phases. Rutherford Backscattering Spectrometry (RBS) with 2 MeV alpha particles was used to study the composition of the thin films. This could also be carried out in the Nuclear Microprobe (NMP) in scanning mode to give composition and depth information as a function of lateral position. RBS was also done in channeling mode to study the epitaxiality of the silicide films. X-ray Diffraction (XRD) was used to identify crystallographic phases and Conversion Electron Mössbauer Spectroscopy (CEMS) was used to identify the various Fe-silicide phases. Imaging of the samples was also done using optical and scanning electron microscopes. These characterisation and sample preparation techniques are discussed in **Chapter 2**.

The growth of uniform epitaxial Fe-silicides on Si(100) as substrate is discussed in **Chapter 3**. Different Fe-M alloys (M=V, Cr, Ti and Ni) were used as either diffusion barriers (100 Å) through which the iron reacted with the silicon or as reactant from which the iron (500 Å thin-films) was supplied for the silicide formation. These results were compared with the case where Fe was reacted directly with the Si(100) substrate. Diffusion barriers have been used successfully in other systems to grow uniform silicides on silicon substrates. A Ti diffusion barrier for example has been used to form epitaxial $CoSi_2$ directly as first phase [La-91] instead of Co_2Si which is

Stellenbosch University https://scholar.sun.ac.za

usually found as first phase. A Ni-Zr alloy has also been used between Ni and Si to form $NiSi_2$ as first phase instead of Ni_2Si [Pr-97]. In both these cases the success was because the diffusion barrier caused the effective concentration at the interface to change such that another phase became thermodynamically more viable. This process is called Concentration Controlled Phase Selection. This means that a phase with a good crystal match with silicon can be formed directly on the substrate and not only after another phase has already formed. In other cases the diffusion barrier does not influence the phase sequence but rather the supply of one of the reacting species in such a way that the film grown through the barrier is more uniform than films grown directly on silicon [Ky-94, Ch-85].

Chapter 4 deals with the effect of stress on Ti-silicide formation. The Ti was deposited onto stressed Si substrates and then annealed to induce reaction. The stress in the substrates varied from compressive to tensile and was induced by depositing varying thicknesses of different materials onto the back side of the substrates. The back side films caused the samples to curve due to differences in thermal expansion coefficients resulting in strain and therefore stress in the front side of the samples. An optical technique was used to measure the curvature of the samples and this could be related to the stress using Stoney's equation. After the Ti films were deposited and stress measurements carried out the samples were annealed at temperatures ranging from 450 to 650 ^{o}C. The samples were then analised using XRD for phase identification and RBS to determine the kinetics of the phases. The phase formation and kinetics were then compared as a function of stress. Al_2O_3 and Ti-oxide capping films were used in an attempt to limit oxidation, which was a continual problem. It was found that the Ti-oxide cap was the most effective as it seemed to act as a gettering site for any oxygen in the system.

The Cr-Si, Pt-Al and Ru-Al lateral diffusion systems are discussed in detail in **Chapter 5**. The lateral diffusion couples consisted of islands of one material deposited onto a thin film of the other. The NMP was used in the RBS mode to do phase identification and the optical and electron microscopes were used to measure the kinetics of the lateral grown phases. A literature search was carried out on lateral diffusion systems and the results summarised and discussed.

Stellenbosch University https://scholar.sun.ac.za

The summary of the important results obtained in this study is contained in **Chapter 6.** All the experimental work was focused on factors affecting phase formation. In this chapter the conclusions that can be derived from the effect of diffusion barriers, stress and lateral diffusion on phase formation are discussed in terms of the EHF model.

Stellenbosch University https://scholar.sun.ac.za

2. EXPERIMENTAL

2.1. Sample preparation and processing

Commercial Si wafers were used as substrates whether silicide reactions were being studied or not. Si wafers offer a firm, clean substrate with a relatively low mass making it favorable for RBS analyses. The deposited metals are mostly heavier than Si and can therefore easily be resolved. The silicon wafers could be made chemically inert to many materials by forming a film of amorphous SiO_2 on the surface. Metal films are then deposited onto the SiO_2 buffer layer when intermetallic reactions need to be studied. The substrates were degreased using organic solvents and etched with HF acid before being placed in a vacuum deposition chamber. The actual deposition technique and process was dependant on the desired sample structure.

2.1.1. Standard thin film structures

Blanket mono elemental thin film structures were deposited using a variety of techniques. They included chemical vapor deposition, electron beam vacuum deposition, sputtering and molecular beam epitaxy. These techniques were not all available at our lab and therefore some samples were made at other institutes. The films were deposited sequentially to obtain the desired structure. The majority of samples used in this study were made in two electron beam vacuum deposition systems. Both systems were fitted with rotary roughing pumps and turbo molecular pumps that could pump the deposition chamber down to below 10^{-5} Torr. A set of six ionisation pumps and a liquid nitrogen cold trap in the one system and a cryopump in the other system then took the pressure down to below 10^{-7} Torr. The pressure during evaporation was in the low 10^{-7} Torr range. Evaporation was accomplished by electron beam melting the materials in a water-cooled copper crucible. In the co-evaporator system up to three elements could be evaporated at the same time and the relative deposition rates determined the composition of the deposited thin film. The depositions were controlled using INFICON deposition controllers that automatically controlled the output power from the power supplies to the electron guns while monitoring the deposition rates, which were measured using crystal thickness monitors.

Stellenbosch University https://scholar.sun.ac.za

2.1.2. Lateral diffusion couples

These structures consist of an island of one material deposited onto a thin film of another. The thin film is deposited as a blanket film onto a SiO_2 coated Si wafer using e-beam vacuum deposition (several hundred angstroms). The island is then deposited onto the blanket film by depositing the material through a silicon mask that has rectangular holes in it (400×800 μm).

2.1.3. Stressed structures

There are three forms of stress in thin film structures namely thermal, coherency and intrinsic stress. Thermal stress is generated when multilayer structures experience a change in temperature. If the different films have different thermal expansion coefficients then a temperature change will result in a difference in thermal expansion. Metallic films for example generally have larger thermal expansion coefficients than semiconductors. If a metallic film is deposited onto a semiconducting substrate at an elevated temperature then when the system returns to room temperature the metallic film will want to shrink more than the substrate resulting in a tensile stress in the film and a compressive stress in the surface of the substrate. If T_1 and T_2 were the temperatures during and after deposition then the film would experience a thermal stress σ_{th} of

$$\sigma_{th} = -E\times\Delta\alpha(T_2-T_1)/(1-\nu)$$

where $\Delta\alpha$ is the difference in thermal expansion coefficients, E the Young's modulus and ν the Poisson's ratio.

Coherency stress results when a thin film grows on a substrate or other thin film that has a crystalline mismatch with itself. In order to grow epitaxially on the substrate the film must slightly adapt its unit cell dimensions (the unit cell is strained) resulting in a build up of stress. If the crystal mismatch is more than a few percent, epitaxial growth will not take place and the film will grow polycrystalline. Coherency stress therefore occurs in systems where there is a small enough crystal mismatch for the growing unit cell to accommodate. Intrinsic stresses are those generated in films during growth that are not as a result of coherency or thermal effects. Stress can be introduced into a thin film system either through coherent growth of a film or by depositing a film with a thermal expansion coefficient different to that of the substrate. Stress introduced in this manner can be large enough to deform the entire substrate and thin film structure.

Stellenbosch University https://scholar.sun.ac.za

Stress can therefore be induced on the front side of a Si wafer by depositing a film on the back side which causes the entire wafer to be deformed. In this study different thickness of Si_3N_4 and SiO_2 films were deposited onto the back side of silicon wafers to induce different stress situations in the front side of the wafer. The reaction between the stressed silicon and a deposited front side film was then studied.

2.1.4. Films of compounds and alloys

In some cases it is necessary to deposit a film composed of more than one element. There are various deposition techniques that can do this. They can be divided into two groups. The first group deposits the film stoichiometrically from a target with the desired composition. Examples are Pulsed Laser Deposition (PLD) and magnetron sputtering. The other group introduces a mixture of gases or vapors into the deposition chamber. The relative activity of the components determines the composition of the film. Examples are co-evaporation, Molecular Beam Epitaxy (MBE) and Chemical Vapor Deposition (CVD). A co-evaporation system was assembled and used in this study to deposit thin films of metal alloys. The different metals were placed in water-cooled copper crucibles inside a vacuum deposition chamber. Three e-guns could be used to melt three different metals simultaneously. The evaporation of each metal was monitored separately using crystal thickness monitors and the deposition rate was then controlled via a feedback system to the power supplies running the e-guns by INFICON deposition controllers. The relative deposition rates of the different metals determined the composition of the alloy thin films.

2.1.5. Vacuum annealing

The thin film structures were annealed in a quartz tube vacuum furnace with a temperature range from room temperature to 1100 °C. The vacuum furnace was fitted with a 6 boat carousel. Each boat could carry 4 samples. The furnace was fitted with a mechanical fore pump, a turbo molecular pump and a liquid nitrogen cold trap. A pressure of 10^{-7} Torr was maintained during annealing. The temperature was controlled by a Eurotherm microprocessor which was part of a feedback system between a thermocouple mounted in the furnace and the furnace power supply.

Stellenbosch University https://scholar.sun.ac.za

2.1.6. Laser annealing

During furnace annealing silicides form by solid state interaction. This means that the two materials mix through solid state diffusion. The diffusion is usually uniform over the surface of the sample. In contrast to this relatively slow process laser induced silicide formation occurs by the rapid heating and then subsequent quenching of a molten liquid and often results in a complex cellular structure which is visible under the optical microscope [St-80]. An excimer laser was used with pulse energy of up to 170 mJ. The laser spot was focussed down to about 3×3mm giving a maximum energy density at the sample of about $2J/cm^2$.

2.2. Sample characterisation

2.2.1. X-ray diffraction

XRD is a quick and efficient technique for phase identification. The phases are identified by there crystal structure. The X-rays reflected from the different planes in the crystal undergo interference with each other. X-rays arriving at the same point from different planes have traveled different distances, which causes a phase shift and a resulting interference. Constructive interference occurs when the difference in distance traveled is equal to a multiple of a wavelength (see **Fig. 2.1**).

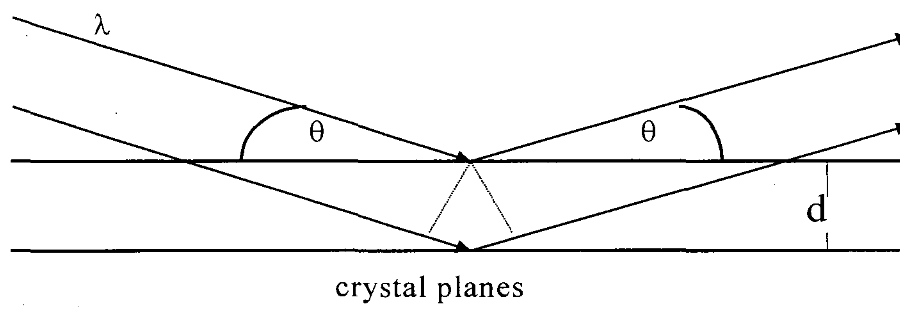

Fig. 2.1 Line diagram of X-rays reflected off crystal planes. Interference between these reflected rays gives rise to the well known Bragg equation. By varying θ and looking for constructive interference the d-spacing of the crystal planes can be measured.

Constructive interference as a function of angle is given by the well known Bragg equation:

$$2d\sin\theta = n\lambda \quad (2.1)$$

Stellenbosch University https://scholar.sun.ac.za

with d the interplanar spacing, n the the order of the reflection, λ the wave length and θ the incident angle of the radiation. This relationship states that for a given interplanar distance and X-ray energy constructive interference will occur at a scattering angle of θ. By varying θ and recording where constructive interference occurs the d-spacing of the crystal planes can be measured. A plot of X-ray counts versus θ gives a series of peaks. The position of each peak defines the spacing between a set of planes. The intensity of the peak is determined by the interference of the X-rays reflecting off the other sets of planes in the crystal.

In this study a standard θ-2θ geometry was used. The sample was horizontal while both the detector and X-ray tube moved symmetrically through an angle θ. The X-ray yield is plotted as a function of $2\times\theta$. The movement was computer controlled allowing variable scanning speed and digital data aquisition. The standard set up was 0.2^{o} per step and 10 seconds per step. Powder diffraction data files were used to do the phase identification.

2.2.2. Rutherford Backscattering Spectrometry (RBS)

Normal RBS

RBS is a very simple and fast method of obtaining elemental depth profiles in solids. It is very well suited for the study of thin films. The sample is bombarded by a monoenergetic charged particle beam. 2 MeV alpha particles were used in this study. The alpha particles penetrate the solid and are attenuated by the potential field in the solid. The alpha particles are then elastically backscattered off the nucleus of one of the atoms in the solid. As it moves out of the solid it again loses energy due to interaction with the solid. The number of elastically backscattered alpha's and their energy are detected with a solid state detector (see **Fig. 2.2**). The energy of the backscattered alpha's is proportional to the atomic mass of the atom from which it is scattered. The number of alpha's is proportional to the square of the atomic number of the scatterer. The energy loss of the alpha as it moves through the solid gives depth information.

Stellenbosch University https://scholar.sun.ac.za

There are therefore three basic concepts in RBS. Each of these is responsible for an analytic capability of the method:

1. kinetic factor (mass analysis)
2. differential scattering cross-section (quantitative analysis)
3. energy loss (depth analysis)

At the hand of **Fig. 2.2** the kinetic factor "k" is defined [Ch-78] as the ratio between the projectile energies after (E_1) and before (E_0) the elastic collision. Making use of conservation of energy and momentum (lab co-ordinates) it can be shown that:

$$k = \frac{E_1}{E_0} = \left(\frac{v_1}{v_0}\right)^2 = \left[\frac{m\cos\theta + (M^2 - m^2 \sin^2\theta)^{\frac{1}{2}}}{m + M}\right]^2 \qquad (2\text{-}2)$$

If the energy of the back scattered particle is measured at a known angle θ then the mass M of the atom from which it is scattered can be calculated and thus identified.

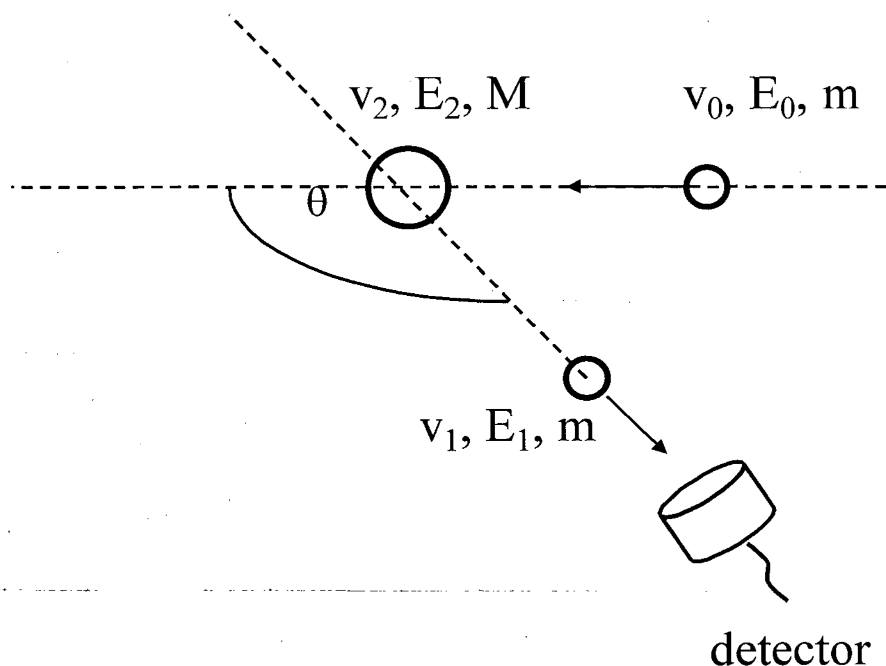

Fig. 2.2 Diagram showing elastic backscattering of a light alpha particle from a heavier atom.

The differential scattering cross section $\frac{d\sigma}{d\Omega}$ for charged nuclear particles is given in laboratory co-ordinates by [Ch-78]:

Stellenbosch University https://scholar.sun.ac.za

$$\frac{d\sigma}{d\Omega}=\left(\frac{zZe^2}{4E_0}\right)^2\frac{4}{\sin^4\theta}\frac{\left\{\cos\theta+\left[1-\left(\frac{m}{M}\right)^2\sin^2\theta\right]^{\frac{1}{2}}\right\}^2}{\left[1-\left(\frac{m}{M}\sin\theta\right)^2\right]^{\frac{1}{2}}} \qquad (2\text{-}3)$$

where z is the atomic number of the projectile, Z is the atomic number of the target atom, E_0 is the energy of the projectile before scattering, θ the laboratory scattering angle and Ω the finite solid angle spanned by detector. This definition implies that the solid angle of the detector dΩ is so small that the angle θ is well defined. If this is so then the number of particles measured at an angle θ in a solid angle dΩ would be proportional to the differential scattering cross section. In the case of detectors of finite solid angle Ω the average differential scattering cross section σ is used.

$$\sigma=\frac{1}{\Omega}\int_{\Omega}\left(\frac{d\theta}{d\Omega}\right)d\Omega \qquad (2\text{-}4)$$

This is sometimes called the scattering cross section. For very small detector solid angles Ω, $\sigma\rightarrow\frac{d\theta}{d\Omega}$

The following functional dependencies can be derived from equation 2.3:

1. $\frac{d\sigma}{d\Omega}$ is proportional to z^2. Higher backscattering yields are therefore possible with heavier particle beams.
2. $\frac{d\sigma}{d\Omega}$ is proportional to Z^2. Backscattering spectrometry is therefore much more sensitive to heavier elements.
3. $\frac{d\sigma}{d\Omega}$ is inversely proportional to the alpha particle energy. The yield therefore rises rapidly as the incoming beam attenuates through the sample material.
4. $\frac{d\sigma}{d\Omega}$ is axially symmetrical with respect to the axis of the incident beam and is therefore a function of θ only.
5. $\frac{d\sigma}{d\Omega}$ is approximately inversely proportional to $\sin^4(\theta)$ when m << M. There is therefore a rapid decrease in yield as θ is increased.

Stellenbosch University https://scholar.sun.ac.za

By measuring the energy loss of the alpha as it moves into the sample and is backscattered onto the detector it is possible to determine the depth to which the projectile penetrated. The energy loss is expressed as a stopping power $\frac{dE}{dx}$ in units of eV/Å. The stopping cross section is given as $\varepsilon = \frac{1}{N}\frac{dE}{dx}$, where N is the atomic density of the target. Both stopping power and cross section are dependant on the target composition and incoming beam energy. In general though, for small variations in energy, the stopping power ($\frac{dE}{dx}$) does not change much and the relationship between energy loss (ΔE) and depth (t) can be expressed as $\Delta E = [S]t$, where [S] is the so called backscattering energy loss factor. For thin films, Δt less than 1000 Å, the relative change in energy along the path of the particle is small. In this case the surface energy approximation can be used, meaning that $\left(\frac{dE}{dx}\right)_{in}$ is evaluated at E_0 and $\left(\frac{dE}{dx}\right)_{out}$ is evaluated at KE_0 with K known as the backscattering kinetic factor. Thus the energy lost by a projectile of mass m which was backscattered off an atom of mass M at a depth Δt can be approximated as [Fe-86]

$$\Delta E = [S]\Delta t = \left(\frac{K}{\cos\theta_1} \frac{dE}{dx}\bigg|_{E_0} + \frac{1}{\cos\theta_2} \frac{dE}{Dx}\bigg|_{KE_0} \right) \Delta t \qquad (2\text{-}5)$$

where θ_1 and θ_2 are the angles of the incoming and outgoing particle with respect to the normal. In a compound there will be more than one element say A and B in the sample. The alpha particle scatters off only one atom and therefore only one of the elements in the target. The stopping power of the material is however affected by both the elements in the sample. The energy loss of the alpha particle backscattered off element A at a depth Δt in a compound A_mB_n using the surface energy approximation is given by:

$$\Delta E = [S]_A \Delta t = \left(\frac{K_A}{\cos\theta_1} \frac{dE}{dx}\bigg|_{E_0} + \frac{1}{\cos\theta_2} \frac{dE}{dx}\bigg|_{KE_0} \right) \Delta t \qquad (2\text{-}7)$$

where K_A is the backscattering kinetic factor off element A. Bragg's rule states that $\varepsilon^{A_mB_n} = m\varepsilon^A + n\varepsilon^B$ where ε^A and ε^B are the stopping cross sections of atoms A and

Stellenbosch University https://scholar.sun.ac.za

B respectively. The total energy loss of the charged particle in the compound A_mB_n is therefore:

$$\Delta E = [S]^{A_M B_N} \Delta t = \frac{M}{m+M}[S]_A^{A_M B_N} + \frac{n}{M+n}[S]_B^{A_M B_N} \quad (2\text{-}7)$$

The height of the spectrum H gives the number of backscattered particles with energy in a certain energy interval δE between E and $(E + \delta E)$ and is given by [Ch-78, Zi-75]:

$$H = n_0 \Omega \left(\frac{d\sigma}{d\Omega}\right) N \frac{\delta E}{[S]\cos\theta_1} \quad (2\text{-}8)$$

where n_0 is the number of incident particles, Ω the solid angle of the detecting system and N the atomic density, while $\left(\frac{d\sigma}{d\Omega}\right)$ and [S] are given by equation 2.3 and equation 2.5 respectively. The height of the spectrum peak H_A for element A in the compound A_MB_N can be given in the same way as equation 2.8.

$$H_A = n_0 \Omega \left(\frac{d\sigma}{d\Omega}\right)_A N_A \frac{\delta E}{[S]_A^{A_M B_N} \cos\theta_1} \quad (2.9)$$

where N_A refers to the density of the atoms A in the compound A_MB_N. A similar equation holds for H_B the height of the spectrum peak of element B in the compound. As N_A and N_B must be proportional to M and N

$$\frac{H_A}{H_B} = \frac{\sigma_A M [S]_B^{A_M B_N}}{\sigma_B N [S]_A^{A_M B_N}} \quad (2.10)$$

where σ_A is the average differential cross section given by:

$$\sigma_A = \frac{1}{\Omega} \int \left(\frac{d\sigma}{d\Omega}\right)_A d\Omega \quad (2\text{-}11)$$

Extensive use was made of the RUMP RBS data processing and simulation computer package [Do-85]. The two major limitations to RBS as an analytical technique are:

1. It is difficult to determine the identity of heavy atomic species, since the mass resolution decreases with increasing mass.
2. Low levels of light mass impurities in a heavier mass substrate are difficult to measure because of the unfavourable ratio of scattering cross sections.

Stellenbosch University https://scholar.sun.ac.za

In-situ real-time RBS

A RBS spectrum gives the instantaneous composition as a function of depth almost like a photograph. In order to obtain information on how a system changes with time it is necessary to take a sequence of RBS spectra and compare them. To see how a phase grows in a thin film system for example a series of samples have to be made and annealed for different times. Each sample is then analysed using RBS and the spectra are compared to see how the phase grows. Two major disadvantages to this technique are that many samples have to be made and annealed and there could be differences in the structure and impurity content of the samples, which are assumed to be exactly the same. The in-situ real-time RBS system used in this study made it possible for a sample to be annealed in the scattering chamber while a scattering signal (RBS or ERDA) was being acquired, which meant that all the information about the growth of one or more phases could be derived from one sample. This was done by mounting an air-cooled copper heating stage into the RBS analysis chamber. The sample was mounted onto the copper front plate of the heat stage with silver paste. Temperature measurement was done with a thermocouple mounted in the copper heating block such that it touched the back surface of the front plate. A special ruggedised surface barrier detector had to be used as it pointed directly at the hot surface of the heating element. This detector had a thicker Au window that did not allow radiated photons from the sample to enter the active region of the detector. With the assistance of a liquid nitrogen cold trap the pressure in the chamber could reach below 10^{-6} Torr. RBS spectra are acquired *in situ* while the sample was being annealed. A 2 MeV He^+ beam was used with a backscattered angle of 165° and the sample was tilted 10° towards the detector. The heating stage was controlled by a eurotherm processor which allowed the temperature cycle, which could include isothermal (see Fig. 2.3 and 2.4) or temperature ramps to be pre-programmed. RBS spectra were acquired continuously and spectra stored at 10 second intervals. The acquired charge and sample temperature were also saved with each spectrum. After the run was completed the RBS spectra could be added to improve statistics and the charge normalised. Any variation in the charge measurement was corrected for by requiring that a certain region of the substrate contain the same number of counts in all the spectra. The RBS spectra were then analysed using the RUMP simulation package [Do-85].

Stellenbosch University https://scholar.sun.ac.za

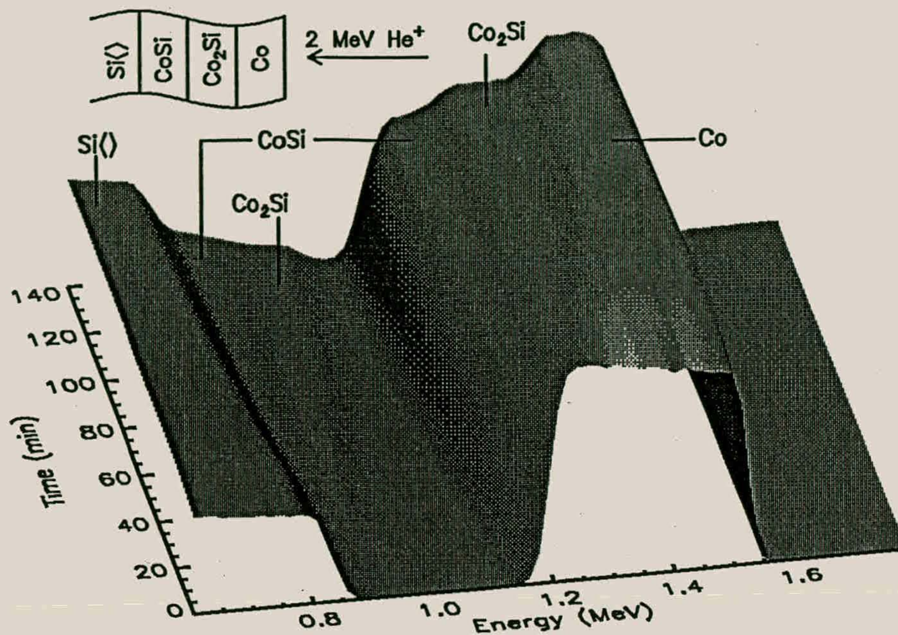

Fig. 2.3 Surface constructed from a series of RBS spectra acquired at different times from the same Co-Si sample isothermally annealed at 450°C using the in situ analysis technique. The surface shows the simultaneous growth of Co_2Si and CoSi [Th-97].

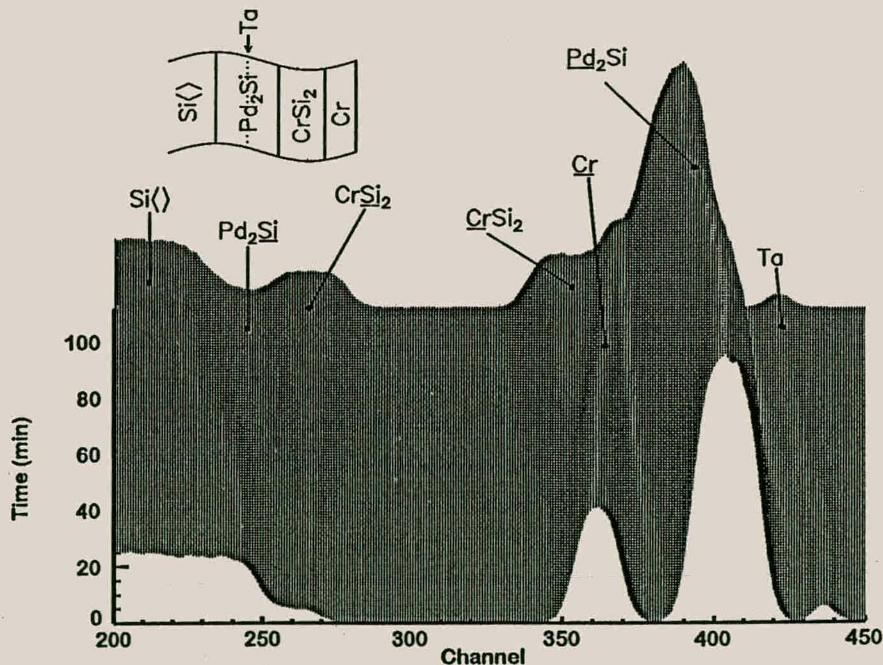

Fig. 2.4 In situ real-time RBS surface showing the formation of $CrSi_2$ on Pd_2Si. The sample temperature was ramped up to 425°C over 35 minutes by which time the Pd_2Si had already formed, and then kept at this temperature for an isothermal anneal. The Ta marker that was embedded in the $PdSi_2$ layer shifts deeper (lower energy) during the $CrSi_2$ formation indicating that the Si is being supplied by direct diffusion from the substrate. The element that has been underlined is that from which backscattering has taken place [Th-97, Th-98].

Stellenbosch University https://scholar.sun.ac.za

2.2.3. Nuclear Microprobe (NMP)

The NMP used in this study was installed onto the zero degree line of a 6 MeV Van de Graaf accelerator. The accelerator was capable of supplying high current H^+, H_2^+ and He^+ beams. The beam goes through an analysing magnet that selects the energy and then through a series of quadropole electromagnets, steering coils and collimators before it enters the microprobe as such. Three Oxford electromagnets then focus the beam onto the sample. These were lenses with very little aberration that allowed for very small beam sizes down to about 1μm. The beam was steered by Oxford scanning coils, which were fully automated with a PC interface, graphics screen and mouse control. The beam could be scanned with variable dwell time and step size and also positioned at any point in the scanning area for point analysis. Runs could be saved in event by event mode. The acquisition process could then be played back with different software settings allowing further analysis of interesting areas.

Detection facilities included: a X-ray detector, annular Si positioned for RBS, channeltron electron detector for secondary electron imaging, optical microprobe and another surface barrier detector positioned for elastic recoil detection analysis (ERDA) and scanning transmission ion microscopy (STIM). Signals accepted in the scanning mode included X-rays, RBS, secondary electrons and current measurements.

2.2.4. Scanning Electron Microscope (SEM)

In the SEM an electron beam is generated with an electron gun, accelerated through a high voltage and focused into a fine probe by electro-magnetic lenses. The electro optical column through which the beam passes is held under a high vacuum to allow free path for the electrons and to prevent high voltage discharge. Accelerating voltages vary between 5 and 40 kV. A ray diagram of a two lens SEM is shown in **Fig. 2.5**. The condenser lens causes the electron beam to converge and pass through a focal point which is above a condenser aperture. The condenser lens, in conjunction with the chosen accelerator voltage is primarily responsible for the intensity of the electron beam when it strikes the specimen. The beam again diverges below the condenser lens aperture. A final lens is used to bring the beam into focus at the specimen by demagnifying (converging) it to a focal point at the specimen surface.

Stellenbosch University https://scholar.sun.ac.za

The final lens demagnification determines the electron beam spot size at the specimen. This in turn determines the SEM resolution.

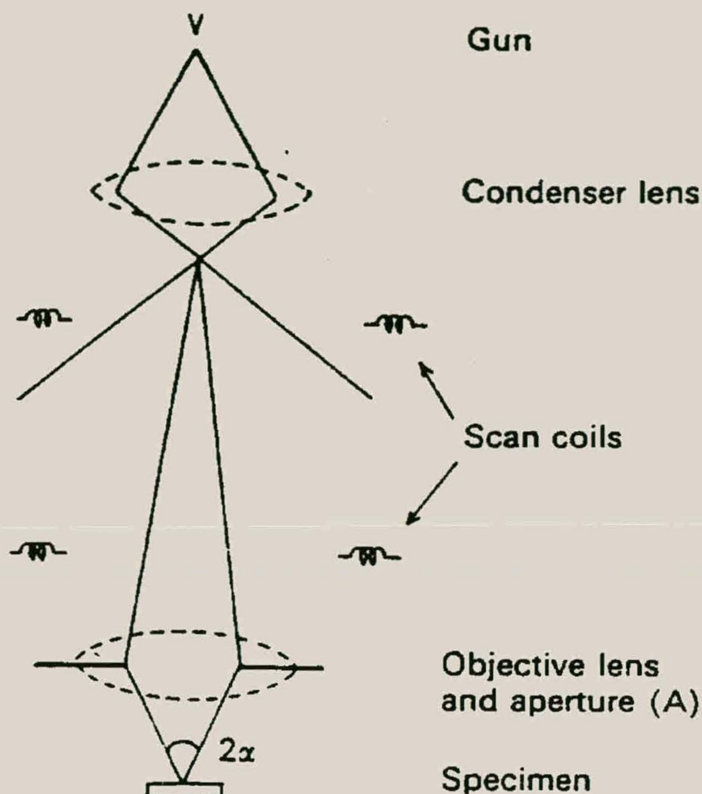

Fig. 2.5 Ray diagram of a two lens SEM showing the electron beam path to the specimen.

The electron beam is scanned across the sample by scan coils (see Fig. 2.5). From this the name scanning electron microscope. As the beam is scanned across the specimen a detector counts the number of low energy secondary electrons given off from the surface of the sample. At the same time the spot of a cathode ray tube (CRT) is scanned across the screen in a similar way as in a television. The signal measured by the detector is amplified and coupled to the CRT. The brightness of the point on the screen is therefore dependent on the amount of secondary electrons given off at the corresponding point on the surface of the sample. A one to one presentation is therefore produced between the area scanned and the screen of the CRT. Magnification of the image is the relationship between the length of the scan line on the specimen and on the CRT screen. A prerequisite for effective viewing is that the surface of the sample must be electrically conductive. During operation electrons are deposited onto the sample. These electrons must be conducted away to earth. As long

Stellenbosch University https://scholar.sun.ac.za

as the Si substrate makes good electrical contact with the sample holder the Si has a high enough conductivity to ensure good contact between the surface layers and earth.

2.2.5. Energy dispersive spectrometry (EDS)

There are a variety of interactions between the electrons in a SEM or e-microprobe and the solid being studied resulting in a variety of signals that may be detected (see **Fig. 2.6**). These signals include secondary electrons, backscattered electrons, transmitted electrons and specimen current. Information regarding specimen composition can also be determined by making use of the Auger electron signals or measuring the cathode illuminescence of the sample.

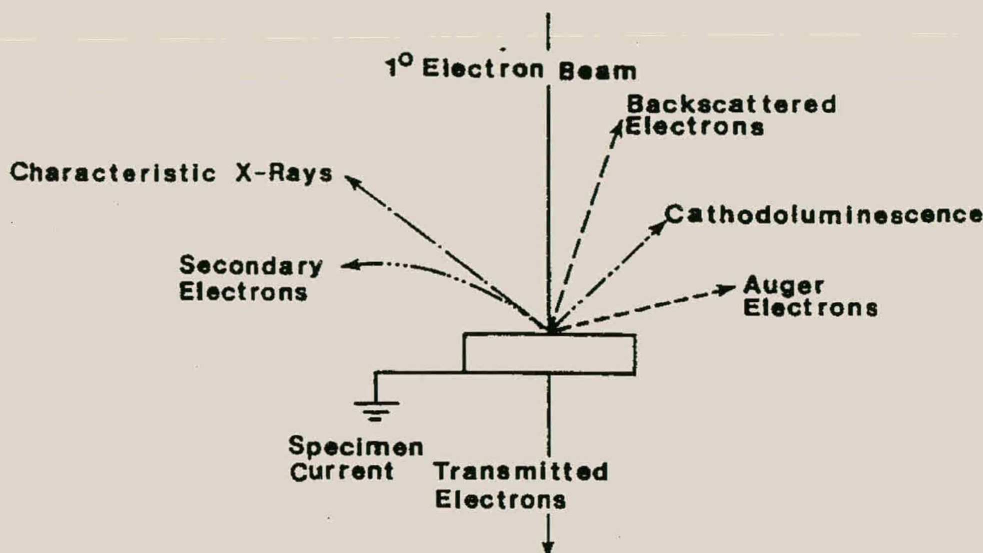

Fig. 2.6 Illustration showing seven of the possible signals generated by the primary electron beam-specimen interaction in the SEM

A technique which is used extensively for elemental identification and mapping is the measurement of the excited characteristic X-rays of atoms. The electron beam excites an atom in the sample, which then decays back to its ground state through the emission of a characteristic X-ray. This technique is often called EDAX as this is the name of a commonly used X-ray analyses system in SEM's and electron microprobes.

Stellenbosch University https://scholar.sun.ac.za

2.2.6. Optical microscopy

A NIKON LABOPHOT microscope was used that could be operated in transmitted or reflected light mode. In this study the samples were never transparent so the microscope was always used in the reflective light mode. For this reason special NIKON reflective light lenses were used, with selections of total magnification (eye piece magnification multiplied by objective lens magnification) ranging from 50 to 1000 times. A digital Charge Coupled Device (CCD) camera (SONY digital HyperHAD colour video camera) was mounted onto the microscope via an appropriate lens system. The image was projected onto a PC screen and saved in digital format using the miroVIDEO DC20 software system. The instrument was routinely used to view the surface of reacted samples as a first stage of analysis. No sample preparation is required and the results are immediate. The system was extensively used in the study of lateral diffusion, void formation, microstructure and other morphological features (see **Fig. 2.7**).

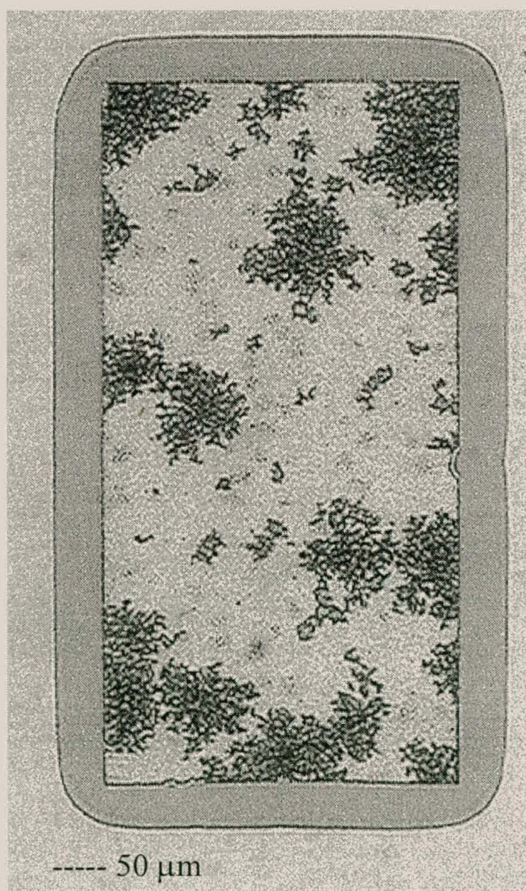

Fig. 2.7 Optical micrograph of a rectangular (340×710 µm) Al-island deposited onto a thin film of Ru. The sample has been annealed at 550 °C for 29 hours. The edge around the island shows about 50µm of lateral phase formation that has grown out of the island. The dark areas on the rectangular island are voids in the Al.

Stellenbosch University https://scholar.sun.ac.za

2.2.7. Mössbauer Spectroscopy (MS)

MS is a nuclear analysis technique used to study solids. Information about the local atomic and electronic environment of a probe atom is derived via electromagnetic radiation emitted by the probe atom while it is present in the solid. This includes information on magnetic characteristics, chemical bonds, crystal structure and the dynamics of the probe atom.

Hyperfine interactions

Every atom is in a certain environment (gas, liquid or solid) and the interaction with this environment will lead to a deformation and splitting of the nuclear energy level structure. This is the hyperfine interaction and is determined by the local microscopic environment of the nucleus. There are three basic hyperfine interactions and each is related to a measurable parameter.

1. The isomer shift (δ).

This is the shift in a nuclear energy level due to a change in electron density relative to a reference energy level. The electron density around the nucleus depends on the chemical environment and in this way MS gives information on the chemical phase. The isomer shift is usually quoted relative to that of αFe.

2. Electrical quadrupole splitting (Δ or ΔE_Q).

The quadrupole split is a splitting of a energy level induced by the presence of a electric field gradient at the site of the probe atom. In other words it is a measure of the symmetry in the charge distribution around the probe atom. Deviation from a cubic point symmetry around the probe atom will lead to splitting of the energy level.

3. Magnetic dipole interaction (nuclear Zeeman effect, H or H_M).

The nuclear Zeeman effect only plays a role when there is a magnetic field present in the crystal. This field could be generated internally within the crystal (hyperfine field) or be an applied external field. Just as in the presence of an electric field gradient this will result in a splitting of a nuclear energy level due to the Zeeman effect. The

Stellenbosch University https://scholar.sun.ac.za

parameter that is measured is the energy change between the split energy levels and this can be related to H the hyperfine field induced around the probe atom.

The combined effect of these three parameters constitutes the hyperfine interactions of the atom. They determine the shift and splitting of the nuclear energy levels. Although all nuclei in a solid undergo hyperfine interactions the MS technique cannot measure these parameters in all nuclei, because suitable nuclear energy levels are not always available.

Experimental procedure

A Mössbauer experiment requires a source that contains the radioactive Mössbauer isotope in its excited state and an absorber, which is in the sample to be analyzed. The radioactive isotope emits gamma radiation with energy of about 10 keV. The radioactive element is only classified as a Mössbauer element if the emission occurs without energy loss due to recoil. This means that the same element will be able to absorb the emitted gamma. The absorber therefore contains the same Mössbauer isotope contained in the source, but in the ground state. These atoms are called the probe atoms. The absorber is the sample in which the hyperfine interactions are to be measured. As mentioned previously αFe is usually used as the reference relative to which all shifts are measured. This effectively means that αFe will be quoted as having zero isomer shift. By moving the radiation source at different speeds relative to the absorber the radiation energy is scanned over a small energy range as it undergoes a Doppler shift. This makes it possible for the emitted radiation from the source to excite the nuclei of the probe atoms in the absorber although they have a different absorption profile due to their different environment. Measuring the absorption as a function of radiation energy gives information about the hyperfine structure and therefore the environment of the probe atoms. The probability for resonant absorption and excitation is dependent on the f-fraction or recoil fraction of the material. The f-fraction is the fraction of nuclei (of the same sort) that can absorb a photon without the creation of a phonon. This is largely determined by the stiffness of the lattice in which the atom is situated. The f-fraction will therefore decrease with increasing temperature. The Debye temperature is a parameter that quantifies the stiffness of the lattice. The stiffer an atom is bound in the lattice the smaller the recoil

Stellenbosch University https://scholar.sun.ac.za

after absorption or emission of a photon, leaving the energy of the emitted and absorbed photon the same. In this way resonant absorption and emission is possible between similar nuclei in the source and absorber. A Mössbauer isotope has to fulfill all above mentioned criteria and as a result there are few isotopes which can be used. The most commonly used are ^{57}Fe, ^{119}Sn, ^{125}Te, ^{127}I, ^{129}I, ^{129}Xe, ^{131}Xe, ^{121}Sb and ^{197}Au.

^{57}Fe Mössbauer Spectroscopy

Of all the existing Mössbauer transitions the ^{57}Fe isotope is the most commonly used. One of the most important reasons for this is that the recoil fraction is high at room temperature (>90%) which simplifies the experiment. For some other Mössbauer probe elements a cryostat is needed to obtain a high enough recoil fraction to do the measurement. The excited state of the ^{57}Fe transition (98 ns lifetime) can be supplied by the decay of either ^{57}Co, ^{57}Mn or ^{57}Ni. The long lifetime (270 days) of the ^{57}Co isotope is well suited for long measurements whereas the shorter (1.6 m) lifetime of the ^{57}Mn isotope is better suited for shorter or faster measurements.

The excited Mössbauer state decays to the ^{57}Fe ground state by emission of a 14.4 keV photon (10%) or conversion electrons (90%). Conversion Electron Mössbauer Spectroscopy (CEMS) uses the large number of electrons emitted to gain the information about the absorber. In such an experiment a ^{57}Co source is used as an emitter to study the ^{57}Fe isotope in the absorber. The ^{57}Co isotope decays to the excited ^{57}Fe Mössbauer isotope that then emits a photon, which enters the absorber and excites a ^{57}Fe isotope atom. This atom in turn decays via 90% emission of conversion electrons that are detected as a function of sample speed. Maximum resonant absorption is characterized by maximum electron emission, which is a positive peak in the spectrum. In conventional MS the resonant absorption is shown as a dip in the transmission photon signal.

The experimental set-up used for the CEMS in this study was as follows (see **Fig 2.8**). The detector was of the parallel plate type operating under constant 50mbar pressure. The detector gas was a mixture of 90% He and 10 % methane. The operating voltage was between 400 and 500 volts. The samples were mounted onto the ground plate using graphite aerosol. The incoming γ-radiation was normal to the surface of the

Stellenbosch University https://scholar.sun.ac.za

sample. A 25 mCi Co/Rh source was used. For those samples that underwent laser annealing only the laser spot was irradiated. This was done by placing a plastic/kapton mask over the samples. The data collection period of a single sample extended up to three days.

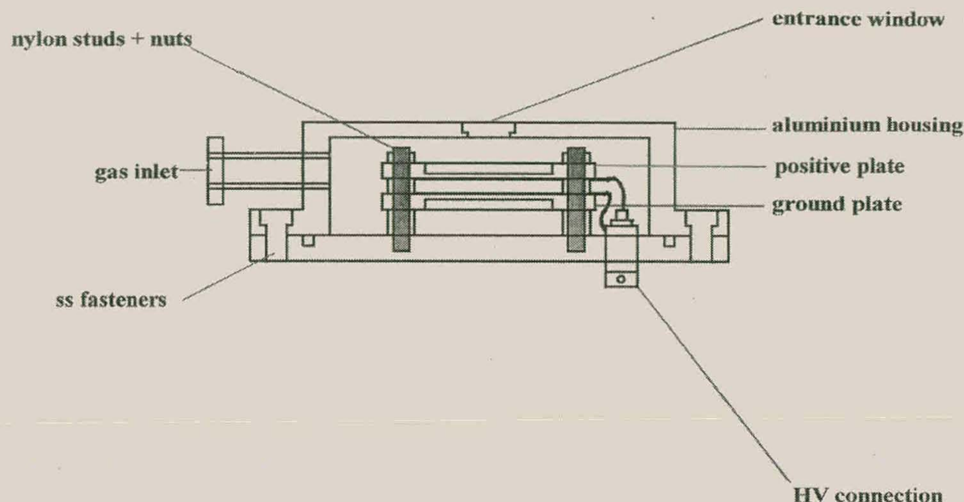

Fig. 2.8. Doppler shifted gamma rays enter the CEMS detector through the window. The Fe nuclei in the sample (which is placed on the ground plate) absorb the photons. In this process conversion electrons and gamma photons are emitted (ratio electrons to photons is 8.3:1). The electrons are accelerated by the electric field between the plates and they excite the He atoms in the detector gas, which also emit electrons causing an avalanche. The electron current is measured between the plates and this signal is proportional to the electron emission from the sample. The methane component in the gas mixture serves as a quencher to the avalanche effect.

2.2.8. Stress measurements in thin films

As mentioned before thin films deposited onto a substrate can bend the substrate as a result of stress. By measuring the change in wafer curvature and assuming that the stress in the thin film (which must be much thinner than the wafer) is isotropic the stress can be calculated using Stoney's equation (see **Appendix A** equation A.6)

$$\sigma_{film} = \left(\frac{E_{Sub}}{(1-\nu_{Sub})}\right)\left(\frac{d_{Sub}^2}{6d_{film}}\right)\left(\frac{1}{R}-\frac{1}{R_0}\right)$$

where σ_{film} is the stress in the thin film (negative=compressive and positive=tensile), E_{sub} and ν_{sub} are Young's modulus and Poisson's ratio for the substrate, d_{sub} and d_{film} are the substrate and film thickness, R_0 is the initial radius of curvature before film deposition and R is the measured radius of curvature. The following assumptions are

Stellenbosch University https://scholar.sun.ac.za

made when using Stoney's equation to calculate the stress in the thin film from the radius of curvature of the sample.

- The stress in the thin film is homogenous throughout its thickness. This is only true if $d_{film} << d_{sub}$.
- There is zero stress in the center of the substrate when it is deformed. The stress therefore changes sign from the front to the back side. This implies that the wafer deformation is small in comparison to the substrate thickness. The bow of the sample (see **Fig 2.9**) should be less than the substrate thickness.

If the stress in the thin film is not isotropic then it will be biaxial with both components in the plane of the film. There cannot be a stress component normal to the film surface. If the stress is not isotropic then the curvature must be measured as a function of position and from there the stress field can be calculated. The substrate curvature is measured by scanning a laser across a line on the surface of the sample. During the scan the position of the reflected light is measured with a position sensitive light detector at a fixed distance from the sample. The scanning is done by a rotating mirror and lens setup in such a way that for a flat sample the position of the reflected light does not move. For a curved sample the position of the reflected light moves proportionally to the position of the laser spot on the sample. The curvature of the sample can be deduced from the gradient of the reflected light position versus laser spot position curve.

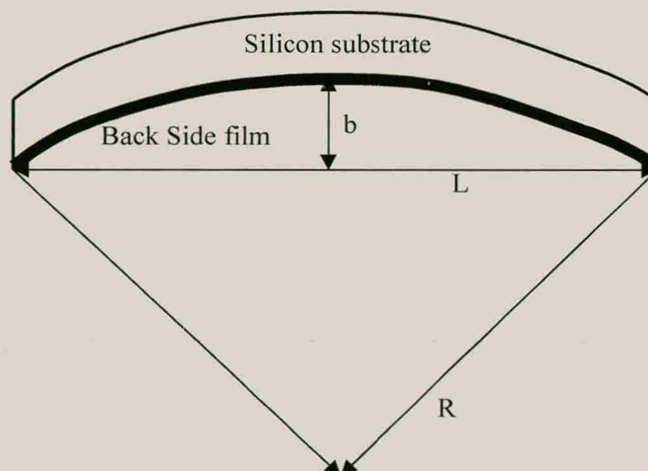

Fig. 2.9 Schematic of a curved sample with a thin film deposited on the Back Side (BS) where b=bow, L=sample size and R=radius of curvature. A positive radius of curvature means that the deposited film is under tensile stress and a negative radius would mean that the film is under compressive stress.

Stellenbosch University https://scholar.sun.ac.za

3. FE-SILICIDE FORMATION FROM ALLOYS AND THROUGH DIFFUSION BARRIERS

3.1. Introduction

On the Fe-Si phase diagram there are four compound phases and two liquidus minima (LM) situated symmetrically around the $Fe_{50}Si_{50}$ position (see **Fig. 3.1**). The four compound phases are Fe_2Si, Fe_5Si_3, FeSi and $FeSi_2$. FeSi and $FeSi_2$ occur in several polymorphic structures of which not all are stable under equilibrium conditions. Some of these phases are only formed in thin film structures on crystalline Si substrates. The equilibrium forms of the monosilicide and the disilicide are εFeSi, $\alpha FeSi_2$ and $\beta FeSi_2$ (see **table 3.1** for crystal parameters). The εFeSi is generally found as the first to form in thin film studies. The EHF model states that the first phase to form will be the one that has the most negative effective heat of formation ($\Delta H'$) at the concentration of the Liquidus Minimum (LM). The effective concentration at the interface between two materials is usually that of the LM. In this case the system has to choose between two liquidus minima at 1212 °C and 1220 °C, (see **Fig. 3.1**) and therefore seems to opt for an effective concentration in the middle between the two liquidus minima, where FeSi is thermodynamically favoured. Subsequent phase formation would depend on the relative thickness of Fe and Si. In our case the system has excess Si and therefore the most Si rich $FeSi_2$ phase forms as a second and final phase.

Table 3.1 Crystal parameters of different Fe-silicides.

Compound	Crystal system	Space group	Prototype	Lattice constants (Å)		
				a	b	c
Si	Cubic	$Fd\bar{3}m$	C	5.4		
αFe	Cubic	Im3m		2.8664		
Fe_3Si	Cubic	Im3m	W	2.841(5)		
Fe_2Si	Cubic	Pm3m	CsCl	2.81		
Fe_5Si_3	Hexagonal	$P6_3/mcm$	Mn_5Si_3	6.759(5)		4.720(5)
εFeSi	Cubic	$P2_13$		4.48798		
FeSi[CsCl]*	Cubic	$Fm\bar{3}m$	CsCl	2.7		
$\alpha FeSi_2$	Tetragonal	P4/mmm		2.69392		5.1361
$\beta FeSi_2$	Orthorhombic		$FeSi_2$	9.879	7.799	7.839
$\gamma FeSi_2[CaF_2]$*	Cubic	$Fm\bar{3}m$	CaF_2	5.4		
$Fe_{0.5}Si$[CsCl]*	Cubic	$Fm\bar{3}m$	CsCl	2.7		

*Metastable phases

Stellenbosch University https://scholar.sun.ac.za

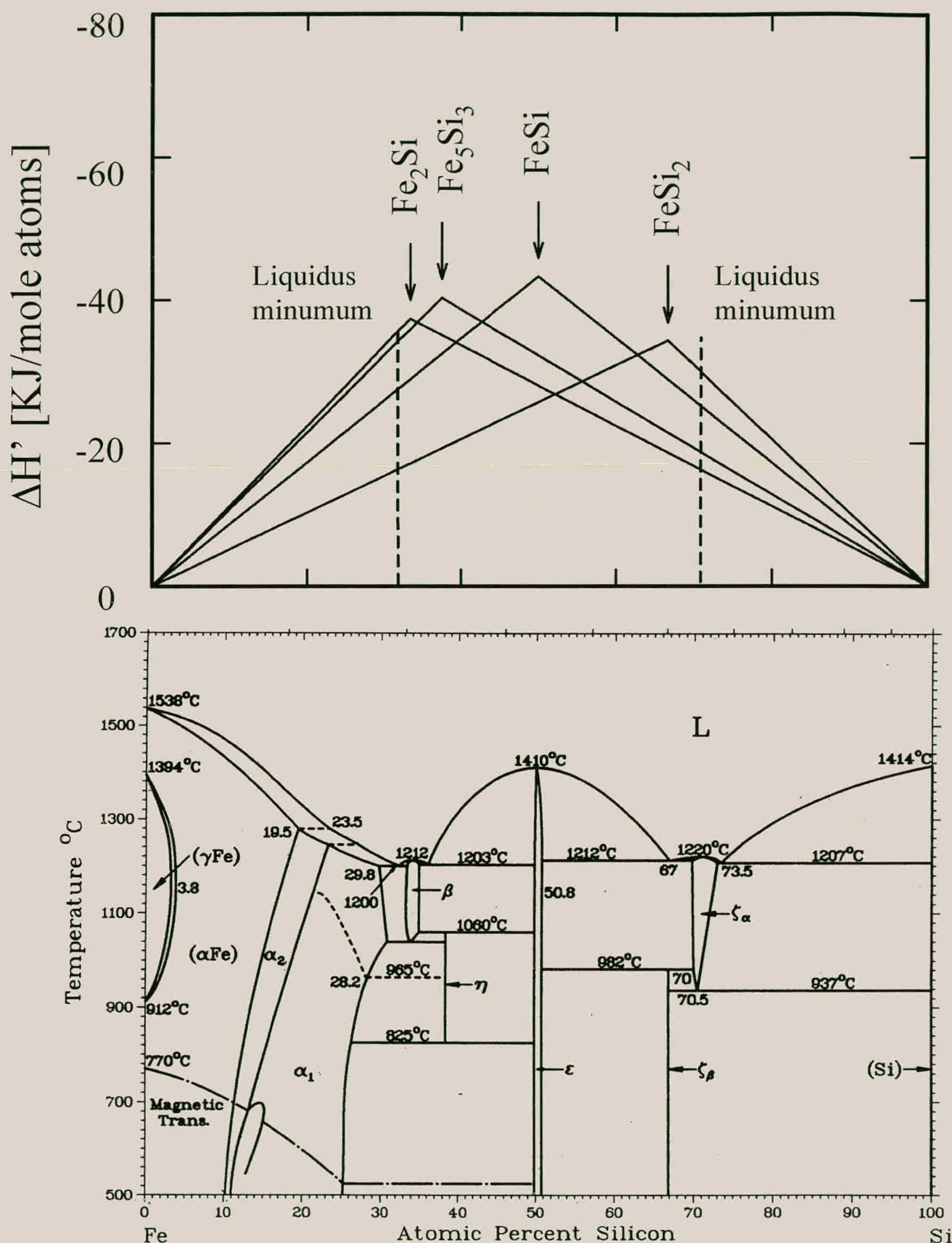

Fig. 3.1 EHF and phase diagram of the Fe-Si system. Each triangle in the EHF diagram shows the amount of energy per mole of atom that will be generated if that phase were to form, as a function of composition. The effective concentration at the interface of a binary system is chosen to be that of the liquidus minimum. In this system there are two liquidus minima very close in temperature to each other, situated at 30 and 70 at.% Fe respectively.

Stellenbosch University https://scholar.sun.ac.za

$FeSi_2$ occurs in two possible equilibrium phases namely alpha and beta. The $\alpha FeSi_2$ phase is stable above 937 °C, has a tetragonal structure and is metallic of nature. The $\beta FeSi_2$ phase is stable below 937 °C, orthorhombic in structure and is a semiconductor. It has an indirect optical band gap of about 0.87 eV (see **table 3.2**) which places it in the near infra red region making it suitable for a variety of applications including optical fiber links, light sources and infra red detectors. This is the reason for the extensive studies currently being carried out on the growth of epitaxial $\beta FeSi_2$ thin-films on silicon. There are three major factors which make large area epitaxial growth of $\beta FeSi_2$ on silicon problematic.

1. There are two possible azimuthal orientations that an epitaxial film of $\beta FeSi_2$ can have on silicon called type A and type B (see **table 3.3** and **Fig. 3.2**). Films of $\beta FeSi_2$ usually consist of a mixture of these two epitaxial crystallites [Vo-94].
2. There is a reversible transition between $\beta FeSi_2$ and the tetragonal $\alpha FeSi_2$ (a=b=2.69 Å, c=5.1 Å, see **Fig. 3.3**) phase at 937 °C. The alpha phase has also been reported below its bulk stability temperature [Vo-95, Ma-95].
3. The Fe-Si thin film system has a complicated phase formation sequence with many non-equilibrium phases which have been reported. The phase sequence is often not just dependant on the relative thickness of Fe and Si but on the absolute thickness of the films (see **Fig.3.4**) [Vo-95].

Table 3.2 Electrical properties of thin-film semiconducting silicides [Ma-95].

Silicide	Resistivity (Ω cm)	Band gap (eV)
$ReSi_2$	18×10^{-3}	0.18
$ReSi_{1.75}$	5×10^{-3}	0.16-0.32
$CrSi_2$	6×10^{-3}	0.27
$\beta FeSi_2$	3×10^{-1}	0.87

Stellenbosch University https://scholar.sun.ac.za

Table 3.3 Possible orientations for the epitaxy of $\beta FeSi_2$ on silicon (100) and (111) [Ma-95]

(100) silicon		(111) silicon			
Matching plane		Matching planes			
$\beta FeSi_2$(100)||Si(100)		$\beta FeSi_2$(101)|| Si(111)	$\beta FeSi_2$(110)|| Si(111)	$\beta FeSi_2$(100)|| Si(111)	$\beta FeSi_2$(010)|| Si(111)
Azimuthal orientation		Azimuthal orientation			
A-type	B-type	A-type	B-type		
$\beta FeSi_2$[001]|| Si<110>	$\beta FeSi_2$[010]|| Si<100>	$\beta FeSi_2$[010]|| Si[1 $\bar{1}$0]	$\beta FeSi_2$[001]|| Si[1 $\bar{1}$ 0]		
$\beta FeSi_2$[010]|| Si<110>	$\beta FeSi_2$[001]|| Si<100>				

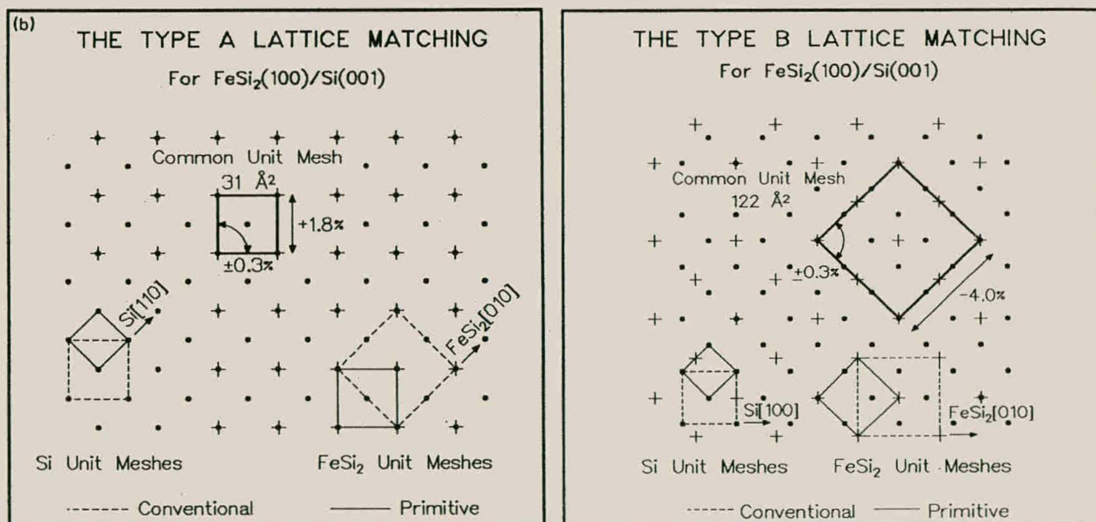

Fig. 3.2 The Type A and type B heteroepitaxial relationship and lattice matching between Si(100) and $\beta FeSi_2$ [Ge-91]. The common unit mesh which corresponds to the mismatches quoted in the figure are also shown. The A type silicide has the [010] direction of the silicide parallel to the <110> set of direction in the Si. The type B film is rotated through 45° relative to the substrate so that the [010] direction is parallel to the <100> set of directions in the Si. In both cases the (100) planes in the substrate are parallel to the (100) planes in the silicide. The Si net is denoted by • and the $\beta FeSi_2$ net is denoted by +.

When Fe-silicide thin films are grown on Si substrates a variety of metastable phases, all with the same [CsCl] crystal structure, have been reported. This is due to the very

Stellenbosch University https://scholar.sun.ac.za

good crystalline compatibility (pseudomorphism) with the substrate. The [CsCl] Fe-silicides are similar to $CoSi_2$ and $NiSi_2$ which are stable in the closely related [CaF_2] structure and also grow epitaxially on silicon. The CsCl structure $Fe_{1-x}Si$ has been formed on Si(111) in compositions ranging from x=0 to x=0.5 [Vo-92]. These [CsCl] and [CaF_2] structures can be built up from the cubic Si structure by simply replacing Si with metal atoms or vacancies. **Fig. 3.3** shows how they all consist of a basic cube of Si atoms with half the cell parameter of Si (2.7 Å instead of 5.4 Å) which is surrounded by a larger cube of Fe atoms with a cell parameter very close to that of Si (5.4 Å). By varying the amount of Fe atoms in this outer cube and the way in which they are distributed the different phases can be formed. In the case of FeSi[CsCl] all the Fe positions are filled. If half the Fe atoms in this outer cube are removed in an ordered fashion (every second atom) then $\gamma FeSi_2[CaF_2]$ is formed. The cubic symmetry in which the Fe atoms are distributed in this phase gives rise to a singlet in its Mössbauer spectrum (see **Appendix C**). If on the other hand these Fe atoms are removed randomly the CaF_2 structure is not formed although the basic CsCl structure is maintained. This disordered phase with composition $FeSi_2$ and CsCl structure is called $Fe_{0.5}Si$[CsCl]. This structure is still cubic but the Fe atoms in the outer cube are no longer distributed symmetrically around the inner Si cube and the Mössbauer spectrum of this phase is therefore not a singlet but a doublet (see **Appendix C**). The $Fe_{0.5}Si$[CsCl] phase is often confused with the $\gamma FeSi_2[CaF_2]$ phase in the literature. The γ-label is used although the Mössbauer spectra shows the characteristic doublet of the CsCl-structure Fe-disilicide. Another reason for the confusion is that if only XRD and RBS are used it is very difficult to discern between these two phases. Even the stable $\alpha FeSi_2$ can be built from the CsCl structure if the cubic structure is allowed to deform to the tetragonal structure. In some thin film cases this usually high temperature phase (>950 °C) has been found to form at temperatures as low as 550 °C when grown on Si(111) substrates [Ch-93]. This is thought to happen for the same reason that the cubic metastable phases are preferred in thin film silicide systems and that is the small crystal misfit and close match in the positioning of the atoms in the Si substrate and the silicide overlayer. It has been found experimentaly that the metastable CsCl structures are favored when very thin films are formed (~15 Å) and the substrate still has a large influence. When the films become thicker (several

Stellenbosch University https://scholar.sun.ac.za

hundred Å) the stable compounds (ε, α and β Fe-silicide) start forming. This is ilustrated in the phase diagram shown in **Fig. 3.4**.

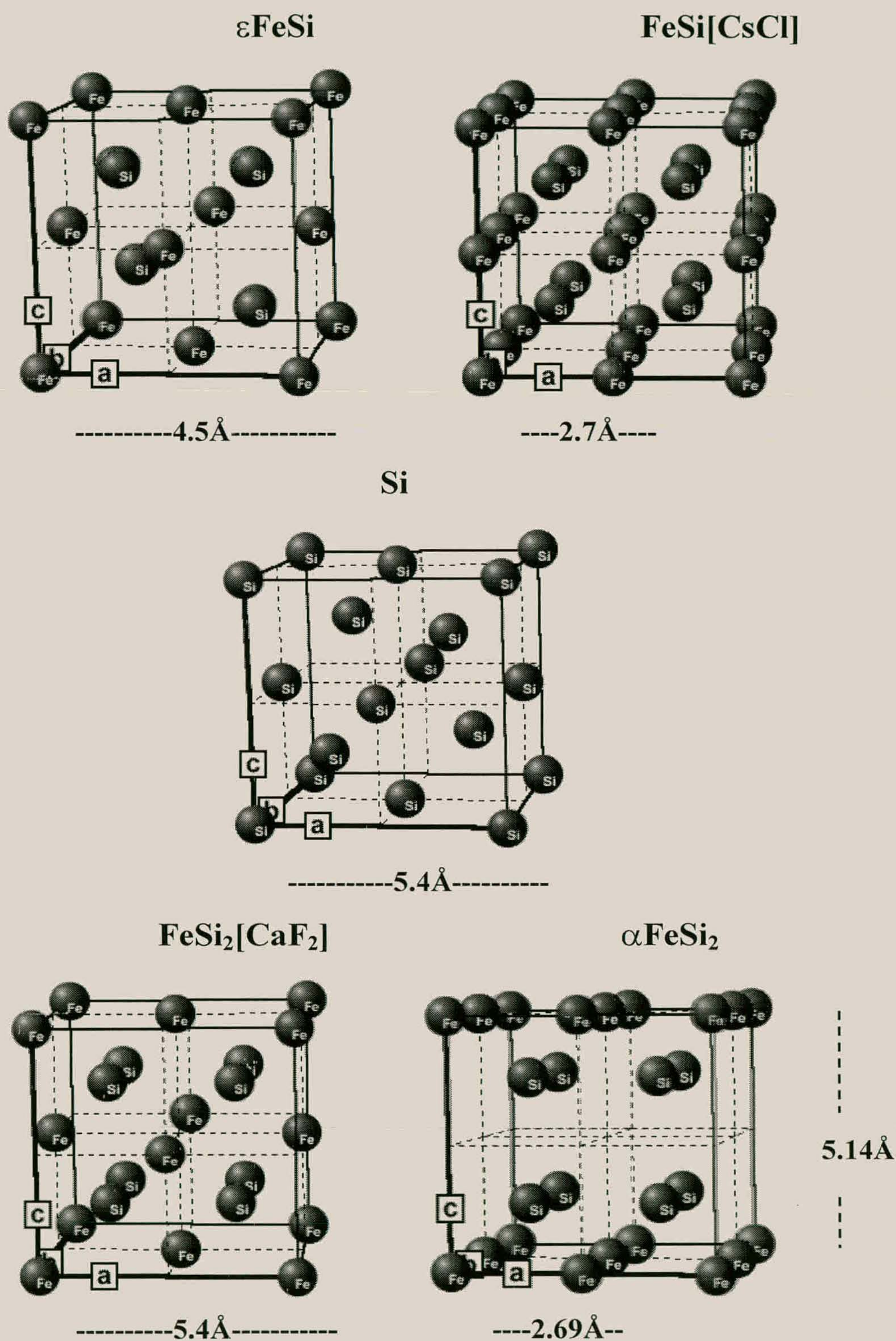

Fig. 3.3 Schematic diagrams of the crystal structures of εFiSi, FeSi[CsCl], $FeSi_2[CaF_2]$ and $\alpha FeSi_2$ showing how they compare to the Si[C] structure.

Stellenbosch University https://scholar.sun.ac.za

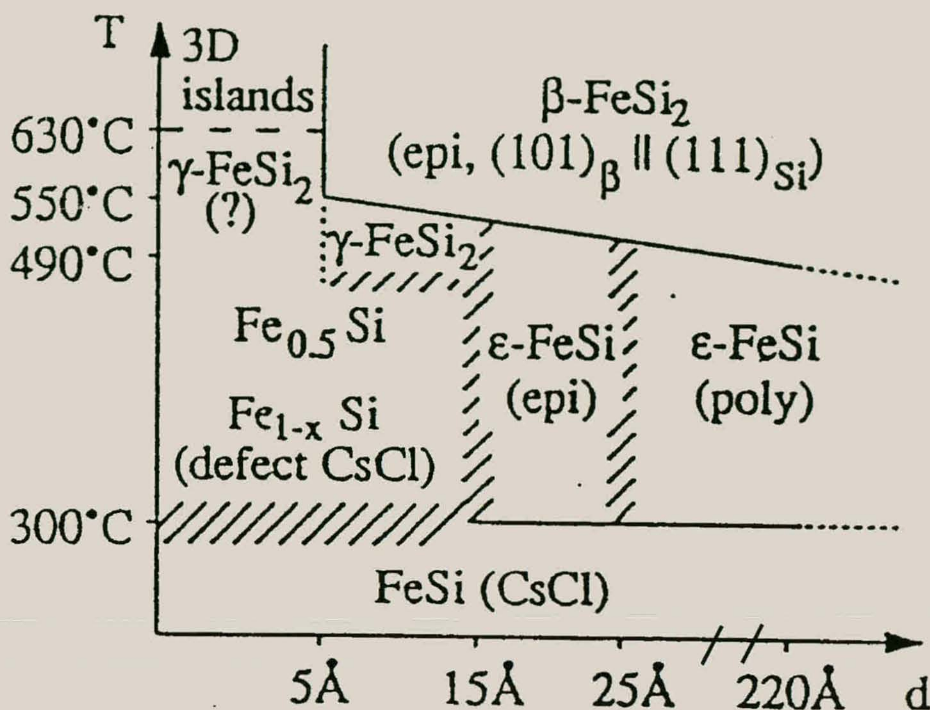

Fig. 3.4 Fe-Si kinetic phase diagram showing which phases form when Fe reacts with Si(111) for different film thicknesses and different annealing temperatures [On-93].

Due to the semiconductor nature of the $\beta FeSi_2$ phase (see **table 3.2**) there is much interest in growing this phase epitaxially on silicon. As shown in **Fig. 3.4** the $\beta FeSi_2$ phase can be formed epitaxially on Si(111) by converting the CsCl structure phases to the β phase by increasing the annealing temperature. For very thin films this does not occur via the bulk stable ε-phase. Using Reactive Deposition Epitaxy (RDE) the β-phase has also been formed by following the $FeSi[CsCl] \rightarrow Fe_{1-x}Si[CsCl] \rightarrow \alpha FeSi_2 \rightarrow \beta FeSi_2$ path [Ch-93] where the α-phase is formed at 550 °C. The success achieved in very thin film systems of growing the $\beta FeSi_2$ phase via the metastable mono and di-silicides has increased the interest in these CsCl and CaF_2 structure Fe-silicides.

Fig. 3.5 shows the total energy curves for the α, β and γ Fe-disilicides as well as the disordered d-phase ($Fe_{0.5}Si[CsCl]$) calculated as a function of atomic volume by Miglio et. al. [Mi-95]. As can be expected the β phase has the lowest energy and slightly above this is the α phase with an energy difference of 14 meV/atom. This is in agreement with the fact that the β phase is the bulk stable low temperature phase and α is the bulk stable high temperature phase. 29 meV/atom above the α phase and

Stellenbosch University https://scholar.sun.ac.za

well below the ordered $\gamma FeSi_2[CaF_2]$ is the disordered $Fe_{0.5}Si[CsCl]$ phase. It is also clear that the energy difference between the α and disordered $Fe_{0.5}Si[CsCl]$ phase in thin film epitaxial configurations is even less than 29 meV/atom because the d-phase has a smaller lattice misfit with Si than the α phase (the arrow in **Fig. 3.5** indicates the equilibrium volume of Si and this corresponds to the energy minimum of the d-phase). This corresponds to previous results showing that the ordered $\gamma FeSi_2[CaF_2]$ phase does not usually form when a thin film of Fe reacts with Si(111) but rather the $Fe_{0.5}Si[CsCl]$ phase forms. It will be shown that this also agrees with the results of this study where the disordered $Fe_{0.5}Si[CsCl]$ phase was formed epitaxially on Si(100).

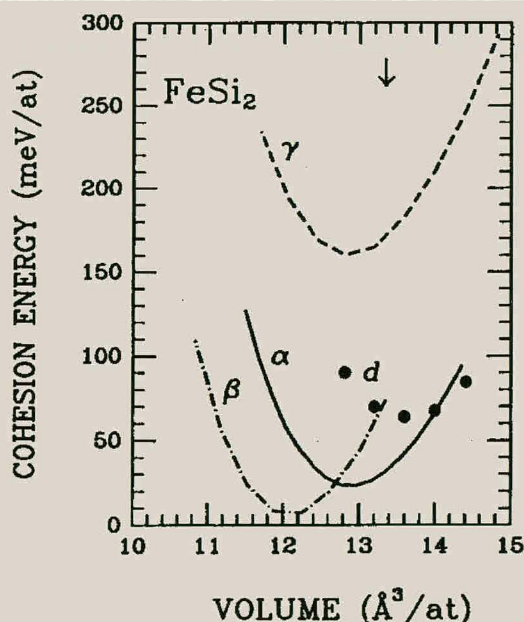

Fig. 3.5 Total energy curves versus atomic volume for all the $FeSi_2$ phases. The arrow indicates the equilibrium volume of crystalline Si [Mi-95]. The d phase is the disordered $Fe_{0.5}Si[CsCl]$ phase.

As in the Co-Si and Ni-Si systems the CsCl structure iron mono and di-silicides grow epitaxialy on Si(111) substrates simply by reacting the metal with the substrates. From the cubic symmetry of both Si and the CsCl structure it could be expected that these phases would also easily grow epitaxialy on Si(100) but this is not the case as a continuous film of CsCl Fe-silicide has until now never been formed on Si(100). The only success in forming CsCl-structure Fe-silicides on Si(100) has been by implanting Fe into Si(100) substrates followed by Ion Beam Induced Epitaxial Crystallization

Stellenbosch University https://scholar.sun.ac.za

(IBIEC) during which Fe-silicide precipitates (three dimensional islands) form. It has been found that even when the CsCl or CaF_2 structure silicides (Co and Ni-silicides) are successfully grown on Si(100) the growth is still in a direction perpendicular to the (111) planes of silicon [Va-99]. This results in the formation of pyramid structures at the reaction interface. Si(100) is the most used substrate in the integrated circuit industry and for this reason it is necessary to be able to grow technologically desirable silicides on these substrates. Si(100) was therefore used in all the Fe-Si studies carried out in this study.

There have been reports of varying degrees of success in the formation of epitaxial $\beta FeSi_2$ using SPE, MBE and IBS techniques [Ma-95]. SPE and MBE techniques result in a mixture of type A and type B beta phase at temperatures ranging from 200 to 750 °C. The most successful experimental procedure of this sort for growing the beta phase on Si<100> had the following steps [Vo-94].

- Deposition of 1-2 Å of Fe followed by a stoichiometric co-evaporation of Fe and Si for a total of 7 Å of $FeSi_2$ at room temperature.
- Annealing of the template at 400 to 500 °C.
- In order to increase the $\beta FeSi_2$ template thickness the first two steps are repeated several times, each time increasing the annealing temperature by 20 to 50 °C.
- Once the $\beta FeSi_2$ template has been formed its thickness can be increased by MBE.

IBS has also been used with some success to form $\beta FeSi_2$ epitaxially on Si<100>. The following is a typical procedure [Re-92].

- 4×10^{17} atoms/cm^{-2} of Fe is implanted into Si<100>. The implantation energy is 300 keV and the substrate temperature is 350 °C.
- The sample is then annealed at 850 °C to form a stable $\beta FeSi_2$ film.
- 1050 °C anneal to transform the beta to the alpha phase and to anneal out any defects.
- Long anneal at 800 °C to convert the alpha phase back to epitaxial beta.

In this study we investigate the use of diffusion barriers and laser annealing on the growth of epitaxial Fe-silicide films on Si<100>. Previous work done in the Co-Ti-Si

Stellenbosch University https://scholar.sun.ac.za

system showed that high quality epitaxial $CoSi_2$ films could be grown through a Ti intermediary film [La-91, Hs-91] where the function of the Ti was to getter away the residual native oxide on the silicon and act as a diffusion barrier. The diffusion barrier causes the $CoSi_2$ phase to form as first phase whereas this is usually the third phase to form in Co-Si thin film diffusion couples. This is similar to the Ni-Si system where a Ni-Zr alloy intermediary layer causes $NiSi_2$ to form as first phase instead of Ni_2Si [De-90]. In both these cases the diffusion barrier limits the supply of the metal to the reaction interface. This means that the concentration at the reaction interface changes in such a way that another phase becomes thermodynamically more viable. This approach is called Concentration Controlled Phase Selection [Pr-97]. Another function of the diffusion barrier is to regulate supply to the reaction interface in such a way that the reaction is more uniform. As in the Co-Ti-Si system Ti and Ni diffusion barriers have been used to improve the epitaxial growth of $FeSi_2$ films on Si [Ky-94, Ch-85]. The use of a diffusion barrier also caused the $\alpha FeSi_2$ to form at temperatures below its bulk equilibrium temperature. As in the IBS growth technique these groups also found that long anneals at 800 °C improved the epitaxy of the first formed $FeSi_2$. If an epitaxial film of $\alpha FeSi_2$ formed an anneal at this temperature would convert the film to epitaxial beta phase and if a polycrystalline film of $\beta FeSi_2$ formed it would improve the epitaxy.

3.2. Sample preparation

Several different alloys were used as diffusion barriers between Fe and Si<100> substrates. They were $Fe_{80}V_{20}$, $Fe_{30}V_{70}$, $Fe_{30}Ti_{70}$, $Fe_{30}Cr_{70}$ and $Fe_{30}Ni_{70}$. Some samples were prepared with 100 Å of the alloy between the Fe (500-600 Å) and the Si<100> substrate. Other samples were prepared with 500 Å of the alloy directly on top of the Si<100>. A control set of samples was made without a barrier layer with 500 Å of Fe on top of the Si<100> substrate. The samples were divided into two groups. In the first group just the Fe-V alloys were used to study the effect of the Fe:V ratio in the diffusion barriers on silicide formation and also to study the reaction of different Fe-V composition alloys with silicon. In the second group of samples different metals were alloyed with Fe and used as diffusion barriers. The samples were prepared in a vacuum co-deposition system with base pressure below 10^{-7} Torr. Samples were

Stellenbosch University https://scholar.sun.ac.za

heated in a vacuum diffusion furnace at a pressure of 2×10^{-7} Torr to induce reaction. An excimer laser was used for the laser annealing. The following annealing and etching procedure was studied.

- 800 °C, 10 minutes
- selective etch
- 800 °C, 3 hours
- laser anneal

The aim of the selective etch was to remove the alloy and un-reacted Fe and leave only the Fe-silicide that has formed during the first anneal. Several etches were investigated to determine which would be the most effective at removing the alloy and un-reacted Fe (see **Fig. 3.6**) and still leave any silicide that has formed. From this investigation (see **Table 3.4**) it was decided to use a 10% HCl etch for the Fe-Ti, Fe-Cr and Fe-Ni alloys and a 10 % HNO_3 etch for the Fe-V alloy. The second anneal is to force the system to form the $\beta FeSi_2$ phase and assist in possible improved epitaxy.

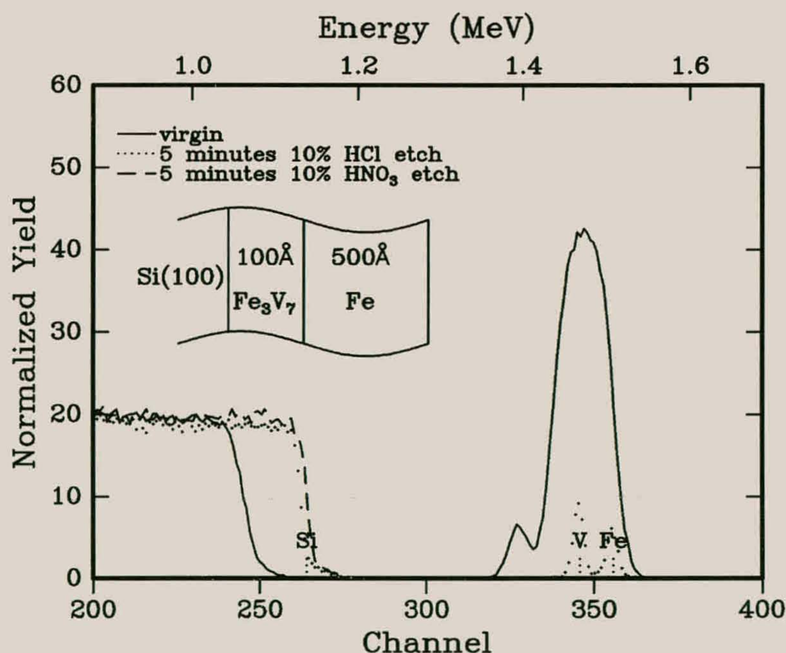

Fig. 3.6 RBS spectra showing that while HCl only removes the Fe film but not the Fe_3V_7 alloy, HNO_3 removes both. The virgin sample structure was Si<100>/100 Å Fe_3V_7/500 Å Fe. The surface position of Si, V and Fe are indicated on the spectra.

Stellenbosch University https://scholar.sun.ac.za

Table 3.4 Summary of the effectiveness of different etches. A tick means that the material was etched and a cross that the material was not.

material	HCl	HNO_3	H_2SO_4
Fe	√	√	√
Fe_3V_7	×	√	-
Fe_3Cr_7	√	×	√
Fe_3Ti_7	√	-	√
Fe_3Ni_7	√	-	√
Fe_8V_2	√	√	√
$FeSi_2$	×	×	?

3.3. Effect of the Fe-V alloy composition in diffusion barriers

The following four sets of samples were prepared using a ultra high vacuum MBE deposition system.

A: Si<100>/100 Å $Fe_{30}V_{70}$/500 Å Fe

B: Si<100>/500 Å $Fe_{30}V_{70}$

C: Si<100>/100 Å $Fe_{80}V_{20}$/500 Å Fe

D: Si<100>/500 Å $Fe_{80}V_{20}$

These samples were annealed at temperatures ranging from 200 to 550 ^{o}C in order to see what the first phase is in the different systems. In sample group A the XRD and CEMS measurements showed that εFeSi (δ=0.25 mm/s and ΔE_Q=0.47 mm/s) was the first phase to form and was present after annealing at 450 ^{o}C for 30 minutes (see **Fig. 3.7** for XRD spectra). In sample group C and D the εFeSi phase had formed after 30 minutes at 550 ^{o}C (see **Table 3.5**). The sample group B, which had only a 500Å film of the $Fe_{30}V_{70}$ alloy showed no reaction even at 550 ^{o}C. XRD analysis of the $Fe_{80}V_{20}$ alloy (sample group D) showed only Fe reflections while analysis of the $Fe_{30}V_{70}$ alloy (sample group B) showed neither Fe nor V reflections. It seems therefore that the $Fe_{30}V_{70}$ composition forms a chemically stable, probably amorphous alloy. 100 Å of this alloy allows Fe to diffuse through at 450 ^{o}C to form εFeSi but does not itself react with Si or Fe up to 550°C. The $Fe_{30}V_{70}$ alloy only reacted with Si to form $FeSi_2$ after annealing at 600 ^{o}C for 12 hours. The $Fe_{80}V_{20}$ alloy reacts with Si to form a mixture of $\beta FeSi_2$ and εFeSi at 550°C. In none of the samples was $\beta FeSi_2$ ever seen as the first phase.

Stellenbosch University https://scholar.sun.ac.za

Table 3.5 Phase formation measured in the first sample group used to determine the diffusion barrier with the best Fe-V alloy composition.

Sample	treatment	phases	Chan yield (%) *	Analysis ‡
Si<100>/100Å $Fe_{30}V_{70}$/500Å Fe				
A1	virgin	Fe, Si		XRD, RBS
A2	200°C 30 min	Fe, Si		XRD, RBS
A3	350°C 30 min	Fe, Si		XRD, RBS
A4	450°C 30 min	εFeSi, Fe, Si	100	XRD, RBS, CEMS
A5	550°C 30 min	εFeSi, Si		XRD, RBS
A15	800°C 10min, SE, 800°C 3hr	$\beta FeSi_2$, Si	100	XRD, RBS, CEMS
A15	800°C 10min, SE, 800°C 3hr, laser	$Fe_{0.5}Si$[CsCl]	85	CEMS
A16	800°C 10min, SE, laser	$FeSi_2$ §	100	RBS
Si<100>/500Å $Fe_{30}V_{70}$				
B1	virgin	Si		XRD, RBS
B2	200°C 30 min	Si		XRD, RBS
B3	350°C 30 min	Si		XRD, RBS
B4	450°C 30 min	Si		XRD, RBS
B5	550°C 30 min	Si		XRD, RBS
B8	600°C 12 hr	$FeSi_2$	100	RBS
B11	800°C 10min, SE, 800°C 3hr	$\beta FeSi_2$, Si	100	XRD, RBS
B11	800°C 10min, SE, 800°C 3hr, laser	$FeSi_2$ §	100	RBS
B12	800°C 10min, SE, laser	$FeSi_2$ §	100	RBS
Si<100>/100Å $Fe_{80}V_{20}$/500Å Fe				
C1	virgin	Fe, Si		XRD, RBS
C2	200°C 30 min	Fe, Si		XRD, RBS
C3	350°C 30 min	Fe, Si		XRD, RBS
C4	450°C 30 min	Fe, Si		XRD, RBS
C5	550°C 30 min	εFeSi, Fe, Si		XRD, RBS
C15	800°C 10min, SE, 800°C 3hr	$\beta FeSi_2$, Si	100	XRD, RBS
C15	800°C 10min, SE, 800°C 3hr, laser	$FeSi_2$ §	90	RBS
C16	800°C 10min, SE, laser	$FeSi_2$ §	100	RBS
Si<100>/500Å $Fe_{80}V_{20}$				
D1	virgin	Fe, Si		XRD, RBS
D2	200°C 30 min	Fe, Si		XRD, RBS
D3	350°C 30 min	Fe, Si		XRD, RBS
D4	450°C 30 min	Fe, Si		XRD, RBS
D5	550°C 30 min	εFeSi, $\beta FeSi_2$, Si		XRD, RBS
D6	800°C 10min, SE, 800°C 3hr	$\beta FeSi_2$, Si	100	XRD, CEMS
D6	800°C 10min, SE, 800°C 3hr, laser	$Fe_{0.5}Si$[CsCl]	90	CEMS, RBS
D7	800°C 10min, SE, laser	$FeSi_2$ §	100	RBS

*SE= selective etch, *2 MeV alpha channelling was not carried out on all the samples, ‡ When only RBS is done only the composition is given, § RBS only gives compositional information and therefore the crystalline phase cannot be identified.*

Stellenbosch University https://scholar.sun.ac.za

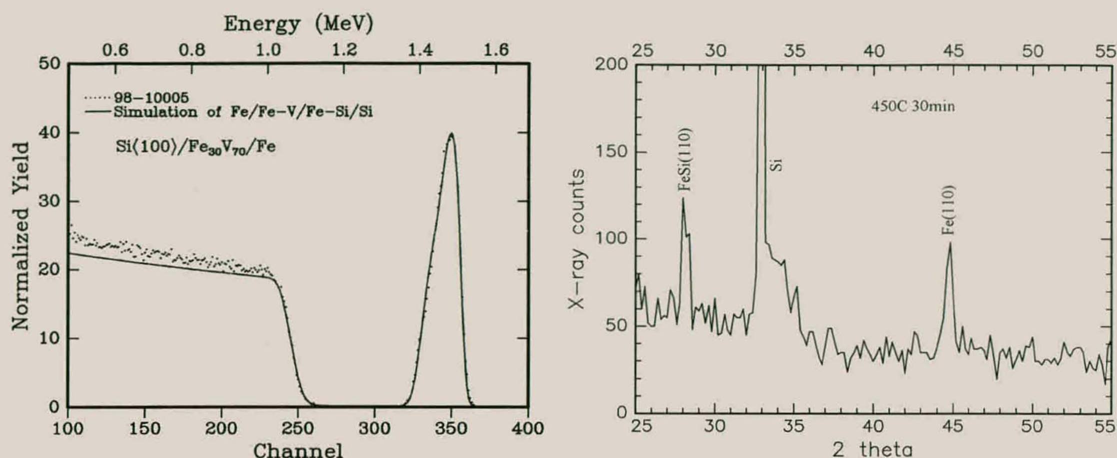

Fig. 3.7 RBS and XRD measurements of a Si<100>/100 Å $Fe_{30}V_{70}$/500 Å Fe sample showing the formation of εFeSi after 30 minutes heating at 450°C. RUMP simulation shows about 400Å of phase formation.

Samples from each of the sample groups were annealed at higher temperatures in order to force the system into forming the $\beta FeSi_2$ phase. They all underwent the same heat treatment namely: 800 °C 10 minutes + 5 minutes 10% HNO_3 + 800 °C 3 hours. The etch was to remove the alloy and any unreacted Fe after the first anneal. The second anneal was to assure the formation of the $\beta FeSi_2$ formation and to improve the quality of the film. At this stage XRD measurements showed that only $\beta FeSi_2$ had formed in all the samples (for example see **Fig. 3.8(b)**) but channelling showed that the films were not epitaxial, implying polycrystalline growth. The samples were then all irradiated using a 0.8 J/cm^2 excimer laser. Channelling measurements were carried out inside the laser spot. From sample groups A, C and D 85, 90 and 90% channelling minimum yields were measured respectively. Sample group B showed no channelling (see **Table 3.5**). Preliminary Conversion Electron Mössbauer Spectroscopy (CEMS) measurements of the samples from group A and D showed that laser caused the $\beta FeSi_2$ phase to regrow as $Fe_{0.5}Si$[CsCl], which then grew epitaxially on the Si<100> (see **Table 3.5**). The use of the $Fe_{30}V_{70}$ alloy as a diffusion barrier therefore resulted in the formation of a uniform polycrystalline film of $\beta FeSi_2$ on Si(100). This could then be converted into an epitaxial film of the metastable $Fe_{0.5}Si$[CsCl] phase after a 0.8 J/cm^2 laser anneal (Liquid Phase Epitaxy) (see **Fig. 3.8**). The alloy diffusion barrier with the least amount of Fe was therefore the most successful at facilitating the formation of epitaxial Fe-silicide. The stable nature of the alloy and the fact that there

Stellenbosch University https://scholar.sun.ac.za

was little Fe in the diffusion barrier both contributed to the slow diffusion of Fe through the barrier which seems to lead to better quality film growth. A literature search has shown that the $Fe_{0.5}Si$[CsCl] has been grown epitaxially on Si<111> by converting the $\beta FeSi_2$ phase with a pulsed laser (0.7 J/cm^2) [Ba-94, Gr-92]. The only examples of $Fe_{0.5}Si$[CsCl] grown epitaxially on Si(100) was by implanting Fe atoms into the silicon followed by Ion Beam Induced Epitaxial Crystallisation (IBIEC) [Ma-96, De-95]. In these experiments continuous films were not formed but rather precipitates of the metastable phase. It was shown that the precipitates (three dimensional islands) did grow in the [100] direction. After the success of growing epitaxial $Fe_{0.5}Si$[CsCl] on Si(100) using the $Fe_{30}V_{70}$ diffusion barrier it was decided to keep the 30:70 composition but to try other metals in the place of vanadium to see if we could improve the epitaxy even further.

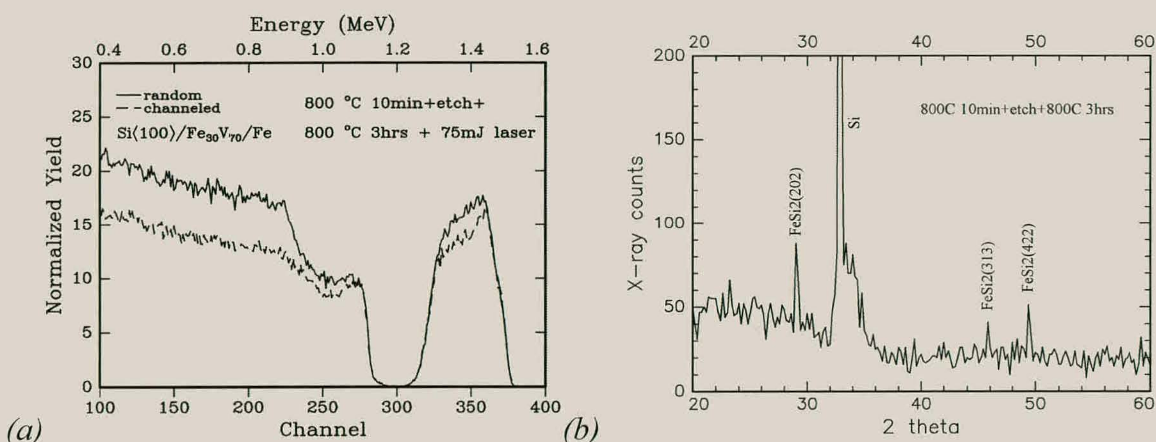

Fig. 3.8 (a)RBS random and channelled spectra of an annealed Si<100>/100Å $Fe_{30}V_{70}$/500 Å Fe sample. The $\beta FeSi_2$ silicide showed channelling with a minimum yield of 85% after a 0.8 J/cm^2 laser anneal. (b) XRD analysis shows that $\beta FeSi_2$ had formed before the laser anneal.

3.4. Effect of different alloys as diffusion barriers

Due to the success of the $Fe_{30}V_{70}$ diffusion barrier it was decided to prepare a group of samples with a variety of diffusion barriers all with 30at.% Fe. The same furnace and laser annealing treatment developed in the previous section was used on these samples and also on samples without any diffusion barrier. The alloys used were $Fe_{30}Cr_{70}$, $Fe_{30}Ni_{70}$, $Fe_{30}Ti_{70}$ and $Fe_{30}V_{70}$. The diffusion barriers were 100 Å thick, were all covered with a 500 Å Fe film and deposited onto Si(100) substrates.

Stellenbosch University https://scholar.sun.ac.za

Fig. 3.9(a) shows the reaction during and after the furnace annealing process in the sample that had 500 Å of Fe deposited directly onto the silicon substrate. The RBS spectra acquired after the sample had been annealed at 800 °C for 10 minutes shows a very non-uniform Fe distribution. The Fe to Si ratio does not correspond to an equilibrium phase. The second anneal flattens out the Fe diffusion profile further. **Fig. 3.9(b)** shows that there is no channelling in the iron after the laser anneal. Optical micrographs of the surface of the annealed samples showed what looked like either balling or very non-uniform reaction (see **Fig. 3.10**). The optical microscope also showed that the laser anneal did not improve the uniformity. This would explain the non-uniform Fe distribution shown in the RBS spectra of the reacted samples both before and after the laser anneal. Optical micrographs of samples where Fe reacted with Si through a diffusion barrier did not show any balling (see **Fig 3.11 and 3.12**).

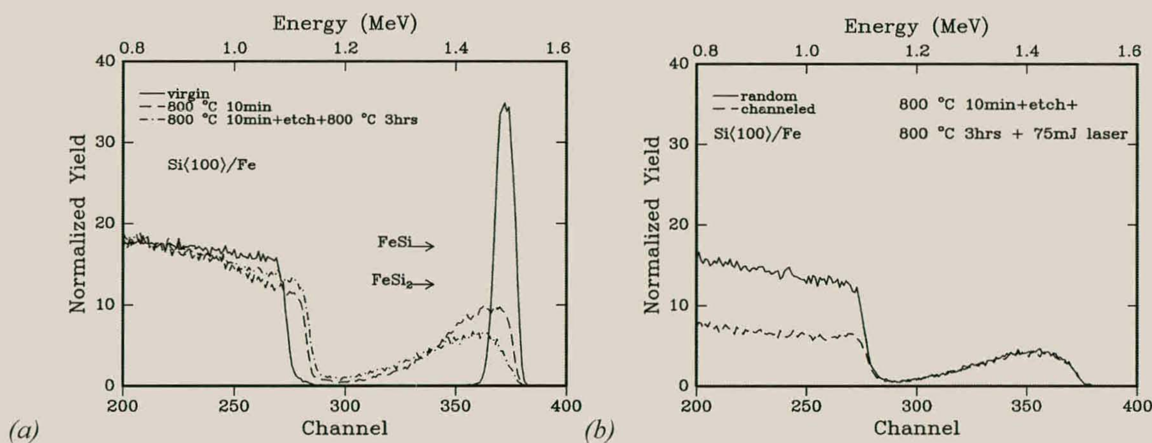

Fig. 3.9(a) RBS spectra showing phase formation in a Si<100>/500 Å Fe sample. The annealed samples show a very non-uniform Fe distribution. (b) Random and channeled spectrum showing that there is no channeling in the Fe-silicide.

Fig. 3.13 to **3.15** show RBS spectra of samples where Fe reacted with silicon through a series of different diffusion barriers. As in the case of the $Fe_{30}V_{70}$ diffusion barrier the RBS shows that a uniform silicide with the composition of $FeSi_2$ has formed after the first anneal of 800 °C for 10 minutes in all the samples (see **Table 3.6**). CEMS measurements showed this phase to be the semiconducting $\beta FeSi_2$ (see **Table 3.7** and **3.8**). The samples were then etched and again annealed at 800 °C for three hours in an attempt to improve the quality of the $\beta FeSi_2$ films. CEMS measurements still showed that only the $\beta FeSi_2$ phase was present in all the samples (see **Table 3.7** and **3.8** and

Stellenbosch University https://scholar.sun.ac.za

Fig. 3.16 and **3.17**) and RBS measurements showed no channelling (2 MeV alpha's) indicating that the silicide films were polycrystalline. At this stage the optical microscope already showed a difference in surface morphology between the samples that had used different diffusion barriers. The samples using $Fe_{30}Ni_{70}$ diffusion barriers for example showed a course grained surface indicating a large grain size (see **Fig. 3.11**). The samples using $Fe_{30}Cr_{70}$ diffusion barriers on the other hand were very smooth under the microscope indicating a small grain size (see **Fig. 3.12**).

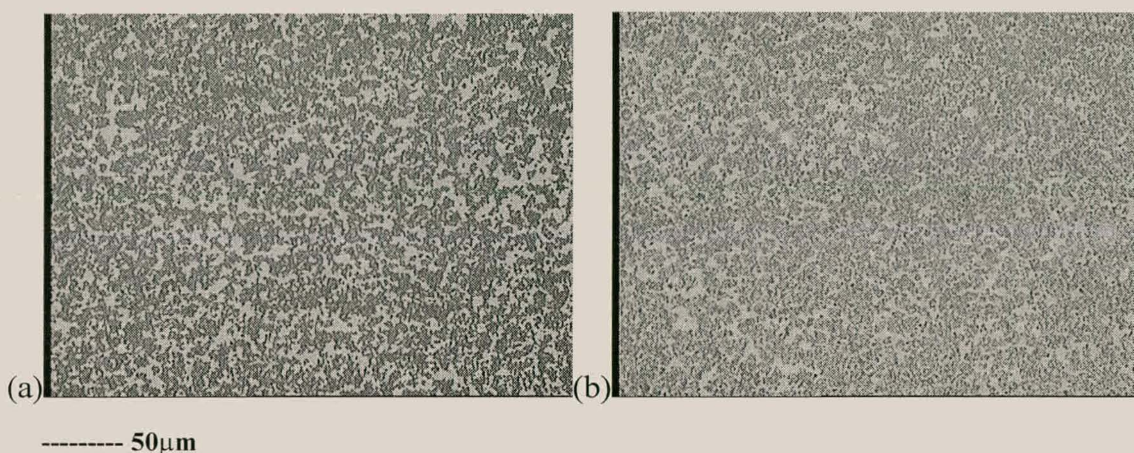

--------- 50μm

Fig. 3.10 (a) Optical micrographs of a sample that had Fe deposited directly onto Si<100> and annealed at 800 °C for 10 minutes, selectively etched and then again annealed at 800 °C for 3 hours showing what seems to be either balling or non-uniform consumption of the surface Fe. (b) Shows the sample after a 0.7 J/cm² laser anneal still showing the non-uniform surface film.

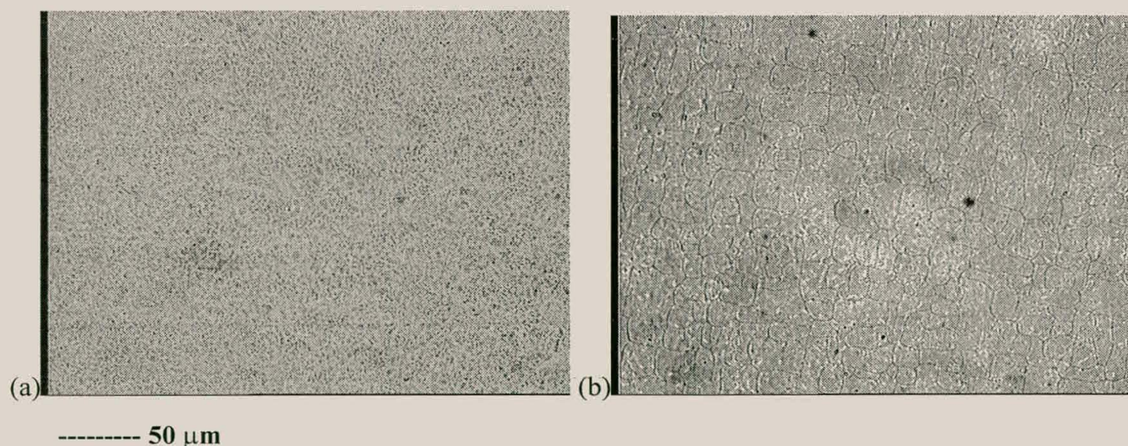

--------- 50 μm

Fig. 3.11 Optical micrograph of a Si/$Fe_{30}Ni_{70}$/Fe sample after 800 °C 10 min, selective etch and 800°C 3 hours before (a) and after (b) a 0.7J/cm² laser anneal. The unlased sample shows a course or large grain structure and did not channel. CEMS showed this film to be $\beta FeSi_2$ (see ***Fig. 3.17****). The lased sample shows a cellular pattern under the microscope and RBS showed a 80% minimum yield (CEMS showed the film to be $Fe_{0.5}Si$[CsCl]).*

Stellenbosch University https://scholar.sun.ac.za

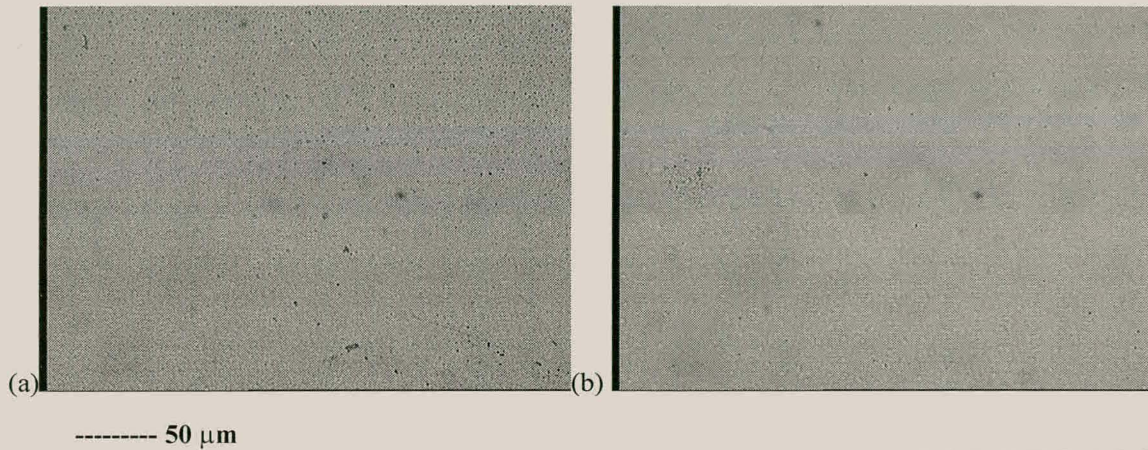

Fig. 3.12 Optical micrograph of a Si/$Fe_{30}Cr_{70}$/Fe sample after 800 °C 10 min, selective etch and 800 °C 3 hours before (a) and after (b) a 0.7J/cm^2 laser anneal showing a smooth surface in both cases indicating a fine grain structure. No channelling was present in either of the samples (see ***Fig. 3.13****). CEMS showed the film in (a) to be $\beta FeSi_2$ and the film in (b) to be $Fe_{0.5}Si$[CsCl] (see* ***Fig. 3.16****).*

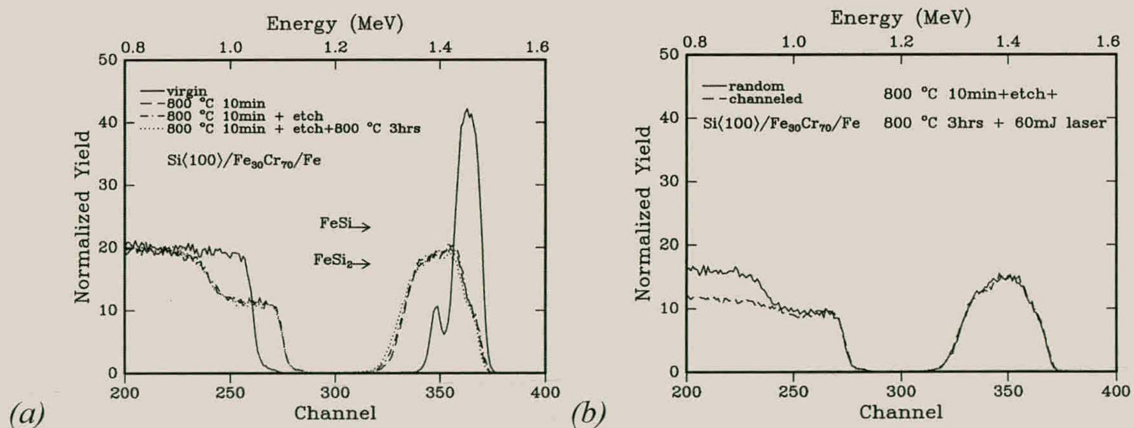

Fig. 3.13(a) RBS spectra showing phase formation in a sample with a 100 Å $Fe_{30}Cr_{70}$ diffusion barrier deposited onto the Si substrate before 500 Å Fe was deposited. The reacted samples show a uniform film of $FeSi_2$. (b) Shows that there is no channelling present in the silicide.

Stellenbosch University https://scholar.sun.ac.za

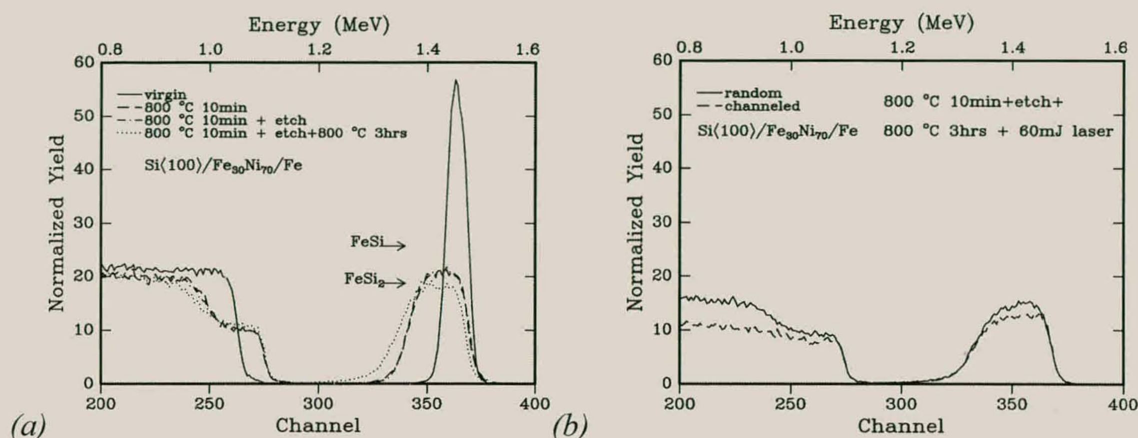

Fig. 3.14(a) RBS spectra showing phase formation in a sample with a 100 Å $Fe_{30}Ni_{70}$ diffusion barrier deposited onto the Si substrate before 500 Å of Fe was deposited. The reacted sample shows a uniform film of $FeSi_2$. (b) The channelling spectra shows a 80% minimum yield.

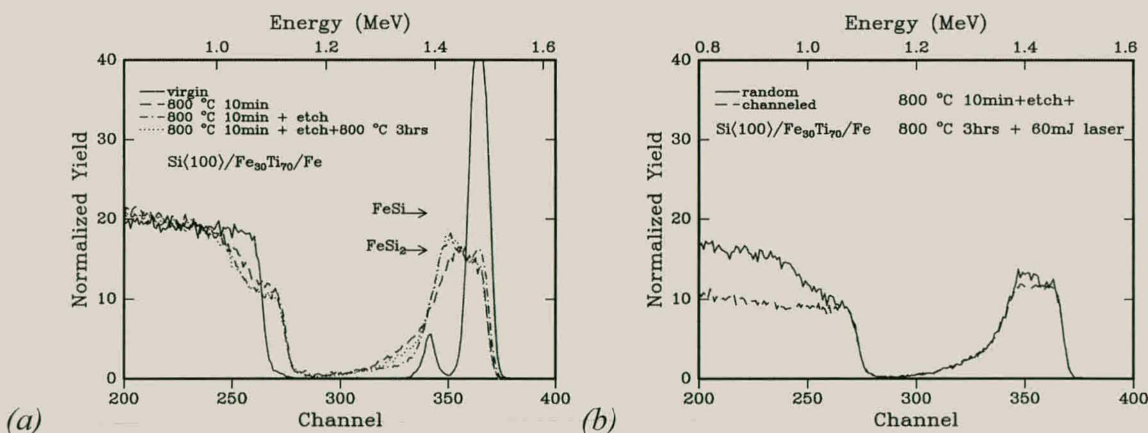

Fig. 3.15(a) RBS spectra showing phase formation in a sample with a 100 Å $Fe_{30}Ti_{70}$ diffusion barrier deposited onto the Si substrate before 500 Å of Fe was deposited. The reacted sample shows a uniform film of $FeSi_2$. (b) The channelling spectra shows a 85% minimum yield.

Stellenbosch University https://scholar.sun.ac.za

Table 3.6 Phase formation measured in the second sample group used to determine the diffusion barrier with the best Fe-metal composition.

sample	treatment	phases	Chan yield (%) *	Analysis ‡
Si<100>/100Å $Fe_{30}Cr_{70}$/500Å Fe				
Q5	Virgin	Fe, Si		CEMS, RBS, XRD
Q1	800°C 10min	$\beta FeSi_2$		CEMS, RBS
Q4	800°C 10min, SE	$\beta FeSi_2$, $\varepsilon FeSi$		CEMS, RBS
Q3	800°C 10min, SE, 800°C 3hr	βFeSi2	100	CEMS, RBS
Q2	800°C 10min, SE, 800°C 3hr, laser	$Fe_{0.5}Si$[CsCl]	100	CEMS, RBS
Si<100>/100Å $Fe_{30}Ni_{70}$/500Å Fe				
R5	Virgin	Fe, Si		CEMS, RBS, XRD
R1	800°C 10min	$\beta FeSi_2$, $\varepsilon FeSi$		CEMS, RBS
R4	800°C 10min, SE	$\beta FeSi_2$, $\varepsilon FeSi$		CEMS, RBS
R3	800°C 10min, SE, 800°C 3hr	βFeSi2	100	CEMS, RBS
R2	800°C 10min, SE, 800°C 3hr, laser	$Fe_{0.5}Si$[CsCl]	80	CEMS, RBS
R0	800°C 10min, SE, 800°C 3hr, laser, 800°C 3hr	$\beta FeSi_2$	100	CEMS, RBS
Si<100>/100Å $Fe_{30}Ti_{70}$/500Å Fe				
P5	Virgin	Fe, Si		RBS, XRD
P1	800°C 10min	$FeSi_2$ §		RBS
P4	800°C 10min, SE	$FeSi_2$ §		RBS
P3	800°C 10min, SE, 800°C 3hr	$FeSi_2$ §	100	RBS
P2	800°C 10min, SE, 800°C 3hr, laser	$FeSi_2$ §	85	RBS
Si<100>/100Å $Fe_{30}V_{70}$/500Å Fe				
A1	Virgin	Fe, Si		RBS, XRD
A17	800°C 10min	$FeSi_2$ §		RBS
A18	800°C 10min, SE	$FeSi_2$ §		RBS
A19	800°C 10min, SE, 800°C 3hr	$FeSi_2$ §	100	RBS
A20	800°C 10min, SE, 800°C 3hr, laser	$FeSi_2$ §	85	RBS

SE= selective etch, *2 MeV alpha channelling was not carried out on all the samples, ‡ When only RBS is done only the composition is given, § RBS only gives compositional information and therefore the crystalline phase cannot be identified.

Stellenbosch University https://scholar.sun.ac.za

*Table 3.7 CEMS fitting parameters (see **Appendix C**) for the Si<100>/100 Å $Fe_{30}Cr_{70}$/500 Å Fe sample group. Γ/2 is the full width half maximum of the fitted singlets (S) and doublets (D).*

Interaction	δ(mm/s)	ΔE_Q(mm/s)	Γ/2(mm/s)	Intensity(%)	Phase
Sample Q5-virgin					
S_1	-0.87		0.12	39.9	Natural Fe
S_2	-0.11		0.18	19.3	✣
S_3	+0.87		0.12	40.9	Natural Fe
Sample Q1-800°C 10minutes					
D_1	0.088(5)	0.56(1)	0.12	49.7	$\beta FeSi_2$
D_2	0.14(4)	0.32(1)	0.12	50.3	$\beta FeSi_2$
Sample Q4-800°C 10min+5min 10% HCl					
D_1	0.073(2)	0.55(2)	0.12	44.6	$\beta FeSi_2$
D_2	0.091(1)	0.34(4)	0.12	38.9	$\beta FeSi_2$
D_3	0.28	0.51(1)	0.12	16.7	εFiSi
Sample Q3-800°C 10min+5min 10% HCl+800°C 3hrs (see **Fig. 3.16**)					
D_1	0.082(2)	0.56(5)	0.12	48	$\beta FeSi_2$
D_2	0.11(3)	0.33(4)	0.12	55.2	$\beta FeSi_2$
Sample Q2-800°C 10min+5min 10% HCl+800°C 3hrs+0.7J/cm^2 laser anneal (see **Fig. 3.16**)					
D_1	0.16(1)	0.58(3)	0.22	100	$Fe_{0.5}Si$[CsCl]

✣ S_2 is probably as a result of the Fe-Cr alloy.

The samples were then all annealed using a single laser pulse from an excimer laser with a laser spot energy of 0.7 J/cm^2. CEMS measurements showed that only $Fe_{0.5}Si$[CsCl] was present inside the laser spot (see **Table 3.7** and **3.8** and **Fig. 3.16** and **3.17**). The laser therefore caused the bulk stable orthorhombic $\beta FeSi_2$ to melt and regrow as the metastable cubic $Fe_{0.5}Si$[CsCl] which has a better crystal match to the cubic silicon substrate. RBS measurements on the samples with the $Fe_{30}Ni_{70}$, $Fe_{30}Ti_{70}$ and $Fe_{30}V_{70}$ alloy diffusion barriers showed channelling inside the laser spot indicating epitaxial regrowth of the $Fe_{0.5}Si$[CsCl] after the laser anneal (see **Fig. 3.8, 3.14** and **3.15**). The sample with the $Fe_{30}Cr_{70}$ alloy diffusion barrier showed no channelling indicating a polycrystalline film of $Fe_{0.5}Si$[CsCl]. The sample with the

Stellenbosch University https://scholar.sun.ac.za

$Fe_{30}Ni_{70}$ alloy diffusion barrier showed the best channeling with an 80% minumum yield. This is the first time that a continuous film of epitaxial $Fi_{0.5}Si$[CsCl] has been formed on Si(100). Annealing of the samples that channelled after the laser anneal for 3 hrs at 800 ^{o}C caused the channelling to disappear. CEMS measurements of these samples showed that the post laser thermal anneal converts the metastable $Fe_{0.5}Si$[CsCl] phase back to $\beta FeSi_2$ (see **table 3.8** and **Fig. 3.18**).

CEMS and RBS measurements therefore show that although the samples with the $Fe_{30}Cr_{70}$ diffusion barrier did not channel and the sample with the $Fe_{30}Ni_{70}$ diffusion barrier did channel after the laser anneal they both had formed $Fe_{0.5}Si$[CsCl] inside the laser spot. This indicates that the amount of Fe in the diffusion barrier ($Fe_{30}V_{70}$ versus $Fe_{80}V_{20}$) as well as the type of metal in the alloy influences the quality of the formed silicide. Silicon is the dominant diffusing species in FeSi and Fe_3Si [Ma-95]. It is alo the dominant diffusing species in most transition metal silicides. For this reason it can probably be assumed to be the dominant diffusing species in $FeSi_2$. The reaction during the formation of the disilicide therefore takes place at the silicide/alloy interface where the iron arrives after it has passed through the diffusion barrier. As the diffusion barrier does not influence the silicon diffusion through the silicide any differences in phase formation are caused by changes in iron diffusion through the different diffusion barriers. The different grain sizes in the $\beta FeSi_2$ film formed with the $Fe_{30}Ni_{70}$ and $Fe_{30}Cr_{70}$ diffusion barriers is therefore caused by the differences in iron diffusion through the two diffusion barriers. The larger grained β-phase formed with the $Fe_{30}Ni_{70}$ barrier is converted to epitaxial $Fe_{0.5}Si$[CsCl] by the laser pulse whereas the fine grained β-phase formed with the $Fe_{30}Cr_{70}$ barrier forms polycrystalline $Fe_{0.5}Si$[CsCl]. Another difference seen under the optical microscope between the samples that channelled and those that did not was the presence of a cellular pattern inside the laser spot. This can clearly be seen in **Fig. 3.11(b)** and could have been caused by either columnar growth or diffusion paths as a result of the reordering of atoms to form an epitaxial film. Similar patterns have been seen before in systems where laser induced metal silicide formation has taken place [St-80].

Stellenbosch University https://scholar.sun.ac.za

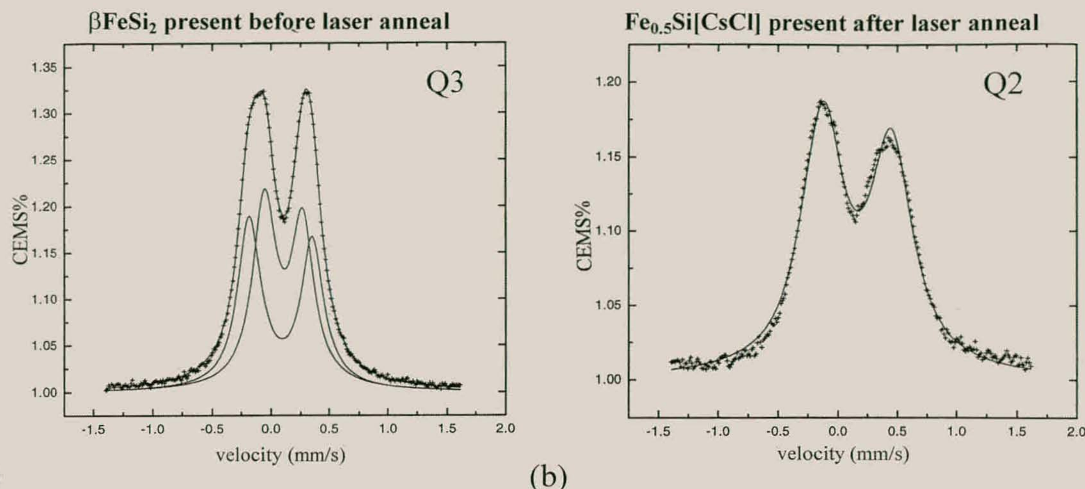

*Fig. 3.16 Mössbauer spectra of the samples that used a $Fe_{30}Cr_{70}$ diffusion barrier showing how the laser anneal transforms the $\beta FeSi_2$ phase shown in (a) into the $Fe_{0.5}Si$[CsCl] phase shown in (b). The β-phase is fitted with two doublets which are added to give the simulation, while the $Fe_{0.5}Si$ phase is fitted with only a single doublet. RBS showed no channelling in either sample (see **Fig. 3.13**). The un-symmetric shape of the doublets are due to the large amounts of vacancies in the Fe-silicides.*

*Table 3.8 CEMS fitting parameters (see **Appendix C**) for the Si<100>/100 Å $Fe_{30}Ni_{70}$/500 Å Fe sample group. Γ/2 is the full width half maximum of the fitted singlets (S) and doublets (D).*

Interaction	δ(mm/s)	ΔE_Q(mm/s)	Γ/2(mm/s)	Intensity(%)	Phase
		Sample R5- virgin			
S_1	-0.86(1)		0.12	47.3	Natural Fe
S_2	-0.86		0.18	52.7	Natural Fe
		Sample R1-800°C 10min			
D_1	0.088(7)	0.53(2)	0.12	25.3	$\beta FeSi_2$
D_2	0.099(3)	0.31(1)	0.11	19.6	$\beta FeSi_2$
D_3	0.29	0.45(7)	0.17	55.1	εFeSi
		Sample R4-800°C 10 min + 5min 10%HCl			
D_1	0.082(7)	0.59(1)	0.12	30.8	$\beta FeSi_2$
D_2	0.095(8)	0.32(1)	0.12	31.4	$\beta FeSi_2$
D_3	0.30(7)	0.47(1)	0.13	37.8	εFeSi
		Sample R3-800°C 10 min + 5min 10%HCl + 800°C 3hrs (see **Fig. 3.17**)			
D_1	0.085(3)	0.56(5)	0.12	49.5	$\beta FeSi_2$
D_2	0.10(3)	0.32(5)	0.11	50.5	$\beta FeSi_2$
		Sample R2-800°C 10 min + 5min 10%HCl + 800°C 3hrs + 0.7J/cm² laser anneal (see **Fig. 3.17**)			
D_1	0.15	0.45	0.22	100	$Fe_{0.5}Si$[CsCl]
		Sample R0-800°C 10 min + 5min 10%HCl + 800°C 3hrs + 0.7J/cm² laser anneal + 800°C 3hrs (see **Fig. 3.18**)			
D_1	0.092(3)	0.55(3)	0.13	52	$\beta FeSi_2$
D_2	0.11(2)	0.34(3)	0.13	48	$\beta FeSi_2$

Stellenbosch University https://scholar.sun.ac.za

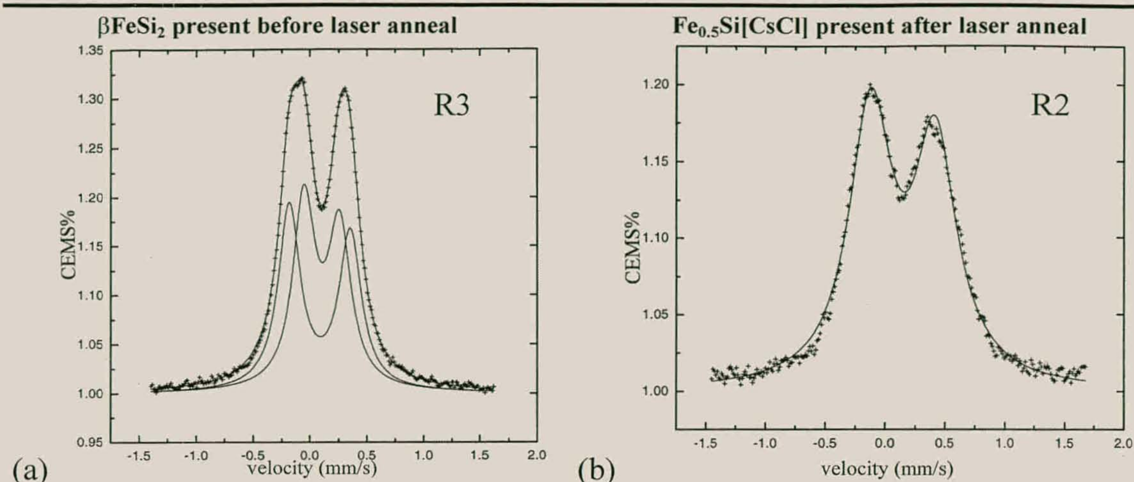

Fig. 3.17 Mössbauer spectra of the samples that used a $Fe_{30}Ni_{70}$ diffusion barrier showing how the laser anneal transforms the $\beta FeSi_2$ phase shown in (a) into the $Fe_{0.5}Si$[CsCl] phase shown in (b). The β-phase is fitted with two doublets which are added to give the simulation, while the $Fe_{0.5}Si$ phase is fitted with only a single doublet. The $Fe_{0.5}Si$ phase was epitaxial with a minimum yield of 80% (see ***Fig. 3.14****). The un-symmetric shape of the doublets are due to the large amounts of vacancies in the Fe-silicides.*

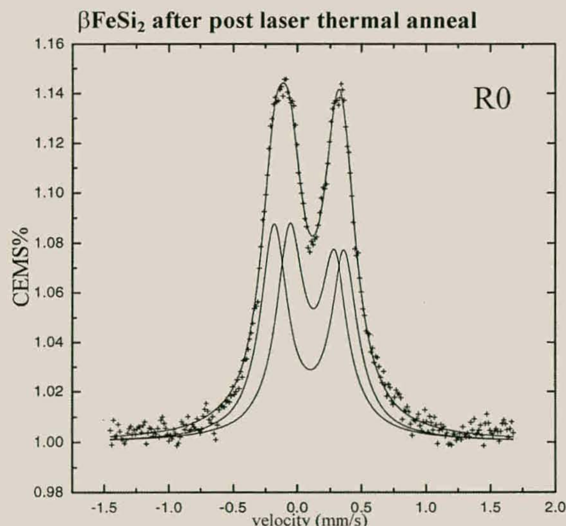

Fig. 3.18 Mössbauer spectra showing the $\beta FeSi_2$ phase. This sample was thermally annealed at 800°C for 3 hours after the laser anneal. RBS channeling showed that the $\beta FeSi_2$ phase was again polycrystalline. The un-symmetric shape of the doublets are due to the large amounts of vacancies in the Fe-silicides.

3.5. Summary and conclusions

In section 3.3 the reaction between two different Fe-V alloys ($Fe_{30}V_{70}$ and $Fe_{80}V_{20}$) and single crystal Si(100) is described. It was found that the composition of the Fe-V

Stellenbosch University https://scholar.sun.ac.za

alloy had a large effect on its reaction with Si and also its ability to act as a diffusion barrier (see **Table 3.5**). While the Fe rich diffusion barrier readily reacted with Si the Fe poor alloy remained stable up to 550 °C. XRD measurements of the un-annealed alloy's showed no Fe or V reflections from the $Fe_{30}V_{70}$ alloy while the $Fe_{80}V_{20}$ alloy showed Fe reflections. This indicates a stable probably amorphous Fe-V phase which can only accommodate a certain amount of Fe. In the Fe rich alloy the excess Fe reacts with the Si upon heating making it an unstable diffusion barrier. CEMS and XRD confirmed that εFeSi was the first phase to form in all the samples when the alloys were used as diffusion barriers. It formed earliest (450 °C) in the sample with the $Fe_{30}V_{70}$ diffusion barrier.

A sample treatment recipe involving thermal and laser annealing, was developed which made it possible to form the metastable $Fe_{0.5}Si$[CsCl] phase epitaxially on Si(100) using either the $Fe_{30}V_{70}$ or the $Fe_{80}V_{20}$ alloy as diffusion barrier. The $Fe_{30}V_{70}$ barrier gave the best results with a RBS channelling minimum yield of 85%. This is the first time that a continuos film of the cubic $Fe_{0.5}Si$[CsCl] phase has been formed epitaxially on Si(100).

It was decided to experiment with different Fe-metal alloy barriers, all with 30 at.% Fe, to try and improve the epitaxial quality. A series of samples were made with different $Fe_{30}M_{70}$ alloy diffusion barriers (M=Cr, Ni, Ti and V). They all underwent the same 800 °C 10 minute anneal, selective etch and 800 °C 3hour anneal. The samples were then irradiated with a 0.7J/cm^2 laser pulse to induce epitaxy. The same procedure was carried out on samples without any diffusion barrier. The samples without any diffusion barrier (pure Fe on silicon) did not form a uniform film of silicide after thermal or laser annealing (see **Fig. 3.9**). The samples with diffusion barriers on the other hand had formed relatively uniform polycrystalline $\beta FeSi_2$ after the 3 hour anneal. After the laser anneal they had formed the metastable $Fe_{0.5}Si$[CsCl] phase. At this stage RBS measurements showed different amounts of channeling (see **Table 3.6**). The sample with the best epitaxial $Fe_{0.5}Si$[CsCl] were those that had used a $Fe_{30}Ni_{70}$ alloy as diffusion barrier. These samples were again annealed at 800 °C for 3 hours and CEMS showed that the $Fe_{0.5}Si$[CsCl] phase had returned back to the stable $\beta FeSi_2$ phase. Samples were also laser annealed without the second 800 °C 3

Stellenbosch University https://scholar.sun.ac.za

hour thermal anneal. No channelling occurred in any of these samples (see **Table 3.5**). The second anneal therefore seemed necessary to improve the quality of the $\beta FeSi_2$ before the laser anneal.

The samples which formed epitaxial $Fe_{0.5}Si$[CsCl] showed a rough grainy texture under the optical microscope indicating large grain sizes, while those that formed polycrystalline $Fe_{0.5}Si$[CsCl] showed a smooth surface indicating a small grain size. This difference was already visible in the $\beta FeSi_2$ phase, which formed after the thermal annealing part of the sample treatment. After the laser anneal the epitaxial $Fe_{0.5}Si$[CsCl] also showed a cellular pattern which is either caused by columnar growth or diffusion paths resulting from the reordering of atoms to form the epitaxial film from the polycrystalline β-phase (see **Fig. 3.11(b)**). Similar cellular patterns have been reported in Co, Fe, Ni, Pd and Mo silicide systems, after laser induced phase formation [St-80]. The cells were thought to form during the rapid quenching of the melt caused by the laser. The idea was that the cells grow in columns in the direction of solidification with walls consisting of an impurity rich phase due to lateral rejection from the solid. These walls then cause the cellular pattern. Another possible cause was thought to be density and temperature gradients at the solid/liquid interface which cause convection and result in these diffusion paths. After the laser anneal the surface of the polycrystalline $Fe_{0.5}Si$[CsCl] became smoother (see **Fig. 3.12**) with no cellular structures. The samples with the larger grain sizes (rough texture), which also channelled, formed the cellular structures after laser annealing. The samples with the smaller grain sizes (smoother texture), which did not channel, solidified after the laser anneal without forming the cellular structures. The grain size therefore influences the mechanism by which the melted film re-grows.

Having the iron react with the silicon through a diffusion barrier vastly improved the homogeneity of Fe-silicide formation. In the samples where Fe was deposited directly onto the Si(100) substrate the Fe reacted very non uniformly. This was obvious from the Fe RBS signal and also from optical micrographs of the surface morphology (see **Fig. 3.9** and **3.10**). In the samples where the Fe first passed through a diffusion barrier uniform films of $\varepsilon FeSi$, $\beta FeSi_2$ and $Fe_{0.5}Si$[CsCl] could be formed.

Stellenbosch University https://scholar.sun.ac.za

As in the case of Ti and Ni-Zr diffusion barriers, used in the Co-Si and Ni-Si systems respectively, the use of the diffusion barrier has not only improved the homogeneity of the iron silicide films but also the epitaxy. It has been argued that this is because the Fe arrives at the reaction interface in a more ordered fashion allowing more time for the atoms to find equilibrium lattice positions. In our case the slower formation of the $\beta FeSi_2$ through the diffusion barrier did not lead to epitaxy but did allow the formation of larger grains. These large grains were then transformed into epitaxial metastable $Fe_{0.5}Si$[CsCl] using the laser. The rapid regrowth of the melt after laser annealing forced the system to choose the phase that would allow the fastest lowering of energy. As shown in **Fig. 3.5** the $Fe_{0.5}Si$[CsCl] phase is energetically very close to both the α and β phases. The very good crystalline match between the CsCl structure metastable phase and silicon further improved the thermodynamic viability of the $Fe_{0.5}Si$[CsCl] phase.

Table 3.5 and **3.6** show a summary of all the results discussed in this chapter.

Stellenbosch University https://scholar.sun.ac.za

4. EFFECT OF STRESS ON $TiSi_2$ FORMATION

4.1. Introduction

The EHF and phase diagrams of the Ti-Si binary system are given in **Fig. 4.1** from which it can be seen that there are two liquidus minima with a temperature of 1330 °C at 14 and 84 at.% Si. If the effective concentration at the reaction interface is 14 at.% Si then because non-congruently melting silicide phases usually do not form as first phase, the EHF diagram shows that Ti_5Si_3 would be preferred thermodynamically, while if the effective concentration is 84 at.% the EHF diagram shows that $TiSi_2$ would be the preferred first phase. The true concentration at the reaction interface could be anywhere between these two values and could be influenced by impurities and the presence of silicon and titanium oxides. Titanium in particular has a very high affinity for oxygen. The EHF model therefore predicts a whole range of phases and this is exactly what is found experimentally. Different groups [Pr-93] have observed $TiSi_2$, Ti_5Si_3 and TiSi as first phases. It is interesting that TiSi is reported, as non-congruently melting phases are usually not formed in thin film silicide systems unless forced to do so stoichiometrically, in which case it would form as a final phase. In our experiments thin films of Ti were deposited onto Si(100) substrates meaning that Si was always in excess and for this reason $TiSi_2$ being the most silicon rich phase would always be the final phase. $TiSi_2$ occurs in two phases, namely the low temperature high resistivity (60 μΩ-cm) C49 phase and the high temperature low resistivity (15 μΩ-cm) C54 phase. The C54-$TiSi_2$ phase is currently the most widely used silicide for ULSI circuits as it possesses the lowest resistivity of all silicides, a low contact resistance, good thermal properties and is compatible with the self aligned silicide process. $TiSi_2$ forms the contact between the first layer of metalisation and either SiO_2 or Si in the active regions of devices. The $TiSi_2$ acts as a barrier to reaction between the Al metal conductor and the underlying Si while still allowing a good electrical contact. The Ti_5Si_3 phase is also a widely used industrial material. It is usually used as a coating in high temperature applications due to its heat resistance, hardness and chemical stability. Oxidation takes place above 1000 °C in an air or oxygen environment. It is sometimes alloyed with other coatings to improve their oxidation resistance.

Stellenbosch University https://scholar.sun.ac.za

In this work the effect of stress on Ti-silicide formation in thin-film systems is investigated.

4.2. Sample preparation and stress measurements

Four sets of samples were prepared in an ultra high vacuum (UHV) deposition system. The samples were made in two steps. The first step was to introduce stress into the substrate. This was done by growing or depositing either SiO_2 or Si_3N_4 films of varying thickness onto the Back Side (BS) of Si(100) wafers (625μm thick wafers) (see section 2.1 and **Appendix** A). In the second step 500 Å of Ti was deposited onto the Front Side (FS) of the same wafers. The four sets of samples had the following geometry.

BS:400 nm Si_3N_4 / Si<100> / FS:50 nm Ti = Sample group A

BS:200 nm Si_3N_4 / Si<100> / FS:50 nm Ti = Sample group B

BS:400 nm SiO_2 / Si<100> / FS:50 nm Ti = Sample group C

BS:200 nm SiO_2 / Si<100> / FS:50 nm Ti = Sample group D

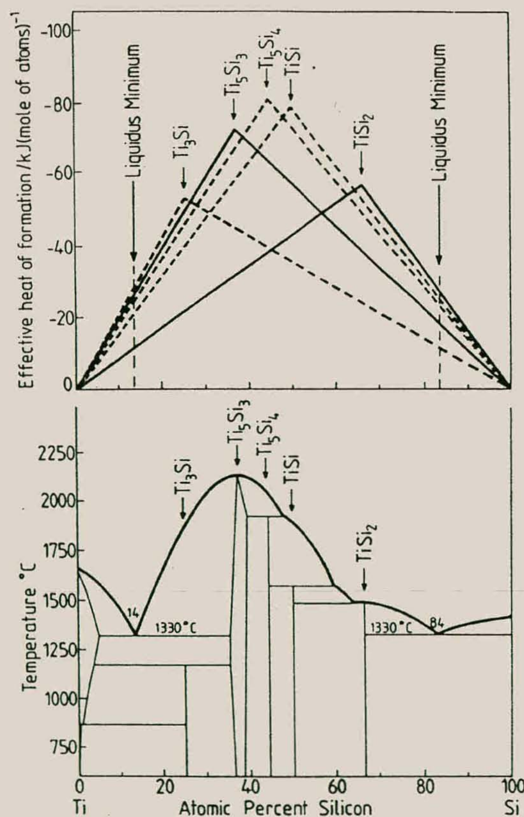

Fig. 4.1 EHF and phase diagram of the Ti-Si binary system. Each triangle on the EHF diagram shows the amount of energy per mole of atoms that will be generated if that phase were to form as a function of composition. The dashed triangles indicate noncongruently melting phases.

Stellenbosch University https://scholar.sun.ac.za

The radius of curvature of each of the samples was measured by reflection of laser light prior to the first deposition and then again after the first and second depositions. There were therefore three measurements carried out on each sample. From these measurements the stress in the deposited thin films was calculated using Stoney's equation (see section 2.2.8 and **Appendix A**). **Table 4.1** shows the results of the stress calculations in the BS and FS films at room temperature.

Table 4.1 The radius of curvature and related stress values in thin films for different samples after the Back Side (BS) and Front Side (FS) depositions respectively. Negative and positive stress values are defined as compressive and tensile respectively.

Sample group	BS film	Si Radius undeposited (m)	R_{eff} (BS-Si) (m)	R_{eff} (FS-BS) (m)	Stress (BS-Si) (MPa)	Stress (FS-BS) (MPa)
A	400nm Si_3N_4	121	24.79	1080	1459	33.2
B	200nm Si_3N_4	406	53.75	733	1345	97.9
C	400nm SiO_2	165	-93.82	-4381	-385	-8.2
D	200nm SiO_2	421	-164.72	1518	-439	47.3

Fig. 4.2 shows how the front side and the back side depositions each contribute to the total stress in the sample. The figure shows how the total stress anywhere in the final sample is a combination of the stress induced by each of the thin film depositions. The deposition process heats the samples and when the samples return to room temperature the different thermal expansion coefficients cause different amounts of contraction in the films and the substrate. Metallic films usually have larger thermal expansion coefficients than Si while insulators like SiO_2 have smaller thermal expansion coefficients (see **Appendix D**). When a film is deposited onto silicon using vacuum deposition the sample heats up due to radiative heating from the molten metal and the e-gun. In the case of thermally grown oxides the samples are heated to above $1000^{o}C$. If the film is comprised of an insulator (in this case SiO_2) and it is cooled to room temperature the film wants to shrink less than the thick silicon. This means that the Si squashes the SiO_2 film and it experiences a compressive stress. In the case of a metallic film the film wants to shrink more than the Si substrate. The substrate limits the metallic film's ability to shrink and the metallic film therefore experiences a tensile stress. The stress in the Si_3N_4 film is positive (tensile, see **table 4.1**) at room temperature. It therefore has a larger thermal expansion coefficient than Si and

Stellenbosch University https://scholar.sun.ac.za

therefore acts like a metallic film. **Fig. 4.2** shows that the stress in the substrate is caused by the combined effect of the BS and FS depositions.

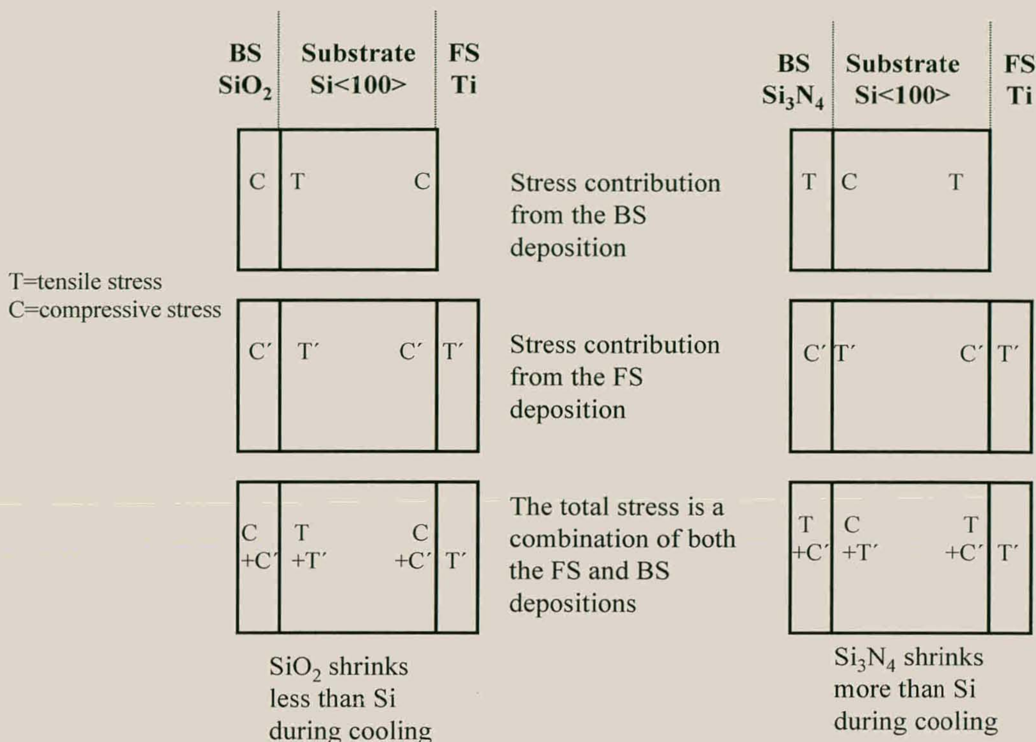

Fig. 4.2 Schematic showing the stress in the sample as a result of the combined BS and FS depositions. The stress is due to differences in thermal expansion coefficients that result in different amounts of contraction when the samples return to room temperature after deposition.

A typical stress calculation is now performed using sample group A (BS:400nm Si_3N_4) as an example (see also **Appendix A**). In our experimental set up the so called bow (b) of the sample was measured. This is illustrated in section 2.2.8 and can be related to the radius of curvature of the sample. The bow is measured before and after the BS deposition and the difference is known as Δb. For this sample the measured value for Δb was 91.88 μm. The other parameters needed to do the calculation of the stress in the deposited thin film are the Poisson ratio for silicon (ν_{Si} = 0.28), the Youngs modulus for silicon (Y_{Si} = 160 GPa), the thickness of the silicon substrate (t_{Si} = 625 μm) and the in-plane dimension of the sample (L=0.135 m). The relationship between Δb and the effective radius (r_{eff}) is (see **Appendix A** equation A.8)

$$\left(\frac{1}{r}-\frac{1}{r_0}\right)=\frac{1}{r_{eff}}=\frac{8\Delta b}{L^2}=\frac{8\times 91.88\times 10^{-6}}{0.135^2}=\frac{1}{24.79}$$

Stellenbosch University https://scholar.sun.ac.za

where r_0 and r is the radius before and after deposition. This result can now be used in the Stoney's equation (see **Appendix A** equation A.5) to calculate the stress in the deposited thin film (σ_f).

$$\sigma_f = \left(\frac{Y}{1-\nu}\right)_{Si} \frac{t_{Si}^2}{6t_f}\left(\frac{1}{r_{eff}}\right) = \left(\frac{160\times 10^9}{1-0.28}\right)\frac{\left(625\times 10^{-6}\right)^2}{6\times 400\times 10^{-9}}\left(\frac{1}{24.79}\right) = 1459\text{MPa}$$

The stress at different depths in the substrate ($\sigma_{Si}(z)$) can be calculated using the following equation (see also **Appendix A** equation A.4)

$$\sigma_{Si}(z) = \left(\frac{Y}{1-\nu}\right)_{Si}\frac{z}{r_{eff}} = 2.22\times 10^{11}\left(\frac{z}{24.79}\right)$$

where z = o is in the middle of the substrate and z = ½(625) at the FS of the substrate where the Ti will be deposited. The stress in the FS surface of the substrate is therefore

$$\sigma_{Si}(½(625)) = \sigma_{Si}(312.5) = 2.79 \text{ MPa}$$

4.3. Kinetic measurements

4.3.1. *in situ* Real time RBS

Two samples were analysed using the *in situ* real time RBS technique [Th-98] (see section 2.2.2). The samples were therefore annealed in the scattering chamber while Rutherford Backscattering Spectrometry (RBS) was being carried out. Both samples underwent the same temperature treatment, which was 25-500°C at 30°C/min (~16 minutes), and then 500-700°C at 1.7°C/min (~118 minutes). Data was acquired continuously and a RBS spectrum was written every two minutes. **Fig. 4.3** and **4.4** shows a RBS spectrum of each of the samples acquired when the samples had reached 600 °C. RUMP simulations [Do-85] of these spectra showed that 900Å of $TiSi_2$ had formed in both samples. **Fig. 4.5** shows a clear surface oxygen signal. This spectrum was constructed by adding several spectra together in the temperature range 630 to 670 °C in order to improve the statistics. **Fig. 4.6** shows that there is no difference in the amount of $TiSi_2$ formation for the two samples throughout the entire temperature ramp. At first glance it therefore seems that there are no stress-induced effects, which

Stellenbosch University https://scholar.sun.ac.za

influence the $TiSi_2$ phase formation. The thickness versus temp plots in **Fig. 4.6** do not however have the normal shape expected for a temperature ramp. The increase in thickness with temperature should be exponential and not almost linear as measured here [Tu-92]. The exponential increase should continue until the Ti is consumed. This deviation is ascribed to oxidation, which is visible in the form of an oxygen peak in **Fig. 4.5**. In this figure several *in situ* RBS spectra have been added to improve the statistics enough to see the oxygen signal. This is necessary as oxygen has a small Rutherfored scattering cross section due to its small atomic number relative to the metals. The formation of $TiSi_2$ is therefore in competition with the formation of Ti-oxide, which explains why the $TiSi_2$ thickness increases slower than expected as the temperature is ramped. A difference in $TiSi_2$ growth rate due to stress effects would only be seen if the stress effect was larger than the oxidation effect. The oxygen peak in **Fig. 4.5** is not as prominent as in the RBS spectra acquired from samples that were annealed isothermally as these were acquired using a glancing angle geometry to improve the resolution (see section 4.3.2). The vacuum in the scattering chamber during the *in situ* annealing was in the 10^{-6} Torr range whereas the vacuum during the isothermal anneals was below 10^{-7} Torr. The poor vacuum in the scattering chamber is due to outgassing from a very large surface area during heating. Oxidation effects will therefore be much greater in the *in situ* analysis process than in the isothermal annealing process.

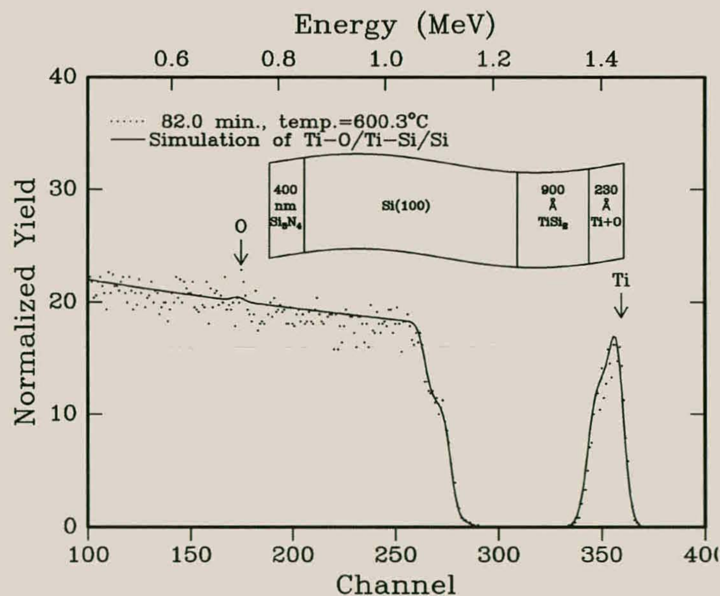

Fig. 4.3. In situ real time RBS spectrum acquired after 82 minutes when the BS:400nm Si_3N_4 sample had reached 600 °C. The RUMP simulation shows that 900 Å of $TiSi_2$ has grown and the unused Ti metal has 17at.% oxygen present in it.

Stellenbosch University https://scholar.sun.ac.za

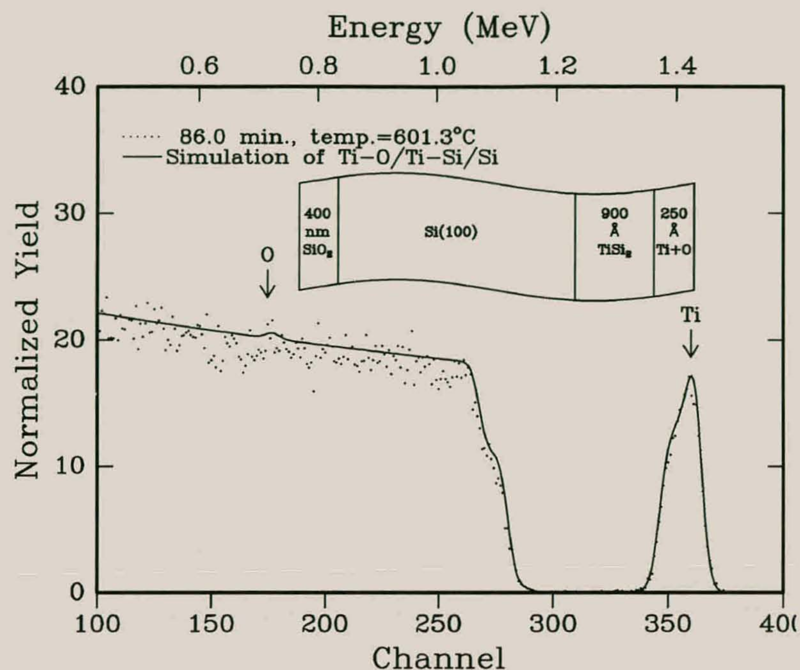

Fig. 4.4 In situ real time RBS spectrum acquired after 86 minutes when the BS:400nm SiO_2 sample had reached 600 °C. RUMP simulation shows that 900 Å of $TiSi_2$ has grown and the unused Ti metal has 20at.% oxygen present in it.

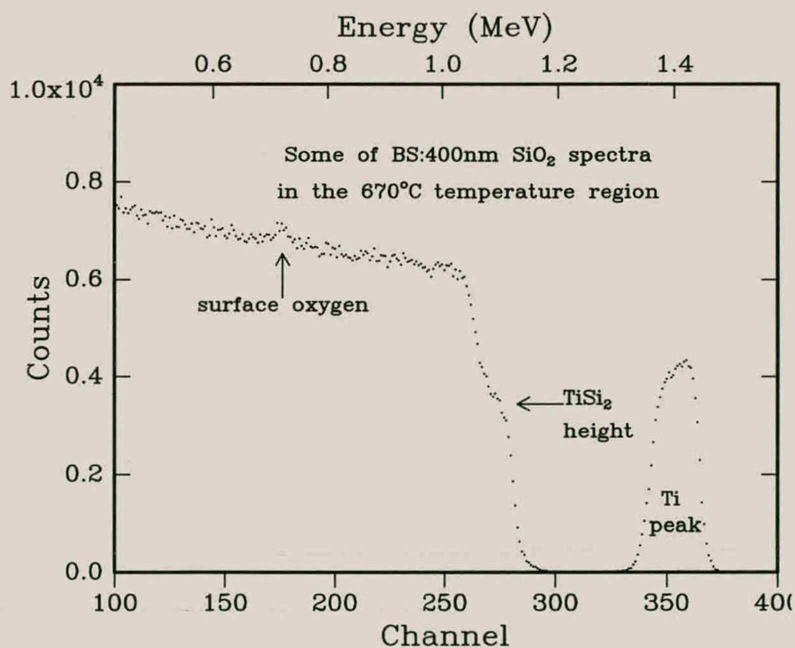

Fig. 4.5 In situ real time RBS spectra showing that the surface oxygen peak becomes visible if the statistics are improved by adding several spectra in the temperature range 630 to 670°C. The oxygen peak is not as prominent as in the standard RBS spectra from the isothermal anneals (see section 4.3.2) as those spectra were acquired with a glancing angle geometry to improve resolution.

Stellenbosch University https://scholar.sun.ac.za

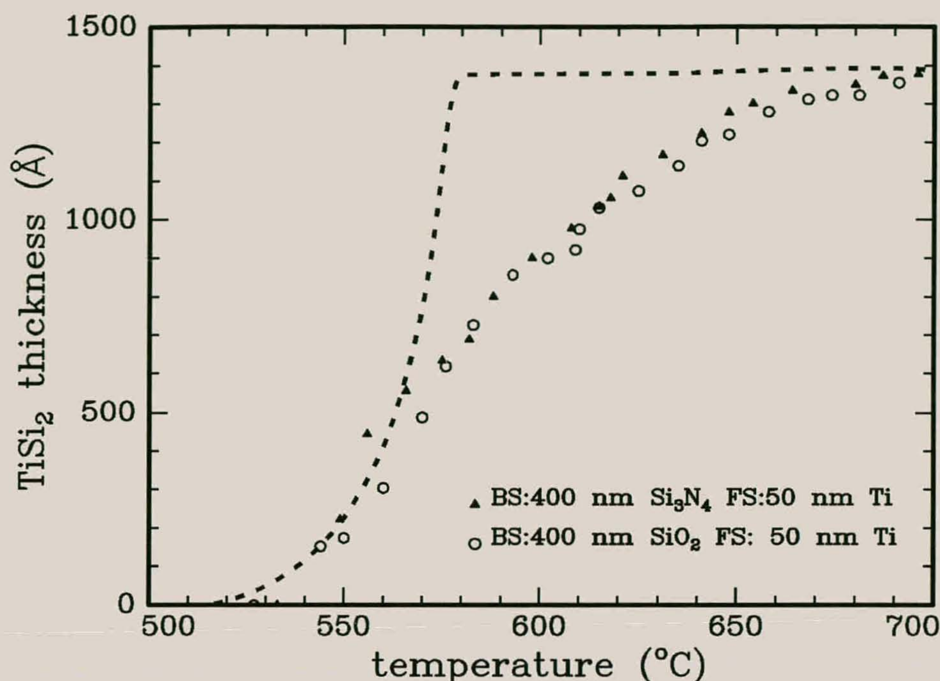

Fig.4.6 Thickness of the $TiSi_2$ film as measured using the in. situ. real-time RBS technique (25-500 °C at 30 °/min and then 500-700 °C at 1.7 °/min). There is no marked difference between the samples. The dashed line shows the exponential shape expected for a ramped sample with no impurities in the Ti. The deviation from the theoretical curve can be ascribed to oxidation.

4.3.2. Conventional isothermal anneals

RBS analysis

Conventional isothermal vacuum anneals were done on samples from all four groups at 450, 500, 550 and 600°C for different times to induce reaction. Samples from each group were annealed together in the furnace. Previous work done by Cheng [Ch-99] showed that there was still a relatively large amount of stress left in the back side (BS) films in similarly prepared samples in this temperature range (see **Fig. 4.7**). The room temperature stress values measured in the BS films in this study were of the same order or larger than those measured by Cheng (see **table 4.1** and **Fig. 4.7**). XRD showed that in three of the sample groups only $TiSi_2$(C49) had formed below 650°C (see section on XRD). In the third sample group (BS:200nm SiO_2) XRD showed that Ti_5Si_3 had formed. **Fig. 4.8** and **4.9** shows RBS spectra from each sample group after annealing at 600°C for 10 minutes. A glancing angle RBS geometry was used to improve the resolution. This geometry not only improved the thickness resolution of the Ti-silicides but also by counting for longer times the oxygen signal became clearly visible (see **Fig. 4.8** and **4.11**). The detector was at 15 degrees and the sample was

Stellenbosch University https://scholar.sun.ac.za

turned 70 degrees toward the detector. The full width half maximum of the detector was 15 keV.

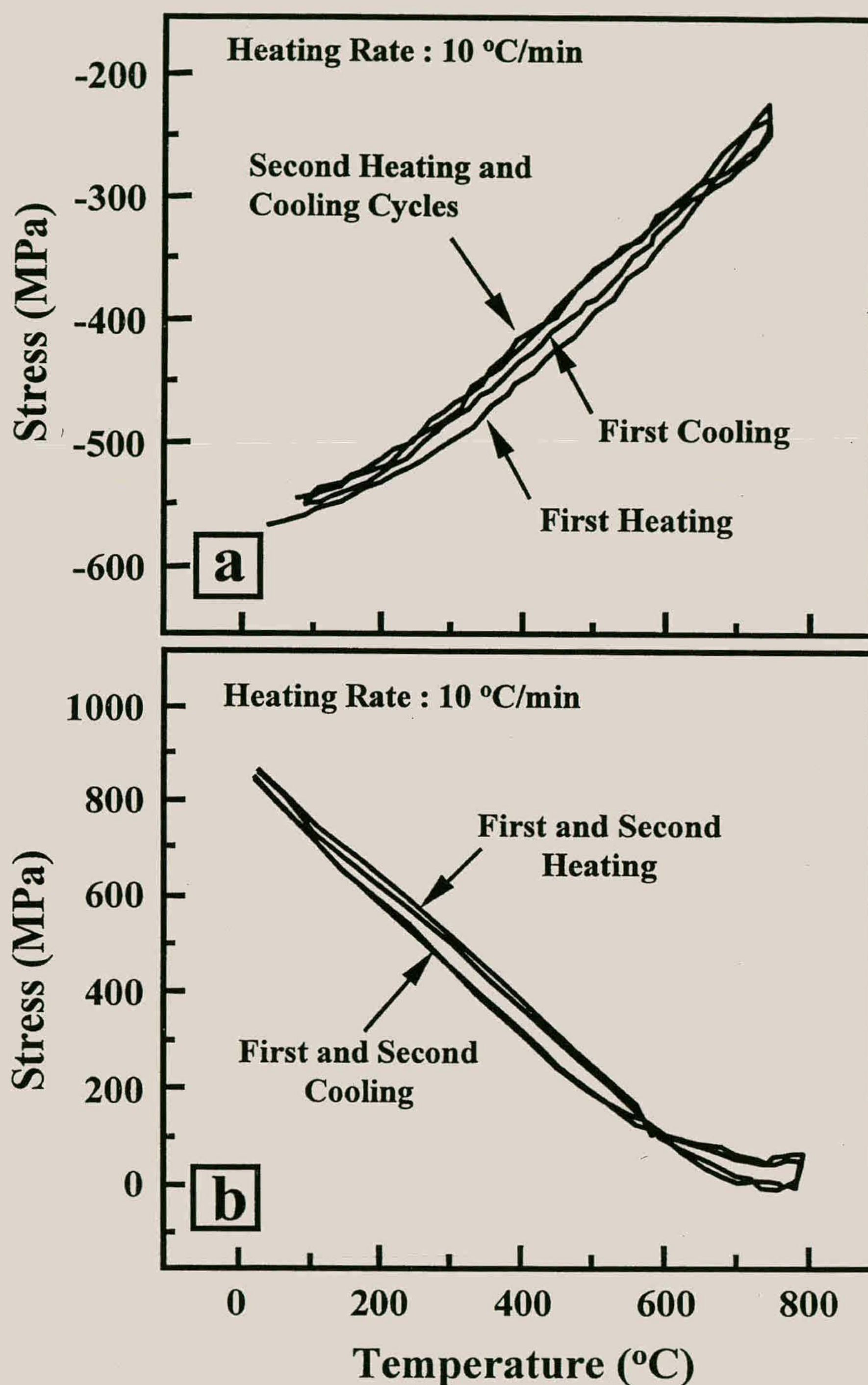

Fig 4.7 Stress as a function of temperature measured in the BS film [Ch-99]. The BS films were (a) SiO_2 and (b) $CoSi_2$. There is still a relatively large amount of stress in the samples in the temperature range 400 to 600 °C that was used in this study.

Stellenbosch University https://scholar.sun.ac.za

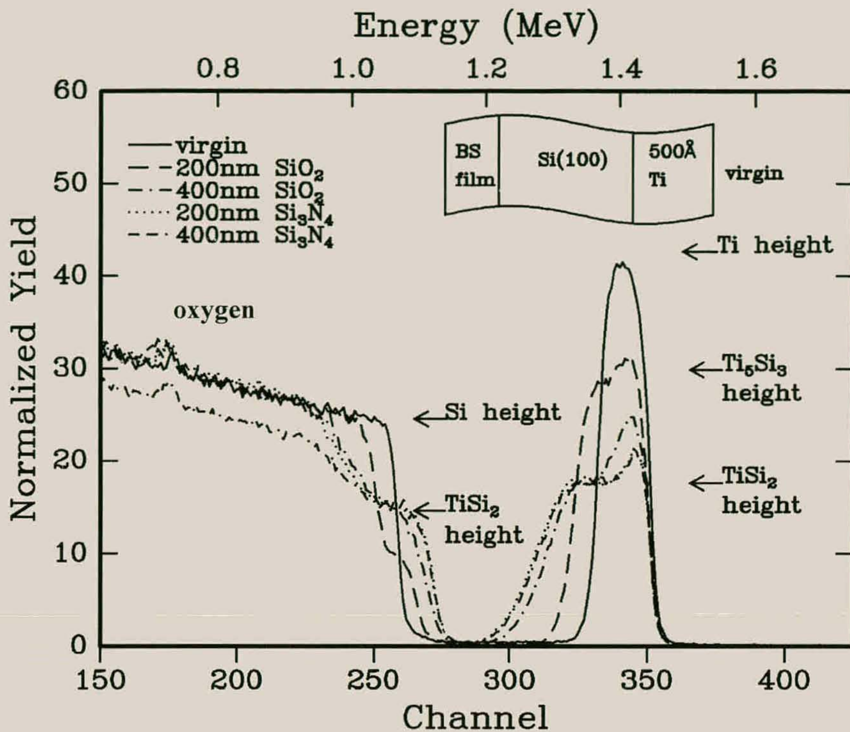

Fig. 4.8 RBS spectrum showing different amounts of $TiSi_2$ in the samples with different back side (BS) films after annealing at 600 °C for 10 minutes. The virgin sample had 500 Å of Ti. The oxide peak is also prominent at channel 175. A glancing angle RBS geometry was used to improve the resolution.

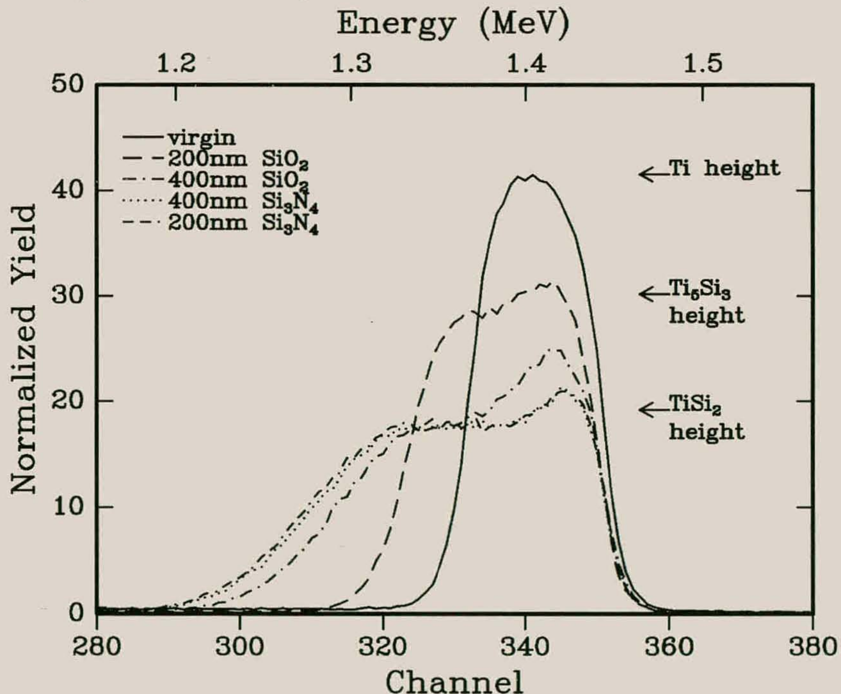

*Fig. 4.9 Blow up of the Ti peaks in **Fig. 4.8** showing different amounts of reaction for the samples with different back side films. All the samples have formed $TiSi_2$ except for the BS:200nm SiO_2 sample which has formed Ti_5Si_3. This was confirmed using XRD (see section on XRD analysis). Of the samples that formed $TiSi_2$ the BS: 400nm SiO_2 sample reacted the slowest.*

Stellenbosch University https://scholar.sun.ac.za

The RUMP simulations showed that both the samples with Si_3N_4 films deposited on the BS formed 1250Å of $TiSi_2$. The BS:400nm SiO_2 sample formed only 970Å of the di-silicide, while the BS:200nm sample did not form any $TiSi_2$ but 480Å of Ti_5Si_3. The virgin showed no signs of silicide formation. Although oxygen was present in the un-reacted Ti of all the annealed samples only the BS:200nm SiO_2 sample showed reflections from an oxide when analysed using XRD (see section on XRD analysis) **Fig. 4.10** shows the RBS spectrum of a BS:200nm Si_3N_4 sample that has been annealed for 10 minutes at 600°C. The overlaid RUMP simulation [Do-85] had the following structure: Si<100>/1200Å $TiSi_2$/160Å Ti+O. The simulation also showed 50at.% oxygen present in the un-reacted Ti thin film.

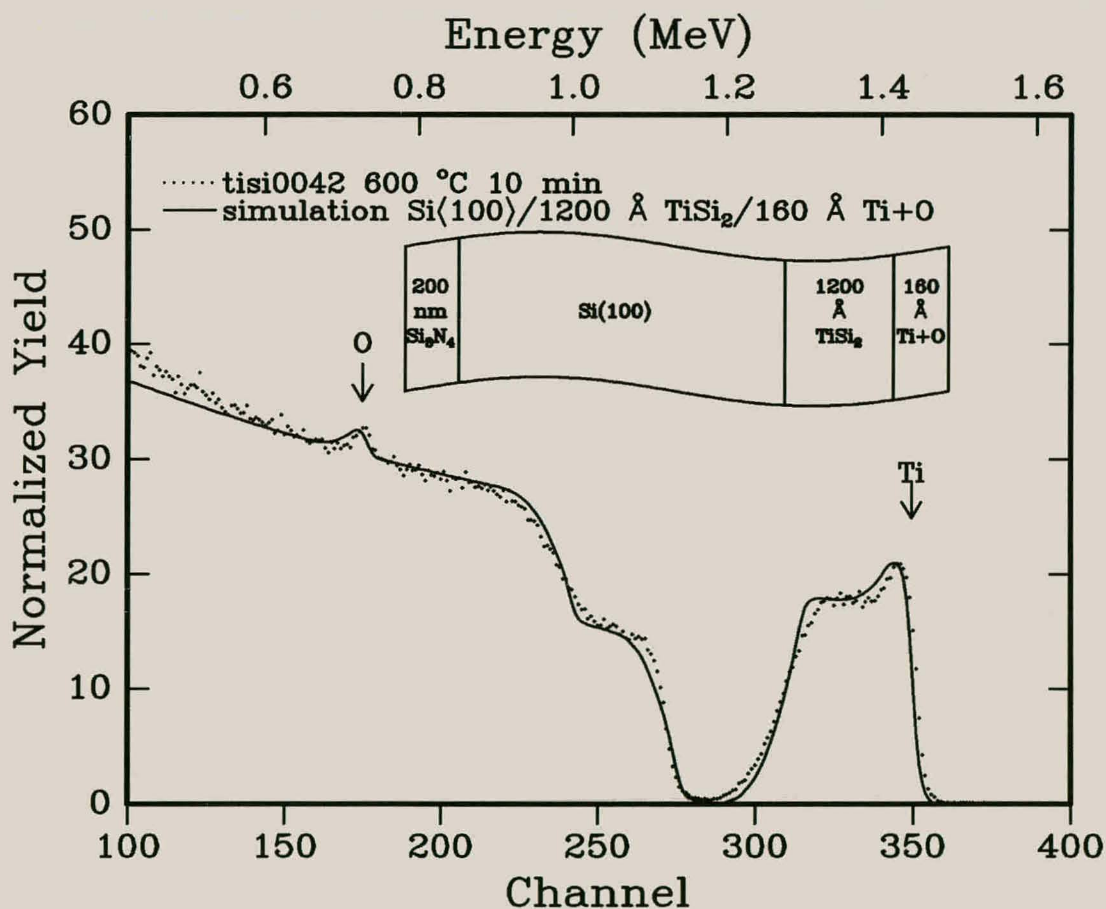

Fig. 4.10 RBS spectrum and RUMP simulation of sample with BS:200nm Si_3N_4 that has been annealed at 600°C for 10 minutes showing 1200Å of $TiSi_2$ formation.

Stellenbosch University https://scholar.sun.ac.za

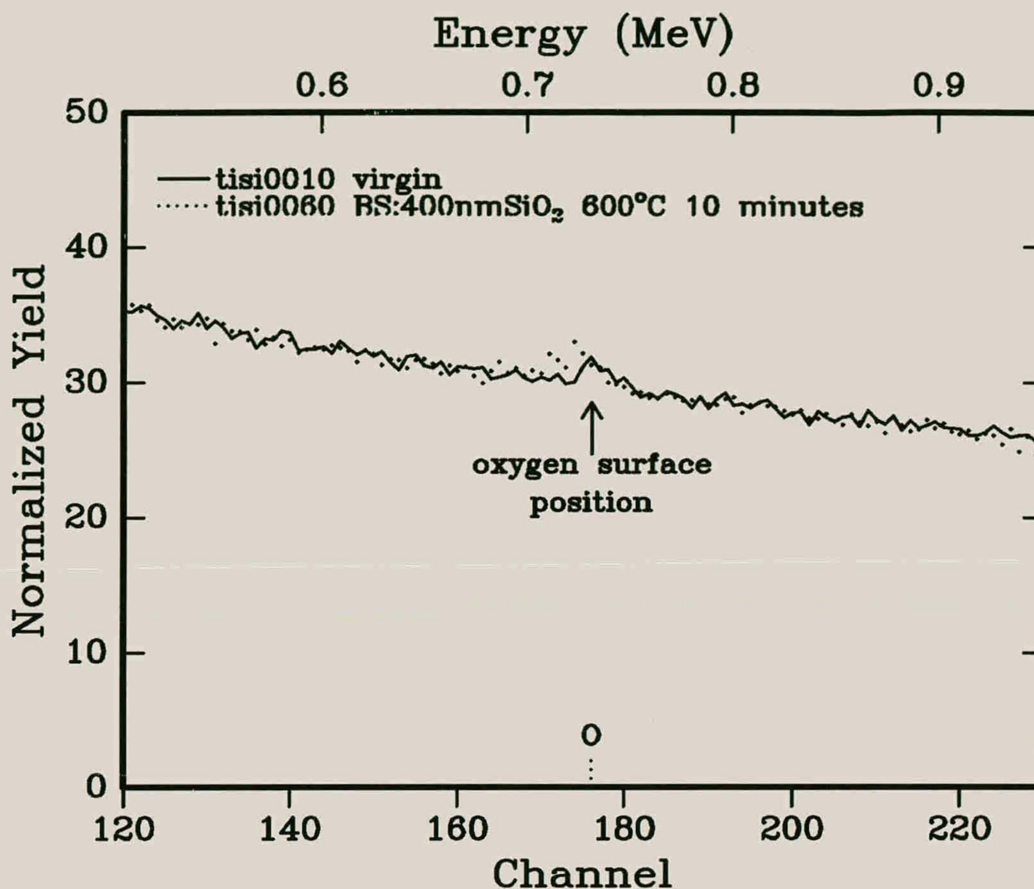

Fig. 4.11 Overlay of the oxygen peak in the virgin and annealed sample. The virgin sample showed a 30Å film of TiO_3 on the surface while in the annealed samples the oxygen has diffused throuhgout the Ti film. The oxygen diffusion can be seen by the broadening of te oxygen signal in the annealed sample.

Fig. 4.12 and **4.13** show the non linear growth of the silicides as a function of time at 450 and 600 °C for all four sample groups. Both sample groups with the Si_3N_4 on the backside formed the same amount of $TiSi_2$ and reacted faster than those with 400nm of SiO_2 on the backside at all temperatures. The BS:200nmSiO_2 samples reacted the slowest of all and formed the Ti-rich Ti_5Si_3 phase instead of the di-silicide. All the samples showed the presence of oxygen in the un-reacted Ti films. In the virgin samples the oxygen was only on the surface in the form of a film with composition TiO_3. In the reacted samples the oxygen was present throughout the Ti film (see **Fig. 4.11**). The oxygen concentration increased throughout the Ti thin film as the annealing time increased from a few atom percent to excess oxygen.

Stellenbosch University https://scholar.sun.ac.za

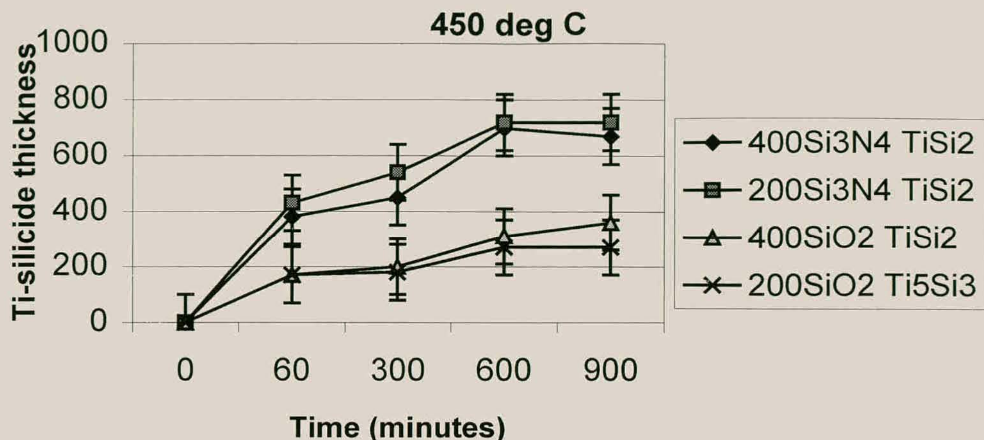

Fig. 4.12 Ti-silicide thickness versus time plots for the four different sample groups that have been annealed at 450 °C showing non-linear or diffusion limited kinetics. The two BS:Si_3N_4 sample groups always formed almost the same amount of $TiSi_2$ and always formed more disilicide than the BS:400nm SiO_2 samples. The BS:200nm SiO_2 always reacted the slowest and did not form the disilicide but the Ti-rich Ti_5Si_3 phase.

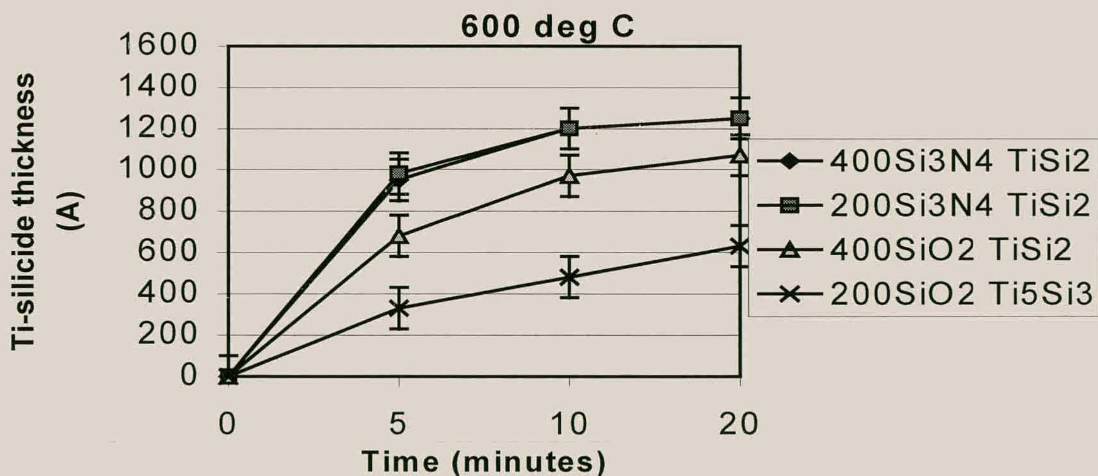

Fig. 4.13 Ti-silicide thickness versus time plots for the four different sample groups that have been annealed at 600 °C showing non-linear or diffusion limited kinetics. The two BS:Si_3N_4 sample groups always formed almost the same amount of $TiSi_2$ and always formed more disilicide than the BS:400nm SiO_2 samples. The BS:200nm SiO_2 always reacted the slowest and did not form the disilicide but the Ti-rich Ti_5Si_3 phase.

Stellenbosch University https://scholar.sun.ac.za

4.3.3. XRD analysis

There are two crystal phases with the same $TiSi_2$ composition. They are the metastable C49 (base-centred orthorhombic) low temperature phase and the stable C54 (face centred orthorhombic) high temperature phase. The low temperature C49 phase has a high resistivity (60 $\mu\Omega$ cm) while the C54 phase has a low resistivity (15 $\mu\Omega$ cm). In general it is found that upon annealing Ti-Si binary thin film couples the first crystalline disilicide to form below 650°C is the C49 phase followed by its conversion to the C54 phase above 650°C [Cl-92, Co-94]. The other phase which has also been reported as a first phase is the hexagonal Ti_5Si_3 phase (see **Appendix B**). If the disilicide forms as first phase the EHF model states that the effective concentration at the reaction interface is on the Si-rich side of the phase diagram (see **Fig. 4.1**). If the Ti-rich Ti_5Si_3 phase forms then the effective concentration is on the Ti-rich side of the phase diagram.

Fig. 4.14 to **4.17** shows the XRD spectra of a set of BS:400nmSiO_2, BS:400nmSi_3N_4 and BS:200nmSiO_2 samples that have annealed at 450, 550 and 600°C (see summary in **Table 4.2**). The virgin samples show no silicide reflections. In the reacted samples the C49 phase is present in the BS:400nmSi_3N_4, BS:200nmSi_3N_4 and BS400nmSiO_2 samples whereas Ti_5Si_3 is present in the BS200nmSiO_2 samples. In both samples that formed $TiSi_2$ only the C54 phase is present at 650 °C (see **Fig. 4.18**). **Fig. 4.15** to **Fig. 4.17** show less reaction in the BS: 400nm SiO_2 samples than in the BS: 400nm Si_3N_4. In **Fig. 4.15** there has not grown enough silicide in the BS: 400nm SiO_2 film to be detected while there is already a strong C49 reflection in the BS: 400nm Si_3N_4 sample. The XRD results therefore agree with the RBS, that the reaction in the BS:400nm SiO_2 samples is slower than the in the BS:400 Si_3N_4 samples throughout the temperature range 450 to 600°C. XRD also shows that the only $TiSi_2$ phase to form in this temperature range was the C49 phase which cancels out the possibility that the differences in growth rates was due to either phase transitions between the C49 and the C54 phases or the growth of both phases simultaneously. Although RBS showed the presence of oxygen in the un-reacted Ti in all the annealed samples XRD only showed oxide reflections in the BS:200nmSiO_2 samples (see **Table 4.2**). These reflections were from the hexagonal Ti_6O phase.

Stellenbosch University https://scholar.sun.ac.za

Table 4.2 Summary of the XRD results showing which phases formed in the different sample groups at different temperatures.

Temp and time	BS:400nm Si_4N_4	BS:200nm Si_4N_4	BS:400nm SiO_2	BS:200nm SiO_2
450°C 15 hours	$TiSi_2$(C49)	$TiSi_2$(C49)	$TiSi_2$(C49)	Ti_5Si_3, Ti_6O
550°C 20 minutes	$TiSi_2$(C49)	$TiSi_2$(C49)	$TiSi_2$(C49)	Ti_5Si_3, Ti_6O
600°C 20 minutes	$TiSi_2$(C49)	$TiSi_2$(C49)	$TiSi_2$(C49)	Ti_5Si_3, Ti_6O
650°C 30 minutes	$TiSi_2$(C54)	$TiSi_2$(C54)	$TiSi_2$(C54)	

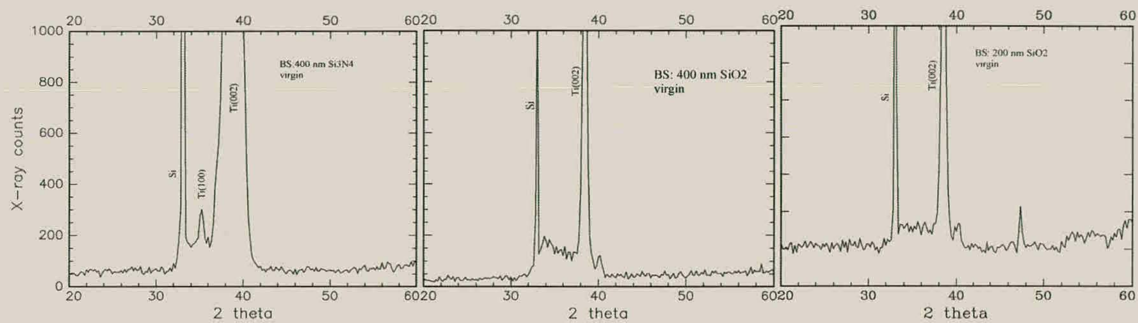

Fig. 4.14 XRD spectra of virgin samples with different BS layers taken in θ-2θ geometry. Reflections from the Ti film and the Si substrate are present.

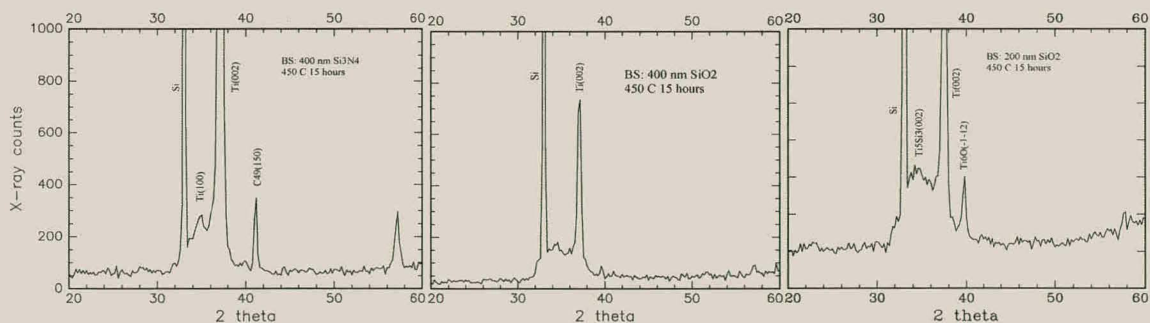

Fig. 4.15 XRD spectra of three samples with different BS layers annealed at 450 °C taken in θ-2θ geometry. Not enough silicide has formed in the BS: 400nm SiO_2 sample to be detected although the BS: 400nm Si_3N_4 and BS: 200nm SiO_2 samples already show reflections from the $TiSi_2$(C49) and Ti_5Si_3 phases respectively.

Stellenbosch University https://scholar.sun.ac.za

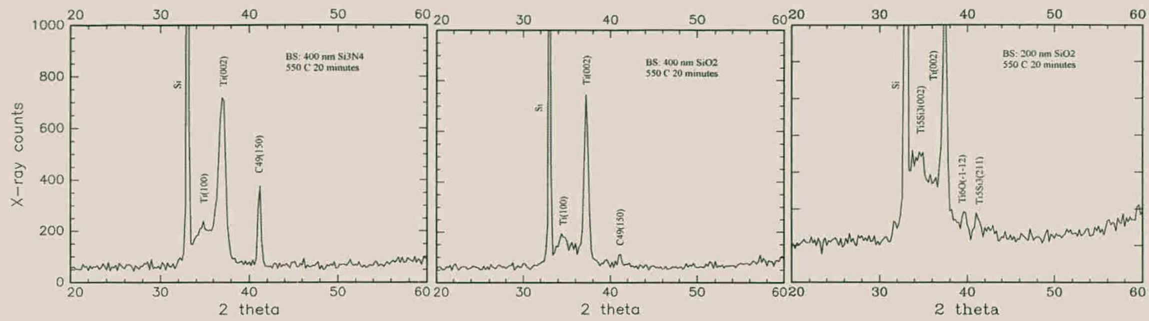

Fig. 4.16 XRD spectra of three samples with different BS layers annealed at 550 ^oC taken in θ-2θ geometry. Less of the C49-$TiSi_2$ phase has formed in the BS: 400nm SiO_2 sample than in the BS 400nm Si_3N_4 sample. Ti_5Si_3 and Ti_6O are present in the BS: 200nm SiO_2 sample.

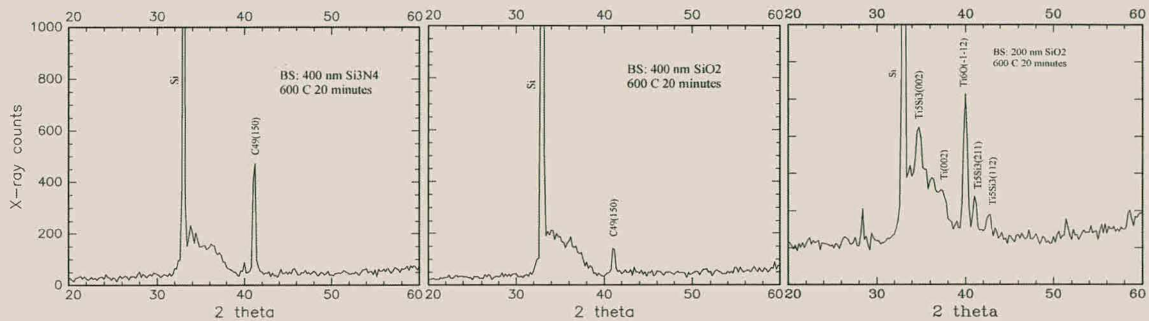

Fig. 4.17 XRD spectra of three samples with different BS layers annealed at 600 ^oC taken in θ-2θ geometry. More $TiSi_2$(C49) has again grown in the BS:400nm Si_3N_4 sample than the BS: 400nm SiO_2 sample with Ti_5Si_3 the only silicide present in the BS: 200nm SiO_2 sample.

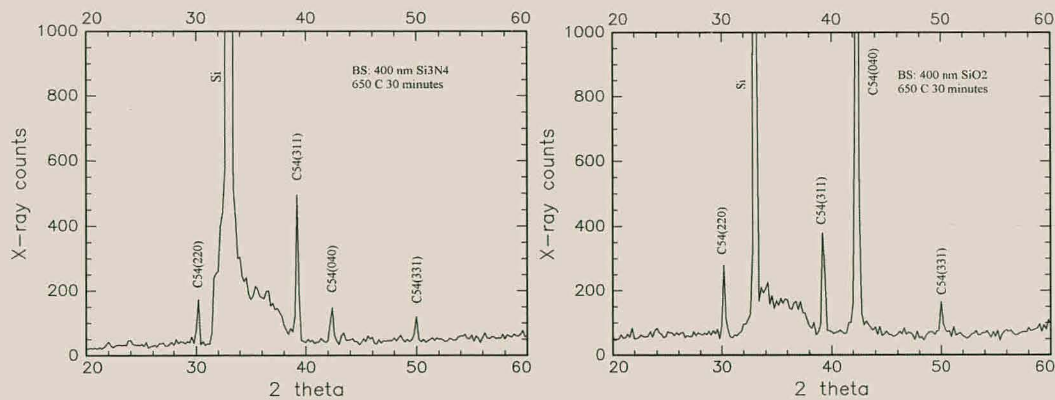

Fig. 4.18 XRD spectra of two samples with different BS layers annealed at 650 ^oC taken in θ-2θ geometry. Both samples just show the high temperature $TiSi_2$(C54) phase.

Stellenbosch University https://scholar.sun.ac.za

4.3.4. Effect of capping films on $TiSi_2$ formation

Oxidation of the Ti thin film during Ti-silicide formation makes accurate kinetic measurement very difficult. Initialy the two reactions do not effect each other but as reaction progresses the combination of the oxygen building up at the silicide/Ti interface (snow plough effect) and the consumption of Ti by the oxidation process on the surface results in the slowing down of the silicide growth rate. Oxygen can enter the system in two stages of the sample processing. The first stage is during the deposition of the Ti thin film and the second stage is during the annealing. RBS showed that the virgin samples had a 30 to 50Å film with composition TiO_3 on the surface (see **Fig. 4.11**). After annealing oxygen was measured throughout the thickness of the Ti film. The amount of oxygen increased as annealing time increased. An experiment with Al_2O_3 and Ti-oxide capping films was carried out to investigate their effectivity in limiting the influence of oxygen on the kinetics of $TiSi_2$ formation. Three sets of sample were prepared with between 700 and 750 Å of Ti deposited onto Si<100> substrates in an e-beam vacuum deposition system with a base pressure of 10^{-7} Torr. One set was then capped with a 720Å Al_2O_3 film while another was capped with a thin (<100Å) film of Ti-oxide. The Ti-O deposition was done by bleading oxygen (10^{-5} Torr) into the chamber while depositing Ti. The third control set of samples had no capping layer. These samples were then annealed at 600°C for between 5 and 30 minutes (see **Fig. 4.19**) in a vacuum furnace at a pressure of less than 2×10^{-7} Torr.

Fig. 4.19 shows that the samples with the Ti-O cap react the fastest to form $TiSi_2$ (C49 phase) and the samples with no cap react the slowest. RBS also showed that the samples with a Ti-O cap reacted the fastest (see **Fig. 4.20**). The Ti-O cap therefore seems to be the best cap of the two. Al_2O_3 does not react with oxygen and therefore only acts as a diffusion barrier during the annealing process. The Ti-O cap however seems to form a gettering sight which cleans up the Ti film of oxygen acquired during the deposition process and also forms a barrier for atmospheric oxygen in the furnace. This is similar to the Hf cap used in the lateral diffusion studies discussed in **chapter 5**. Although it seems that the caps did limit the effect of oxidation RBS still showed the presence of oxygen in the annealed samples.

Stellenbosch University https://scholar.sun.ac.za

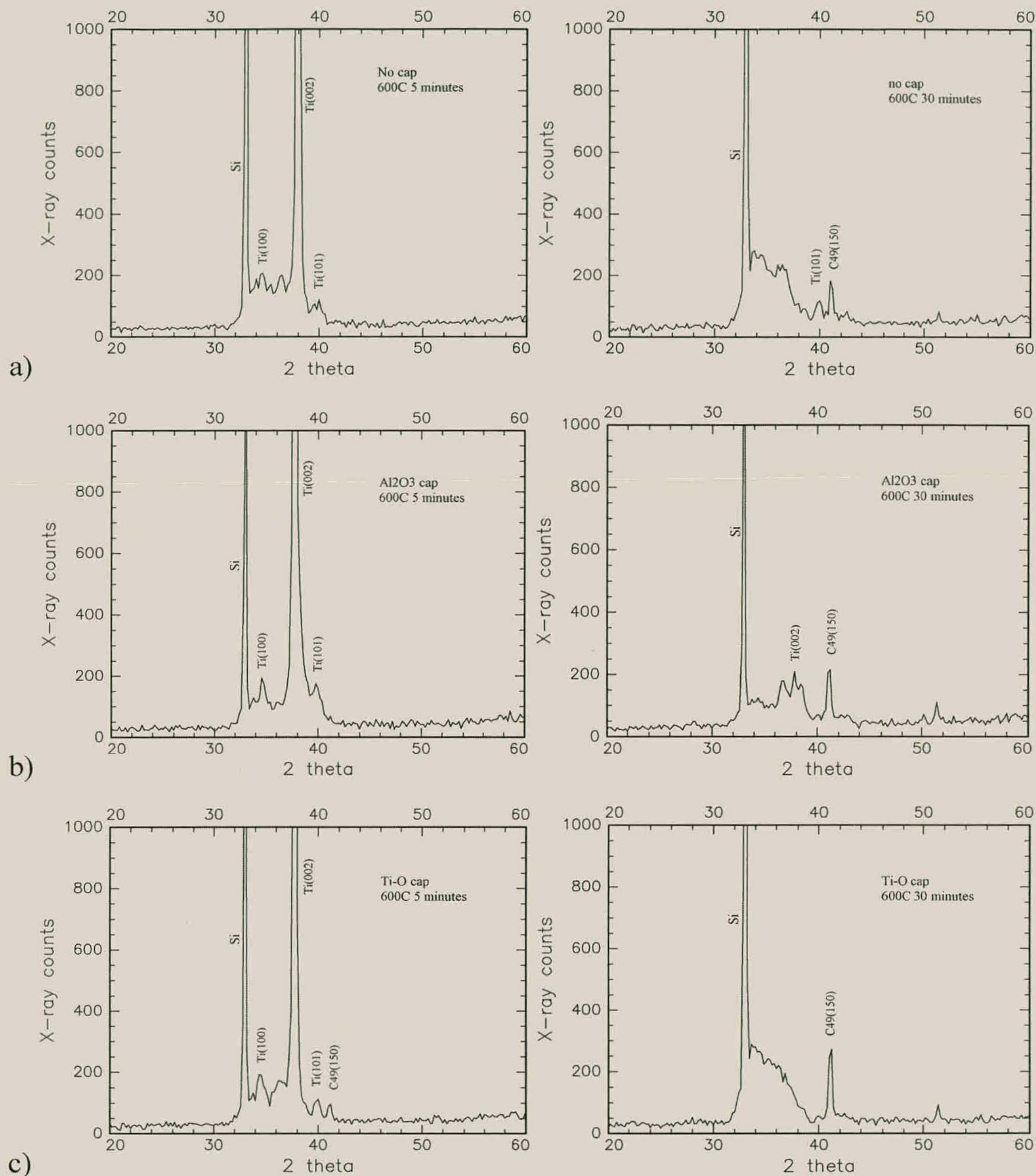

Fig.4.19 XRD spectra showing phase formation at 600°C in samples with different capping layers. In the samples with no capping layer (a) $TiSi_2$(C49) just started forming after 30 minutes. In samples with an Al_2O_3 capping layer (b) after 30 minutes the $TiSi_2$(C49) phase formed and there was still some Ti metal left. The C49 peak is larger than in the similarly annealed sample with no cap. In the samples with a Ti-oxide capping layer (c) the $TiSi_2$ (C49) phase had already formed after 5 minutes. After 30 minutes all the Ti was consumed showing that the Ti-O cap is more effective at limiting oxidation than the Al_2O_3 cap.

Stellenbosch University https://scholar.sun.ac.za

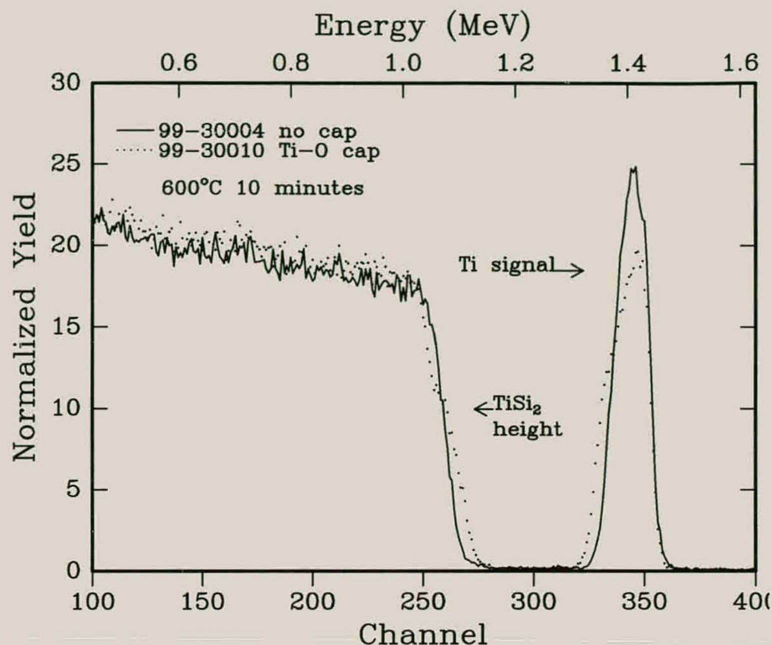

Fig. 4.20 RBS spectra showing how a Ti thin film reacts faster with Si(100) when covered with a Ti-O cap to form $TiSi_2$. The sample without any cap shows very little reaction while the sample with the Ti-O cap already has a definite shoulder corresponding to $TiSi_2$.

4.3.5. Discussion

XRD analysis showed that the $TiSi_2$(C49) phase formed and grew in the BS:400nm Si_3N_4, BS:200nm Si_3N_4 and BS:400nm SiO_2 samples whereas in the BS:200nm SiO_2 samples the Ti_5Si_3 phase formed as first phase and continued to grow. Previous studies have shown Si to be the dominant diffusing species during $TiSi_2$ formation [Bo-82, Ni-83]. In some of these studies radioactive Si tracer experiments have shown a very high mobility of Si in TiS_2 and that silicon diffusion takes place by a vacancy mechanism [Bo-82] which could indicate linear kinetics. Both non-linear (diffusion limited) [Hu-83, Pi-88] as well as linear (reaction limited) [Pi-88] $TiSi_2$ kinetics have been reported in the literature. A possible reason for this inconsistency is that Ti oxidises very easily. This means that as the silicide is formed the oxides are piled up at the interface forming a snow plough effect which limits the access of Ti to Si thereby slowing down the silicide formation. The Ti_5Si_3 phase is reported to grow with linear or diffusion limited kinetics [Ma-95]. In this study non-linear kinetics gave the best fit to the data and therefore **Fig. 4.21** shows plots of $TiSi_2$ and Ti_5Si_3 thickness versus square root of time for the BS:200nm Si_3N_4 and BS:200nmSiO_2 samples that were been annealed at 450, 500, 550 and 600 °C. The relatively poor fit to the data in some cases is due to the effect of the oxygen which could be seen in the

Stellenbosch University https://scholar.sun.ac.za

RBS spectra (see **Fig. 4.8** and **4.11**). The virgin samples only showed surface oxygen whereas the annealed samples showed oxygen throughout the Ti film even at 450°C. Different capping films were used to try and limit the effect of oxidation (see **Fig. 4.20**). Even though a Ti-oxide cap did increase the reaction rate the effect of oxidation could not be eliminated.

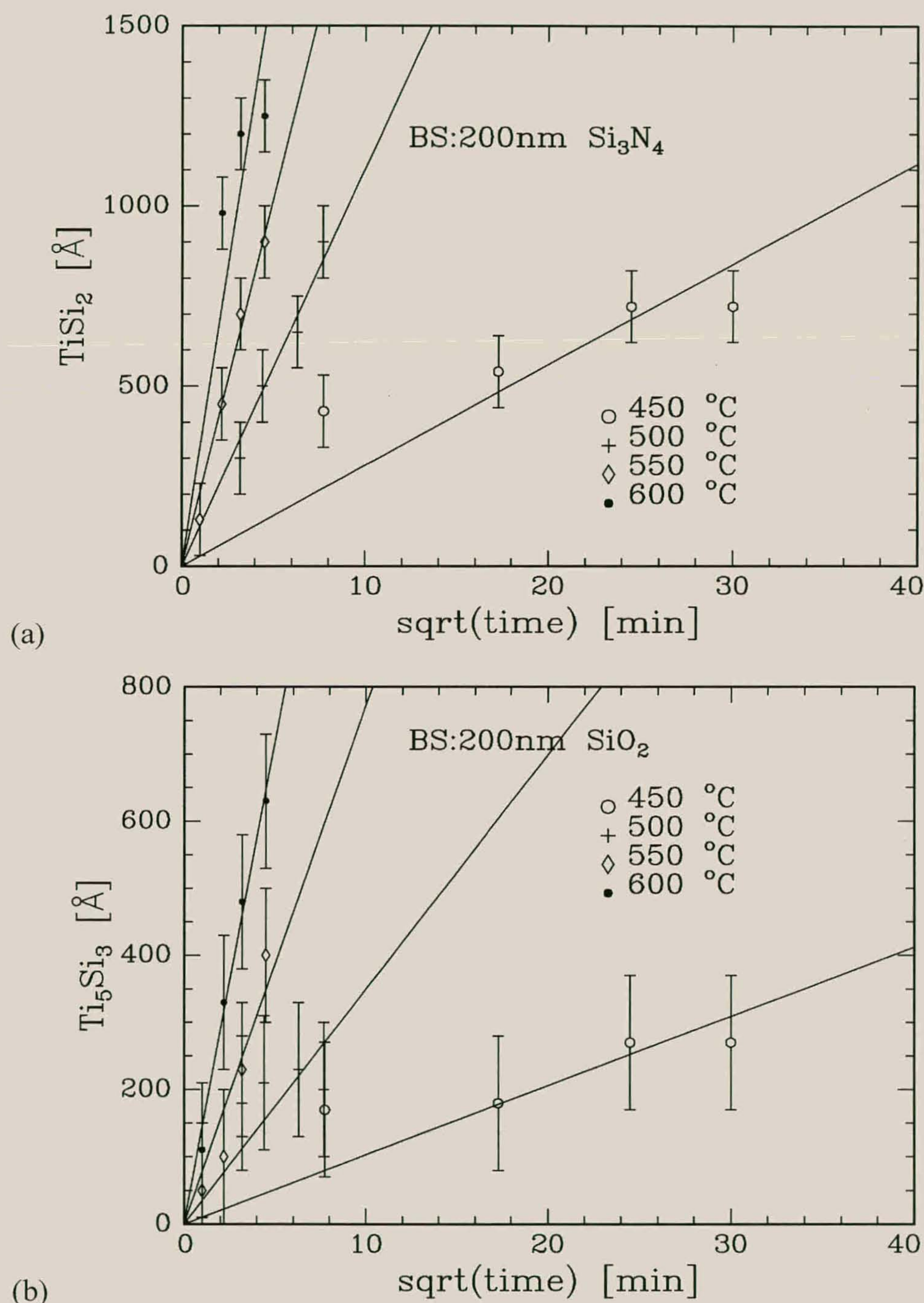

Fig. 4.21 Plots of (a) $TiSi_2$ thickness versus square root of time and (b) Ti_5Si_3 thickness versus square root of time, for the samples with 200nm of Si_3N_4 and 200nm of SiO_2 respectively deposited on the backside. Some of the straight line fits were relatively poor. This is due to the retarding effect of the oxygen absorbed in the un-reacted Ti-films.

Stellenbosch University https://scholar.sun.ac.za

Fig. 4.22 shows the Arrhenius plots of the Ti-silicide formation which took place in the four sample groups. Ideally a control sample group would have been made which had no BS film to induce stress. Unluckily due to the high work load of the manufacturing laboratories this could not be done in time. The activation energy for the $TiSi_2$ formation (gradient of the Arrhenius curve) varied between 2.1 and 2.2 eV in all three the sample groups which formed the disilicide. The activation energy of the Ti_5Si_3 phase was slightly smaller at 1.9eV. The reaction rates for the $TiSi_2$ formation in the two sample groups with Si_3N_4 deposited on the BS are basically the same. The two BS:Si_3N_4 curves therefore lie within the experimental error of each other. The reaction rate for the formation of $TiSi_2$ in the 400nm SiO_2 samples is almost half that of the BS:Si_3N_4 samples (see **Table 4.3**) and therefore this line lies below the previous two lines. This means that the samples with a tensile stress in the BS film react faster than those with a compressive stress. The Ti_5Si_3 reacts the slowest and therefore its line lies at the bottom and at a slightly different angle due to the slightly smaller activation energy of this phase. The sample group which formed the Ti_5Si_3 phase had the largest compressive stress in the BS film. The measured activation energy for $TiSi_2$ corresponded well with the values reported in the literature of 2.1eV [Cl-92] and 1.8eV [Hu-83]. The fact that the activation energy stays constant in the sample groups that formed $TiSi_2$(C49) indicates that there is not a change in the reaction mechanism but only a change in the speed of the process. Previous research shows the Si diffusion mechanism in $TiSi_2$ to be vacancy diffusion [Bo-82]. In a recent article Cheng et. al. [Ch-99] reported on the effect of stress induced by backside deposition on the growth of $TiSi_2$ on Si<100> wafers. Although he did not measure the total kinetics as a function of stress in the backside film he did find that as the stress went from tensile (+870 MPa) to compressive (-550 MPa) the $TiSi_2$ thickness formed would decrease with as much as 50 % after annealing for 30s at temperatures between 650-800 ^{o}C. This is in agreement with the trends observed in this study in which even greater stress effects are seen. The larger effects reported in this study can be explained using **Fig. 4.7**, which shows that the stress in the BS film decreases as temperature is increased. The samples would therefore be more stressed in the lower temperature range used in this study (450-600°C) than those used by Cheng (650-800°C). It is important to realise that if the BS film is under compressive stress the Si wafer at the BS-interface is under tensile stress. The opposite side of the

Stellenbosch University https://scholar.sun.ac.za

wafer (where the Ti is deposited) is again under compressive stress (see **Fig. 4.2**). This is because the substrate is much thicker than the backside film and can be assumed to have zero stress in the middle (see **Appendix A**). Cheng argued that compressive stress on the front surface would lead to a loss in vacancies in order to try and counter the increase in pressure. Tensile stress on the other hand would lead to an increase in vacancies to accommodate the increase in volume. As the $TiSi_2$ grows with a vacancy diffusion mechanism [Bo-82] a compressive stress would retard the diffusion of Si atoms (by limiting the amount of vacancies) and tensile stress would enhance the diffusion of Si atoms (by increasing the amount of vacancies). This agrees with our result of a constant activation energy and a decreasing reaction rate as stress becomes more compressive (see **table 4.3**) which implies no change in reaction mechanism only a change in the rate at which the silicide grows.

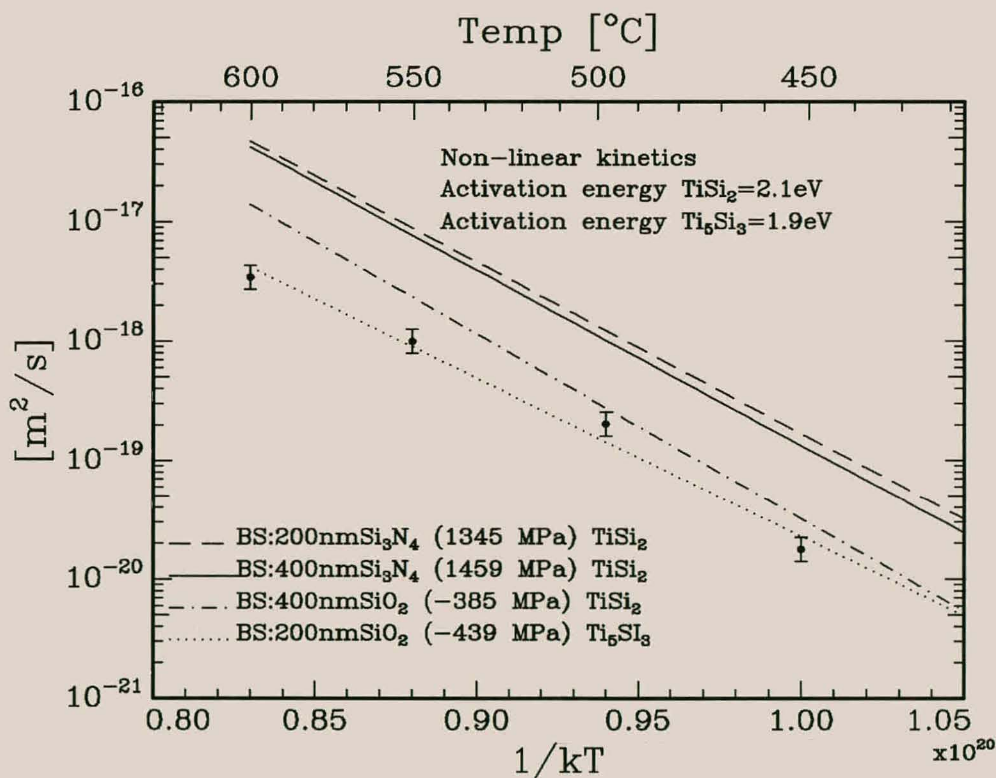

*Fig. 4.22 Arrhenius plots for the four different stress situations. The measured stresses in the backside film is also shown on the figures. The activation energies are the same for all the samples which formed $TiSi_2$ while the activation energy for the Ti_5Si_3 phase was a bit smaller. The more compressive (negative) the stress the more the reaction rate decreases. The activation energy of the $TiSi_2$ phase corresponded well with reported values in the literature [Cl-92, Hu-83] (see **table 4.3**). A literature search showed that the Ti_5Si_3 phase has previously been found to grow with diffusion limited kinetics [Ma-95]. No references to the activation energy could however be found. The actual data points are only shown for the Ti_5Si_3 phase.*

Stellenbosch University https://scholar.sun.ac.za

Table 4.3 Table showing the measured stress in the back side film before the FS deposition (negative=compressive, positive=tensile), the activation energy and reaction rate for each sample at 500 °C. The data was analysed for non-linear or diffusion limited ($t^{1/2}$) kinetics.

Sample group	Stress at BS film (Mpa)	Phase	Activation energy (eV) ($t^{1/2}$)	Reaction rate @500°C (m^2/sec)
BS:200 nm Si_3N_4	+1345	$TiSi_2$	2.1±0.2	1.6×10^{-18}
BS: 400nm Si_3N_4	+1459	$TiSi_2$	2.1±0.2	1.3×10^{-18}
BS:400 nm SiO_2	-385	$TiSi_2$	2.2±0.2	7.9×10^{-19}
BS:200 nm SiO_2	-439	Ti_5Si_3	1.9±0.2	1.6×10^{-19}

As discussed before three phases have been reported to compete to form as first phase in this system. They are Ti_5Si_3, TiSi and $TiSi_2$ where TiSi is a non-congruently melting phase that will probably have a barrier to nucleation. This is in agreement with the EHF model as the two liquidus minima (both at 1330 °C) makes it such that there is little to choose thermodynamically between any of the phases on the phase diagram. In the situations where $TiSi_2$ has formed the effective concentration at the reaction interface is therefore on the silicon rich side of the phase diagram (**Fig. 4.1**). In the sample group BS:200nm SiO_2 the Si supply has been slowed down so effectively by the compressive stress that the effective concentration has moved toward the Ti-rich side of the phase diagram where the Ti_5Si_3 phase is thermodynamically more viable (see EHF diagram **Fig. 4.1**).

Appendix A shows that after the BS deposition the stress in the substrate is three orders of magnitude smaller than in the BS film. This is because the substrate is of the order 1000 times thicker than the BS film. The force and moment equilibrium at the interface then equates to a stress which is force per area that is of the order of 1000 times smaller in the thick substrate than in the thin film. The same can be said after the FS deposition. The stress measured in the FS film was smaller than the stress measured in the BS film after the first deposition. The curvature of the substrate after the FS deposition (second deposition) is a linear combination of the effects of both depositions. The final stress in the thin film is therefore also a linear combination of

Stellenbosch University https://scholar.sun.ac.za

the stress induced by the two depositions. The final stress is very small (see **Appendix A**) and it could be argued that it is too small to induce such a large effect on the kinetics of the $TiSi_2$ formation. The actual stress in the growing silicide thin film is however unknown. The just formed silicide is very thin and the stress in it might be relatively large. Seeing as we do not understand the mechanism with which stress influences the growth process we cannot judge what is a large or small value for stress.

4.4. Summary and conclusions

The main aim of this study was to investigate the effect of stress on Ti-silicide formation by depositing Ti films onto silicon substrates that were under different amounts of stress. The stress in the silicon was induced by depositing a film with a different thermal expansion coefficient to silicon on the Back Side (BS) of the substrate. As the sample cools after deposition the substrate deforms (strain) inducing stress throughout the sample structure (see **Fig. 4.2**). Samples were prepared with varying amounts of stress in the Si substrate by varying the thickness and type of BS film. SiO_2 BS films caused compressive stress in the surface of the Si substrate while Si_3N_4 films caused tensile stress in the surface of the Si substrate (see **Appendix A**). Ti thin films (500Å) were deposited onto the Front Side (FS) of these stressed substrates and annealed to induce reaction. The temperatures used were 450 to 600°C. **Fig. 4.7** shows that the stress in similar systems is almost totally relaxed at temperatures above 600°C [Ch-99].

Two sets of samples were manufactured with 400 and 200nm of Si_3N_4 on the BS respectively. These samples both had tensile stress in the FS of the substrate. XRD and RBS showed that both these sample groups formed only the $TiSi_2$(C49) phase up to 600°C and the $TiSi_2$(C54) formed above 650°C (see section on XRD analysis). Two further sample groups were manufactured with 400 and 200nm of SiO_2 on the BS. The BS:400nm SiO_2 sample group also formed $TiSi_2$(C49) up to 600°C and $TiSi_2$(C54) at 650°C while the BS:200nm SiO_2 formed the Ti_3Si_5 phase up to 600°C. Kinetic measurements of the phase formation (see **table 4.3**) showed that the samples which had tensile stress in the BS films (1345 to 1459MPa) formed $TiSi_2$(C49) much

Stellenbosch University https://scholar.sun.ac.za

faster than those with compressive stress in the BS films (-385MPa). This can clearly be seen in **Fig. 4.12** and **4.13** where the BS:400nm SiO_2 curve lies below the two BS:Si_3N_4 curves for all annealing times and temperatures. The kinetics of theTi_5Si_3 phase in the BS:200nm SiO_2 sample group, which had the largest compressive stress in the BS film (-439MPa) was the slowest of all. Arrhenius curves (see **Fig. 4.22**) showed that the activation energy of the three sample groups which formed $TiSi_2$ was very similar at about 2.1eV, which corresponded well with results found in the literature [Cl-92, Hu-83]. Only the pre-exponential factor varied with changing stress (see **Table 4.3**), which implies that the reaction mechanism does not change only the reaction rate. The activation energy of the Ti_5Si_3 phase was a little smaller at 1.9eV but still compared to the $TiSi_2$ activation energy within the statistical error. The pre-exponential factor was drastically smaller though resulting in much less silicide formation.

In **Appendix A** it is shown that while the stress in the BS films was relatively large the stress at the surface of the Si wafer after the BS deposition was three orders of magnitude smaller but still the same polarity. Cheng et. al. [Ch-99] argued that such compressive stress in the surface of the Si wafer would lead to a loss in vacancies as the system tried to accommodate the increased pressure and tensile stress would likewise lead to an increase in vacancies as the system tried to accommodate the increase in volume. He further argued that as $TiSi_2$ grows with a vacancy diffusion mechanism a compressive stress would therefore retard growth and a tensile stress would speed up growth. This would agree with our result that the reaction mechanism does not change as the stress goes from compressive to tensile only the reaction rate. It also agrees with the result that the samples with a compressive stress in the BS film (compressive stress in the substrate surface) react slower than those with a tensile stress in the BS film (compressive stress in the substrate surface). In the case of the BS:200nm SiO_2 samples the compressive stress was so large that the lack of vacancies moved the effective concentration at the reaction interface towards the Ti-rich side of the phase diagram making Ti_5Si_3 thermodynamically the more viable phase. This can be seen from the EHF diagram (see **Fig. 4.1**) where the Ti_5Si_3 phase triangle shows that this phase leads to the highest change in free energy in the Ti-rich region of the phase diagram as Ti_5Si_4 is a non-congruently melting phase and therefore would not

Stellenbosch University https://scholar.sun.ac.za

generally form as a first phase in a silicide system. For this model to be true it would imply the following two points.

1. The $TiSi_2$ reaction kinetics are diffusion limited because if they were reaction limited then speeding up or slowing down the diffusion would not influence the reaction rate without changing the reaction mechanism
2. The stress in the forming silicide is the same polarity as the stress in the surface of the substrate before the Ti film is deposited, as this is where the diffusion takes place. The silicon substrate only supplies the diffusing species.

The stress calculated in the Ti thin film and the surface of the Si substrate after the FS deposition is much smaller than after the BS deposition (see **Appendix A**). It could be argued that these stress values are too small to have any effect on the silicide formation. The actual stress in the growing silicide is however unknown. The just formed silicide film is very thin and due to the force equilibrium on either side of the silicide/substrate interface the stress experienced (force per area) in the thin film might be relatively large.

A Ti-oxide capping layer seemed to limit surface oxidation, which is a constant problem in the Ti system. It was found that a Ti-oxide capping layer speeded up the formation of $TiSi_2$ as can be seen in **Fig. 4.20**. The Ti-oxide capping film was more effective than a Al_2O_3 capping film as it seemed to form a gettering site for oxygen in the Ti film acquired during the deposition process. The majority of groups have reported diffusion limited (non-linear) [Hu-83, Pi-88, Ma-95] growth kinetics for the $TiSi_2$ phase but linear or reaction limited kinetics have also been reported [Pi-88]. In all these experiments the reaction kinetics was derived from a thickness versus time plot. Any build up of oxygen at the reaction interface (snow plow effect) would slow down the reaction rate making the plot look non-linear. Radioactive Si tracer experiments done by Botha [Bo-82] show a very high mobility of Si in $TiSi_2$ and that silicon diffusion takes place by a vacancy mechanism which could indicate reaction controlled kinetics. Radioactive tracer measurements directly monitor the movement of the Si and are not influenced by surface oxidation or impurity build up at the reaction interface (snow plow effect). If the growth mechanism is reaction controlled then the stress must be having a direct influence on the reaction at the Ti/silicide interface and cannot be influencing the reaction by speeding up or slowing down the diffusion process as put forward by Cheng. Either that or the stress in the silicon itself

Stellenbosch University https://scholar.sun.ac.za

does influence the ability of the substrate to supply Si to the forming silicide. It would be useful to measure the stress in the forming silicide in. situ. as it is grown. This could shed more light on the possible mechanism by which stress influences phase growth.

Stellenbosch University https://scholar.sun.ac.za

5. Ru-Al, Pt-Al AND Cr-Si LATERAL DIFFUSION COUPLES

5.1. Introduction

Conventional bulk diffusion has been a topic of study for many years. These studies have addressed various technical problems encountered whenever two dissimilar materials are joined together. The discovery of the transistor in 1947 and the subsequent development of Si-transistor based technology in the 1950's that later developed into the commercial integrated circuit industry which first saw light in the early 1960's started a huge interest in thin film interactions. The modern integrated circuit is a complicated multilayer structure with more than 20 layers of metalisation. Lateral diffusion couples have been used in the development of these complicated structures. **Fig. 5.1** shows a structure in a device and a comparable lateral diffusion couple.

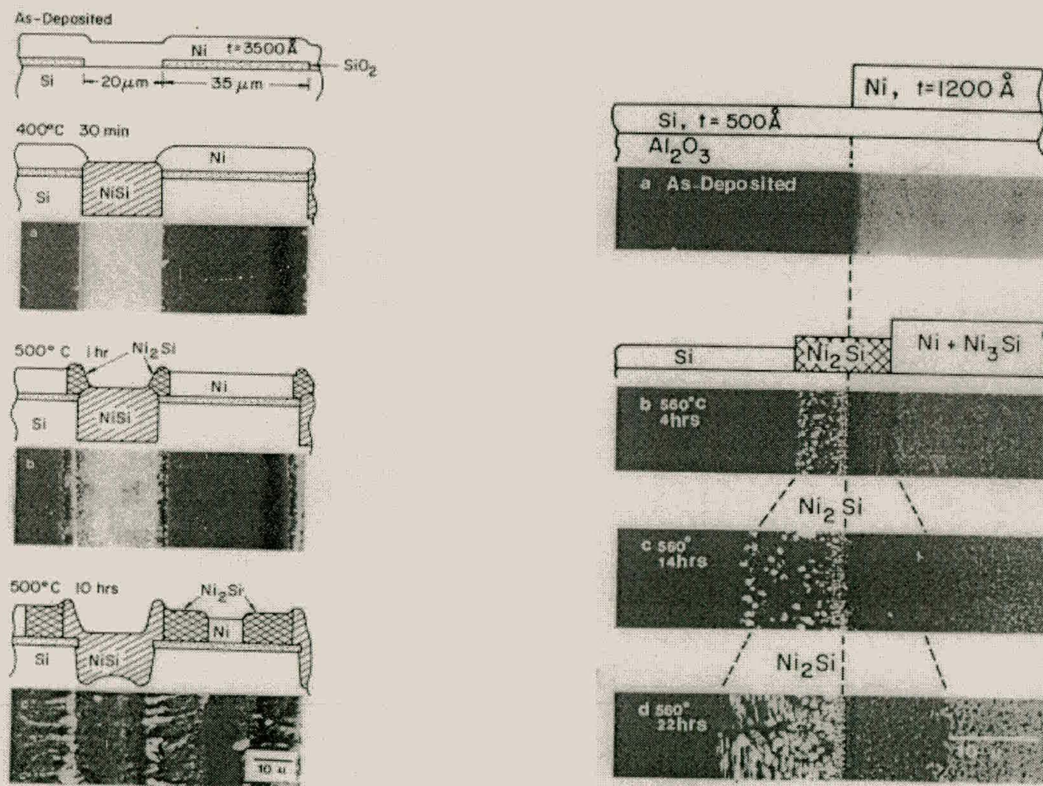

Fig. 5.1 SEM micrographs and schematic diagrams of silicide formation in a device structure (left) and a lateral diffusion couple (right) [Zh-82].

There are major differences between thin film and bulk diffusion couples. In thin film systems usually only one phase forms and grows at a time. The next phase only starts growing when one of the species has been consumed. In bulk diffusion couples a

Stellenbosch University https://scholar.sun.ac.za

variety of phases grow simultaneously in parallel layers. In bulk diffusion couples all the equilibrium phases are usually present. In thin film systems metastable phases are often reported and non-congruently melting phases usually do not form in metal silicide systems. Apart from their technological importance lateral diffusion couples with diffusion lengths of between fifty and several hundred micron act as a bridge between thin film and bulk diffusion regions. Depending on reacting species, lateral diffusion couples have been reported to have thin film and bulk characteristics. In many lateral diffusion systems several phases have been found to co-exist [Zh-83, Bl-92, Li-88] and in the Ni-Si system [Zh-83] the non-congruently melting Ni_3Si_2 phase forms which generally does not form in thin film systems. **Fig. 5.2** shows a typical example of a lateral diffusion couple. In this case an Al island deposited onto a Ru thin film on top of an oxidised Si wafer.

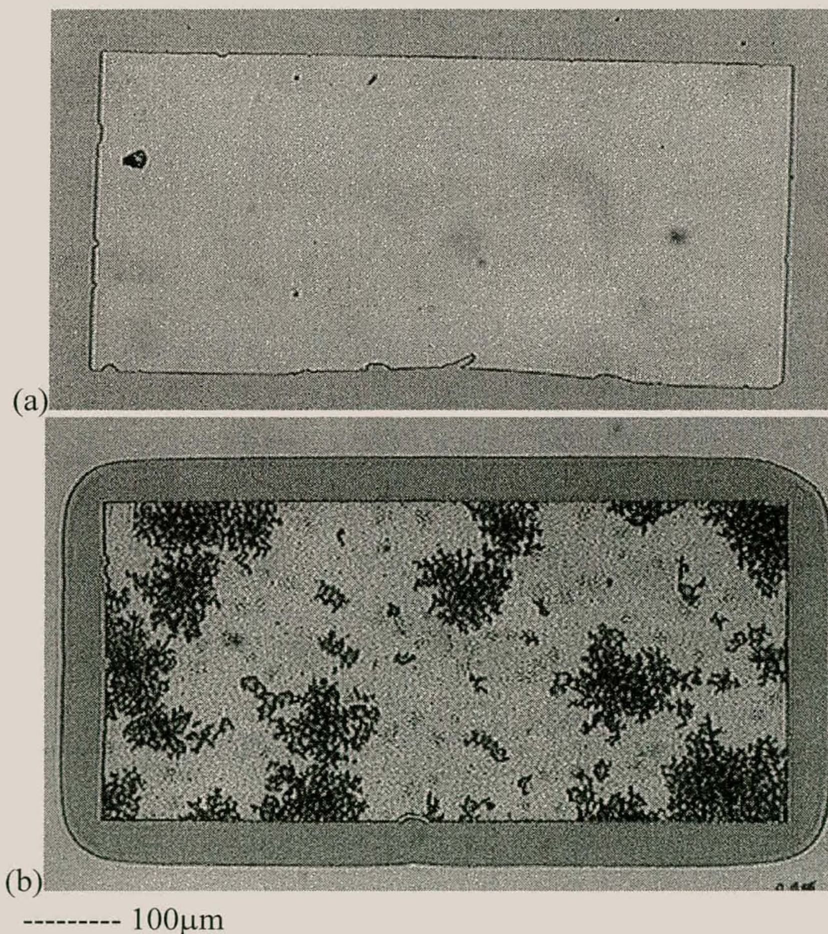

Fig. 5.2 Optical micrographs of a typical lateral diffusion couple before (a) and after annealing (b). The sample has an Al island (3800 Å) deposited onto a Ru thin film (300 Å) and was annealed for 29 hours at 550°C.

Stellenbosch University https://scholar.sun.ac.za

A literature search has shown that apparently no lateral diffusion studies have been carried out on the Ru-Al, Pt-Al and Cr-Si systems. There has only been one study carried out on a lateral diffusion system using a nuclear microprobe [Di-94]. In the past SEM and TEM have been used [Zh-83, Ch-85]. The Nuclear Micro Probe (NMP) has been used before to study lateral non-uniformities during reaction in Au-Al thin film systems [De-97]. The major advantage of doing RBS in the NMP is that it gives compositional information as a function of depth anywhere on the sampled area. This makes it possible to generate a three dimensional image of the sample.

5.2. Ru-Al system

5.2.1. Thin film couples

There are five equilibrium compound phases on the Ru-Al binary phase diagram, with the liquidus minimum on the far Al-rich side (**Fig. 5.3**). According to the EHF diagram shown in **Fig. 5.3** there is very little to choose thermodynamically between the phases $RuAl_6$, Ru_4Al_{13}, $RuAl_2$ and Ru_2Al_3 at the composition of the liquidus minimum. This would mean that any of the four could be expected as a first phase.

Fig. 5.4 shows XRD and RBS spectra of samples that have been annealed at 550 °C for various times. The virgin sample structure was: SiO_2/850 Å Al/2000 Å Ru which means that there is excess Ru in the system. The XRD spectra show that $RuAl_2$ and Ru_2Al_3 are definitely present in the annealed samples. It seems that these two phases coexist. The first phase seems to already be present in the virgin samples (the virgin was 1 year old when XRD was carried out) and could be either $RuAl_6$ or $RuAl_2$. It is difficult to say as the $RuAl_6$<314> line and the $RuAl_2$<115> line overlap. The $RuAl_2$<202> line (80% intensity in a powder sample) is not present in the virgin sample however, which probably means that $RuAl_6$ is the first phase to form followed by $RuAl_2$ and Ru_2Al_3 (see **Fig. 5.4**). Ru is in excess in this system and the Al is already consumed after 20 minutes. Previous studies did not find $RuAl_6$ as first phase [Wa-95] but as $RuAl_6$ does not grow to completion and already forms at room temperature it would not be noticed at the high temperatures that these studies (550 °C) were carried out at. It is important to note that the most ruthenium rich phase, RuAl is not detected even after annealing for 10 hours with excess ruthenium. This

Stellenbosch University https://scholar.sun.ac.za

implies some sort of nucleation barrier to the formation of the RuAl phase. A higher temperature could not be used as Al melts at 660 °C.

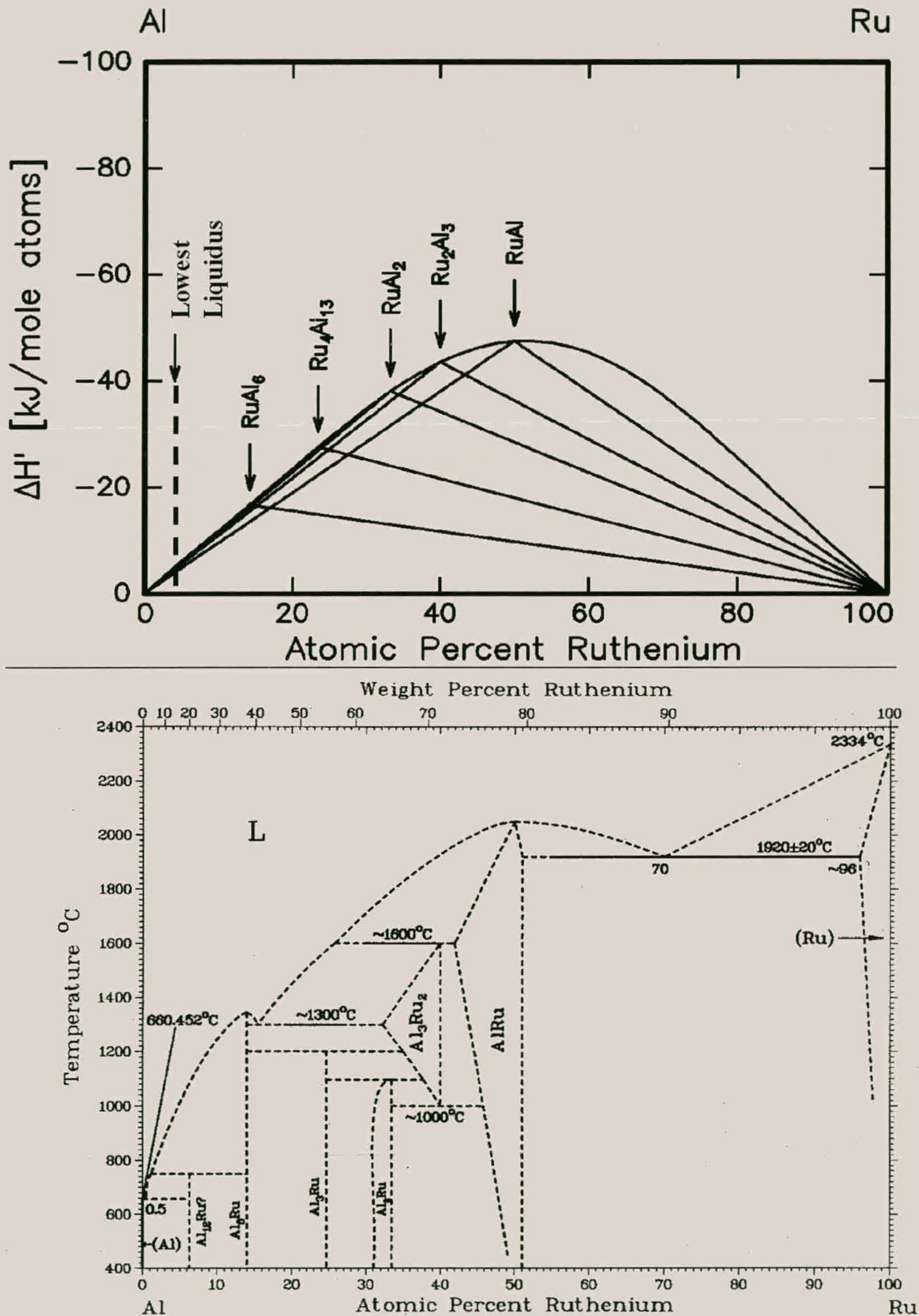

Fig. 5.3 EHF and phase diagram for the Ru-Al binary system, showing that at the liquidus minimum composition the effective heat of formation of $RuAl_6$, Ru_4Al_{13}, $RuAl_2$ and Ru_2Al_3 are nearly the same.

Stellenbosch University https://scholar.sun.ac.za

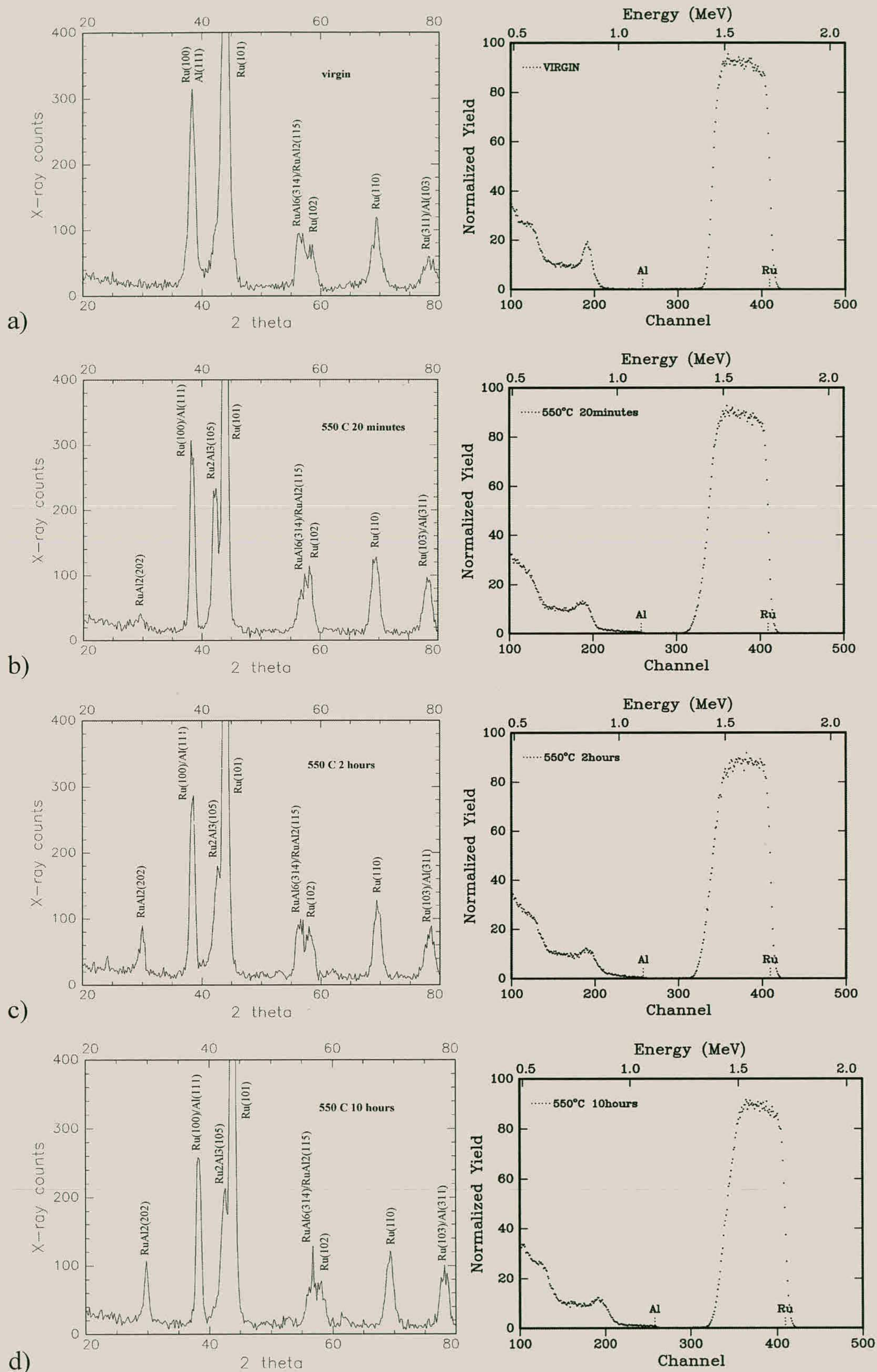

Fig. 5.4 XRD (left) and RBS (right) spectra of a series of samples with composition SiO_2/850 Å Al/2000 Å Ru before annealing (virgin) and after annealing at 550 °C for different times. It seems that $RuAl_6$ is the first phase to form followed by $RuAl_2$ and Ru_2Al_3. The Al is already consumed after 20 minutes.

Stellenbosch University https://scholar.sun.ac.za

Wang et. al. studied the Ru-Al thin film system in the situation where there is excess Al [Wa-95]. In their case the Al contained 0.8 wt.% Si. Annealing at 550 °C resulted in the formation of a mixture of $RuAl_2$ and Ru_4Al_{13}. To summarise the results of both studies; if the system has excess Al then $RuAl_2$ and Ru_4Al_{13} will form and if the system has excess Ru then $RuAl_2$ and Ru_2Al_3 will form. The results of this study are summarised in **table. 5.1**.

Table 5.1 Phase formation in the Ru (2000 Å)-Al(850 Å) thin film system heated at 550°C.

Time (minutes)	Al	$RuAl_6$	Ru_4Al_{13}	$RuAl_2$	Ru_2Al_3	RuAl	Ru
0	×	×					×
20				×	×		×
120				×	×		×
600				×	×		×

5.2.2. Lateral diffusion couples

Al-island geometry

<u>Optical microscope study</u>

Samples were prepared using electron beam vacuum deposition and then annealed in a standard vacuum furnace to induce phase formation. The lateral diffusion couples were made by depositing islands of aluminium (3800 Å thick) onto a thin film of ruthenium (300 Å), through a silicon mask with 780 × 390 μm rectangular holes. The lateral diffusion structure was deposited onto an oxidised Si substrate. The minimum distance between the islands being 1mm. **Fig. 5.5** shows optical micrographs of a virgin sample (a) and a sample that has been annealed at 550 °C for 29 hours (b). **Fig. 5.5(c)** is a schematic diagram of the island edge in the reacted sample viewed from the side. The optical micrographs show four important points.

1. The island edge does not move during reaction.
2. Dark patches appear all over the island surface.
3. The reaction region seems smooth and uniform.
4. It looks like there is only one phase present in the reaction region (B). Regions A and C are the Al island and the Ru thin film respectively.

Stellenbosch University https://scholar.sun.ac.za

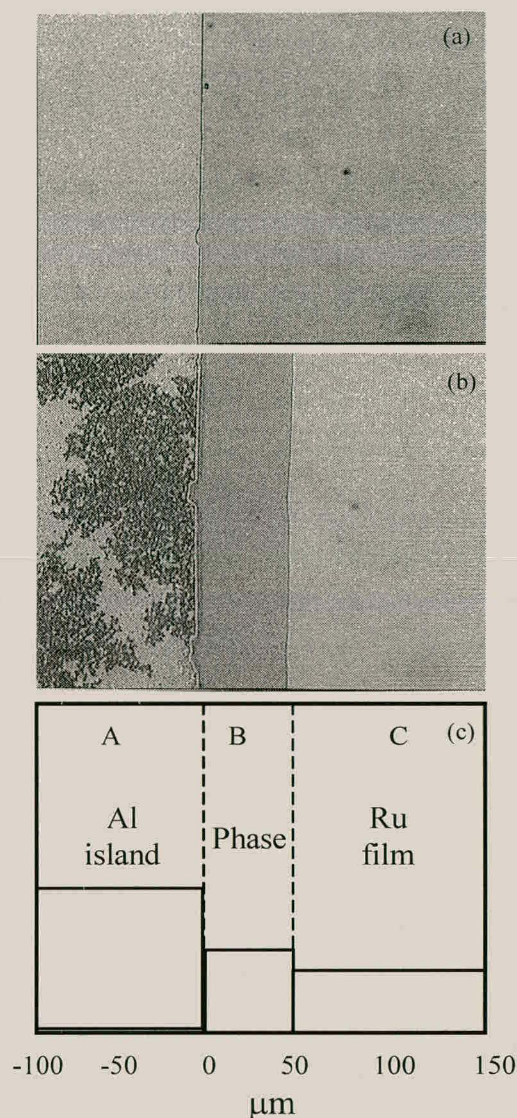

Fig. 5.5 Optical micrographs and schematic of the island edge in a virgin and annealed (550 °C 29 hours) sample. The virgin sample structure had 3800 Å thick Al islands deposited onto a 300 Å Ru thin film. A Ti glue layer (<20 Å) was used between the Ru thin film and the SiO_2 substrate to prevent peeling.

The dark patches are areas where the aluminium has been consumed non-uniformly leaving voids where the underlying Ru-aluminide thin film is visible. This can be seen in **Fig. 5.6** where the Al-island RBS spectrum shows Ru present on the surface. A further indication in this spectrum of the non-uniform Al island is the slanted front edge of the Ru signal. Voiding has been well documented in metal aluminide thin film systems [De-97, Co-90]. The voiding occurs because of very fast grain boundary and interface diffusion of the Al. The voids are spread over the full area of the island and not just at the edge, indicating that the entire island provides the Al that is consumed

Stellenbosch University https://scholar.sun.ac.za

by the lateral growing phase. The fact that the island edge stays in the same place also indicates that not just the Al near the edge takes part in the lateral phase formation. This is in contrast to lateral diffusion couples like Ni-Si [Zh-82] and Cr-Si where the island shrinks laterally as phase formation takes place. The fact that the phase formation occurs to the outside of the island also implies that Al is the diffusing species as there is no Al outside the island before annealing.

Nuclear microprobe study

The three regions visible in the optical micrographs of the island edge in the annealed sample are also visible in **Fig. 5.7** and **Fig. 5.8**. **Fig. 5.6** shows the RBS spectra from each of these three regions. A RUMP [Do-85] simulation of region A shows a $RuAl_6$ film covered by a very uneven film composed of Ru, Al and oxygen. The non-uniformity in the Al island can be seen by the sloping front edge of the Ru signal. RUMP simulation show region B to be a uniform (1500 Å) Ru_4Al_{13} film. Region C is the surrounding un-reacted Ru thin film (300 Å).

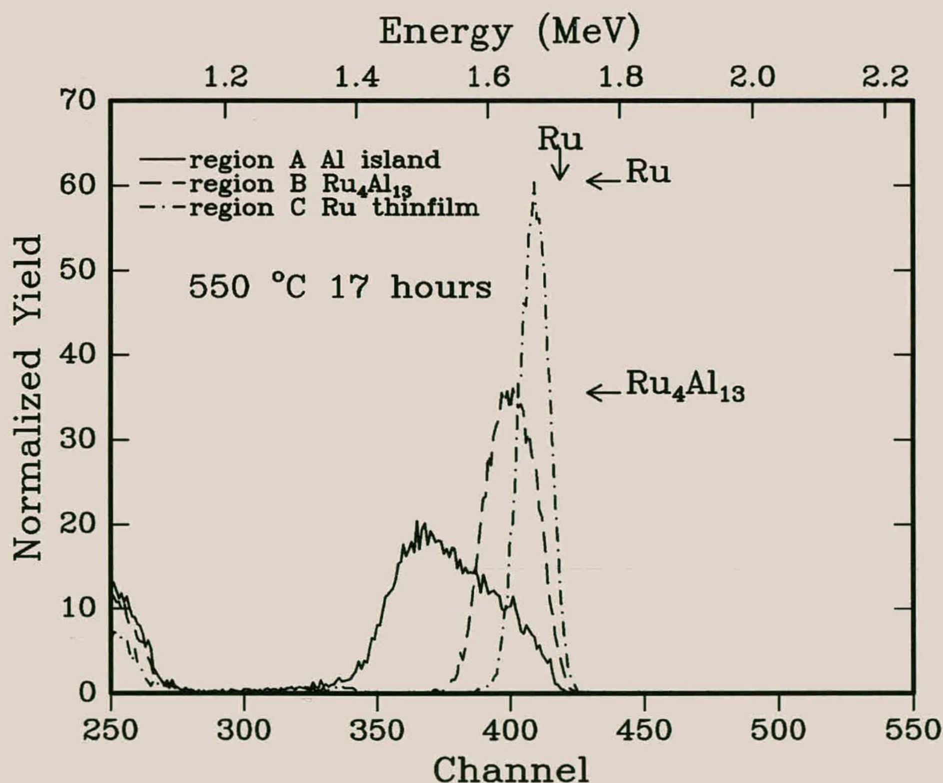

*Fig. 5.6 Overlay of RBS spectra showing the Ru signal, acquired using the nuclear microprobe in regions similar to A, B and C in **Fig. 5.5**. The horizontal arrows indicate the expected Ru signal heights for Ru and Ru_4Al_{13}. The vertical arrow indicates the Ru surface position.*

Stellenbosch University https://scholar.sun.ac.za

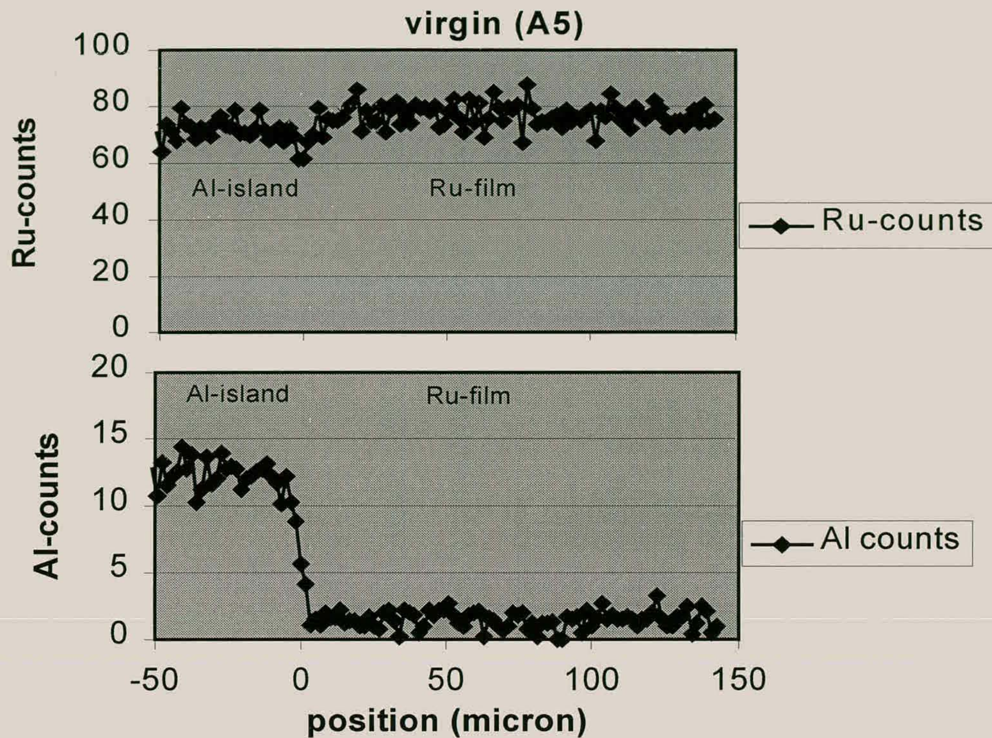

Fig. 5.7 Plot of Ru and Al RBS peak heights as a function of lateral position for a virgin sample. The origin of the horizontal scale is at the island edge.

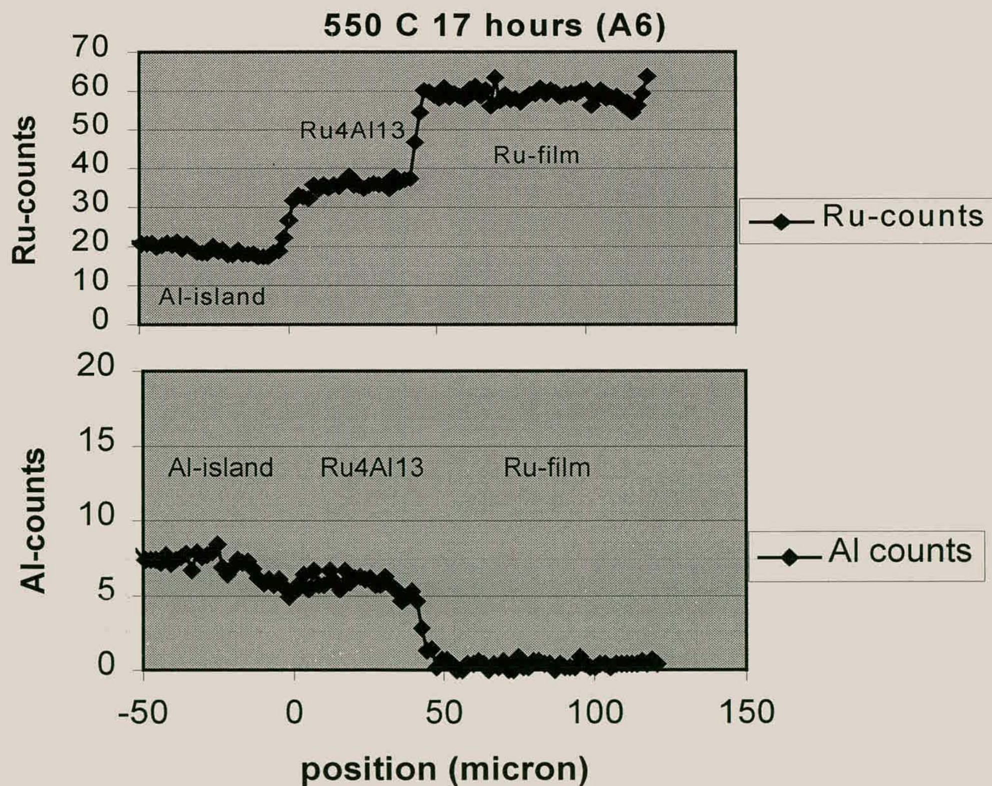

Fig. 5.8 Plot of Ru and Al RBS heights as a function of lateral beam position for an annealed sample (550 °C 17 hours). The origin of the horizontal scale is the position of the original island edge.

Stellenbosch University https://scholar.sun.ac.za

Fig. 5.7 and **Fig. 5.8** show plots of Ru and Al RBS signal heights as a function of lateral position measured with the NMP for virgin and annealed (550 °C 17 hours) samples. The original island edge corresponds to the origin of the x-axis. **Fig. 5.8** shows that the position of the island edge does not move after the sample is annealed and lateral diffusion takes place. It is therefore concluded that Al is the diffusing species and that Al diffuses to the surrounding reaction region from the entire island and not just from the island edge. The Al diffuses non-uniformaly from the entire island passing through the underlying phase and into the surrounding reaction region. This is confirmed by the voids visible over the full area of the island (see **Fig. 5.2** and **5.5**). After the composition of the different regions had been identified using RBS an optical microscope was used to measure the width of the lateral reaction region for different annealing times.

Fig. 5.9 shows how far the Ru_4Al_{13} phase has grown laterally in micrometers as a function of time at 550 °C. The phase grows with linear time dependence indicating reaction limited growth kinetics. The fact that the phase grows linearly indicates that it has not grown far enough for the long distance that the Al must diffuse to slow down the phase growth. If this were to happen the phase would start growing non-linearly or with diffusion limited kinetics, which would mean that the availability of Al would decrease at the reaction interface, as the phase grew thicker. When the so-called critical thickness is reached it would be energetically more viable for a more Ru-rich phase to nucleate and grow. In this case, due to the reaction limited growth kinetics of the Ru_4Al_{13} phase, the availability of Al does not decrease as the phase grows thicker and therefore the same phase continues to grow as it stays energetically the most viable.

Stellenbosch University https://scholar.sun.ac.za

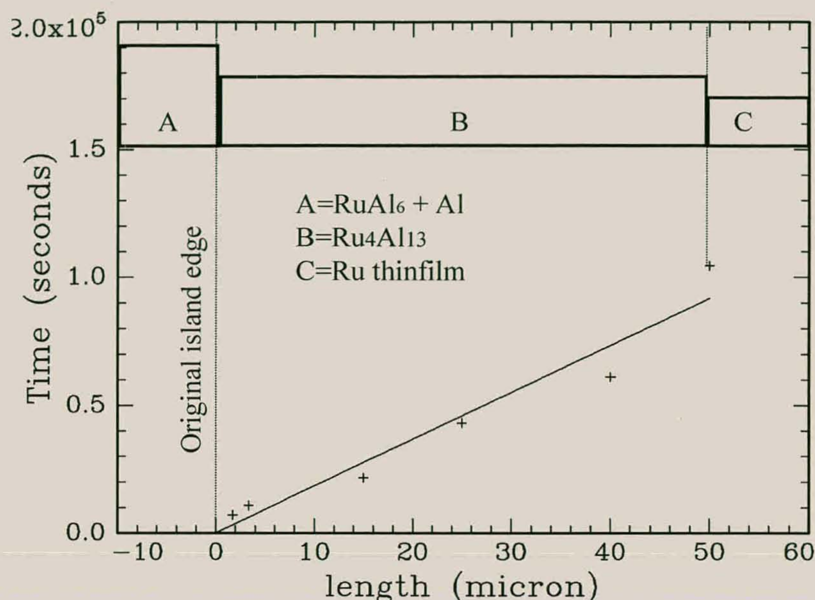

Fig. 5.9 Lateral thickness of the Ru_4Al_{13} as measured, using an optical microscope, for different times at 550 °C showing linear time dependence and therefore reaction limited growth.

Ru-island geometry

Samples were also made with 2000 Å thick Ru islands deposited onto a 300 Å Al thin-film on top of an oxidised Si wafer. Due to the good adhesion between Al and SiO_2 a Ti glue layer was not necessary. **Fig. 5.10** shows an optical micrograph of a Ru island after annealing at 500 °C for 19 hours. Regions (a) and (c) are the Ru island and the Al thin-film respectively. Region (b) was found to be a region of depleted Al surrounding the island. This can be seen from the EDS measurements in **table. 5.2** that were taken in the three different regions using a scanning electron microscope. The accelerator voltage necessary to excite the Ru L lines was 10 kV and therefore the sampling depth was always more than just the surface thin films and included the SiO_2 substrate. This is why for example the concentration of Al is not 100 in the thin film but much less. This means that the absolute values cannot be trusted but they can still be used to compare the three regions. Table 5.2 gives the relative concentrations measured in the three regions. The depletion zone therefore has a factor four times less Al than the Al thin-film and no Ru. The Al has therefore diffused out of this region and has not been replaced by Ru. As Al is the diffusing species the reaction interface is at the Ru-aluminide / Ru-island interface. The aluminide does not grow laterally but Al diffuses upward into the island consuming Ru as it goes. As each Al

Stellenbosch University https://scholar.sun.ac.za

atom moves into the island it leaves a void. The Al thin film therefore recedes leaving a depletion zone.

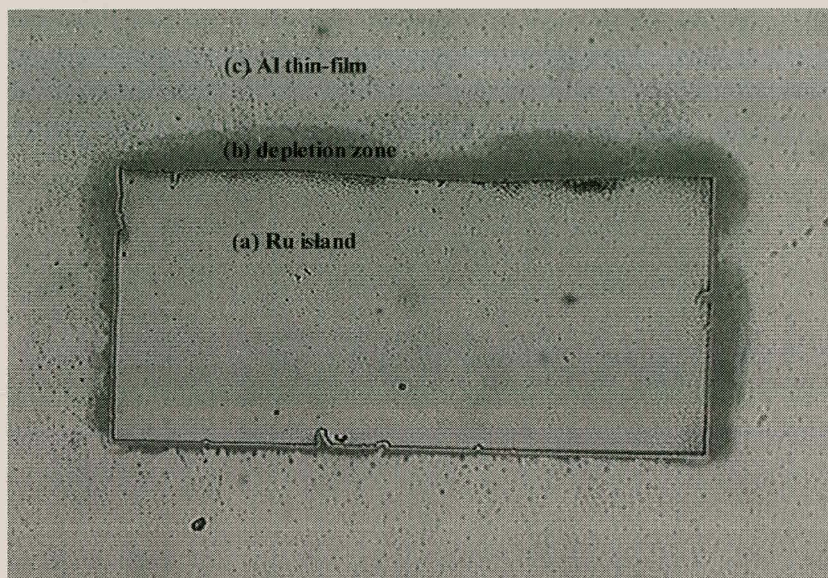

*Fig. 5.10 Optical micrograph of the a Ru island on a sample that has been annealed for 19 hours at 500 ^{0}C. In the virgin sample 2000 Å thick Ru islands were deposited onto a 300 Å Al thin film. The Al and Ru compositions at positions (a), (b) and (c) are shown in **table. 5.2**.*

*Table.5.2. SEM EDS results (10kV acceleration voltage) showing the depletion of the Al-thin film around the Ru-island. Regions (a), (b) and (c) are shown in **Fig. 5.10**.*

Region	Al(relative concentration)	Ru(relative concentration)
(a) Ru island	30	620
(b) depletion region	10	0
(c) Al thin-film	40	0

Stellenbosch University https://scholar.sun.ac.za

5.3. Pt-Al system

5.3.1. Thin film couples

The Pt-Al system has many different equilibrium phases. **Fig. 5.11** shows that the Pt_5Al_{21} phase has the largest effective heat of formation at the composition of the liquidus minimum, followed by Pt_8Al_{21}, $PtAl_2$ and Pt_2Al_3. Both Pt_8Al_{21} and Pt_5Al_{21} have large atom per unit cell ratios (116 and 416 respectively) which could cause nucleation difficulties. If nucleation were therefore taken into consideration the EHF model would predict either $PtAl_2$ or Pt_2Al_3 as first phase.

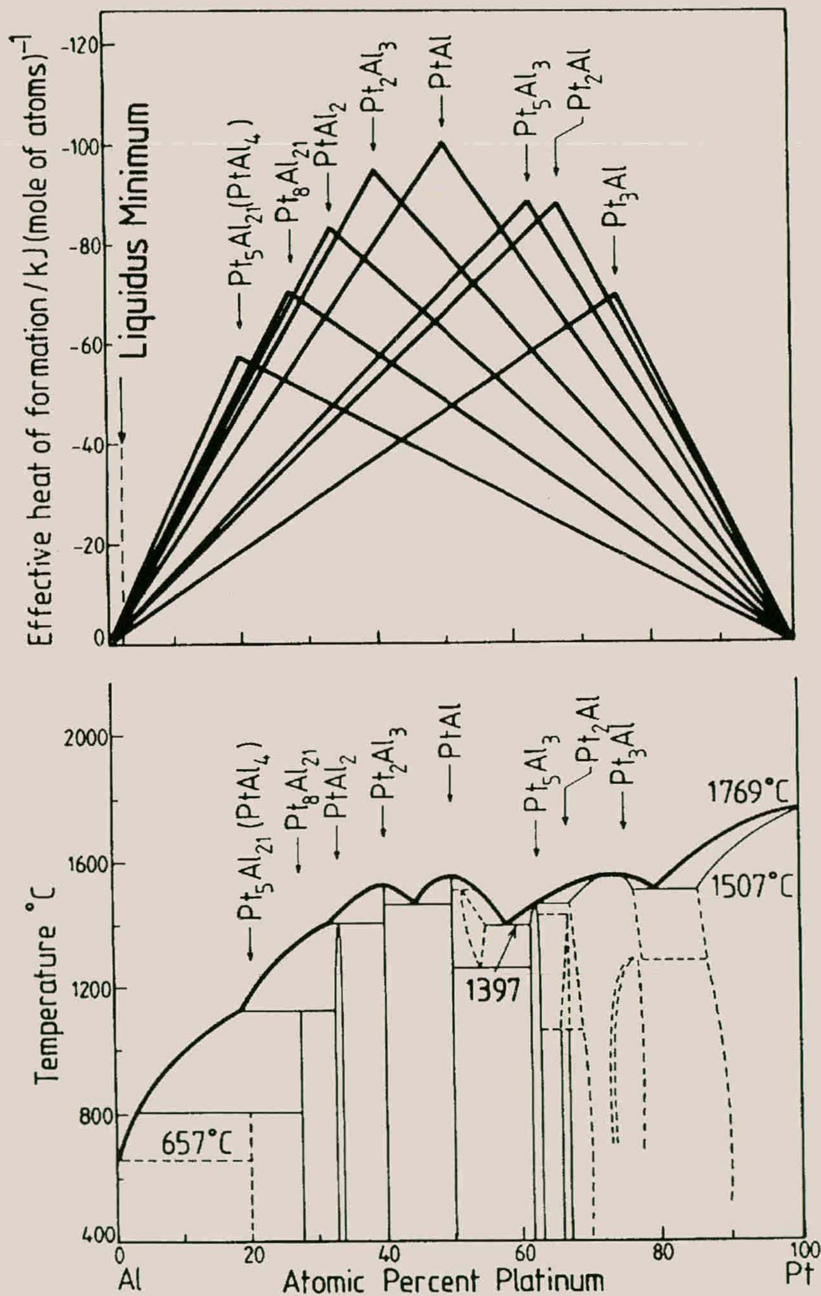

Fig. 5.11 EHF and phase diagram for the Pt-Al binary system.

Stellenbosch University https://scholar.sun.ac.za

Most thin film studies find Pt_2Al_3 as the first phase [Co-87, Co-92] (see **table 5.3**). The metastable $PtAl_4$ phase has also been reported as first phase [Co-87, Co-92]. As this phase is a metastable phase it is difficult to determine its heat of formation experimentally. Since, however $PtAl_4$ has a composition very close to that of Pt_5Al_{21} it can be expected according to Miedema [De-88] that $PtAl_4$ and Pt_5Al_{21} should have very close heats of formation and therefore very close effective heats of formation. If nucleation difficulties are therefore ignored the EHF model would predict the formation of either $PtAl_4$ or Pt_5Al_{21} as first phase.

Table 5.3 Phase formation in the Pt(1500 Å)-Al(3 mm) thin film system heated at different temperatures [Co-87, Co-90].

Temp (°C)	Al	$PtAl_4$	Pt_8Al_{21}	$PtAl_2$	Pt_2Al_3	PtAl	Pt_5Al_3	Pt_2Al	Pt_3Al	Pt
310	×				×					×
375	×				×					
450	×	×								
510	×	×								

5.3.2. Lateral diffusion couples

Al-island geometry

<u>Optical microscope study</u>

Samples were prepared using electron beam vacuum deposition and then annealed in a standard vacuum furnace to induce phase formation (see phase diagram in **Fig. 5.11**). The lateral diffusion couples were made by depositing islands of Al (2500 Å) onto thin films of Pt (400 Å) on top of oxidised Si wafers, through a silicon mask with 780 μm × 390 μm rectangular holes. The minimum distance between the islands being 1mm. **Fig. 5.12** shows optical micrographs of the island edge in a virgin sample (a) and a sample that has been annealed at 500 °C for 780 minutes (b). **Fig. 5.12** (c) is a schematic diagram of the island edge in (b) viewed from the side. Four important points should be noticed in the optical micrographs.

1. The island does not shrink laterally i.e. the island edge does not move.
2. The entire island surface becomes rough.
3. The reaction zone looks smooth and homogenous.

Stellenbosch University https://scholar.sun.ac.za

4. Two colour regions are visible in the reaction zone (B and C) with four regions in total A, B, C and D.

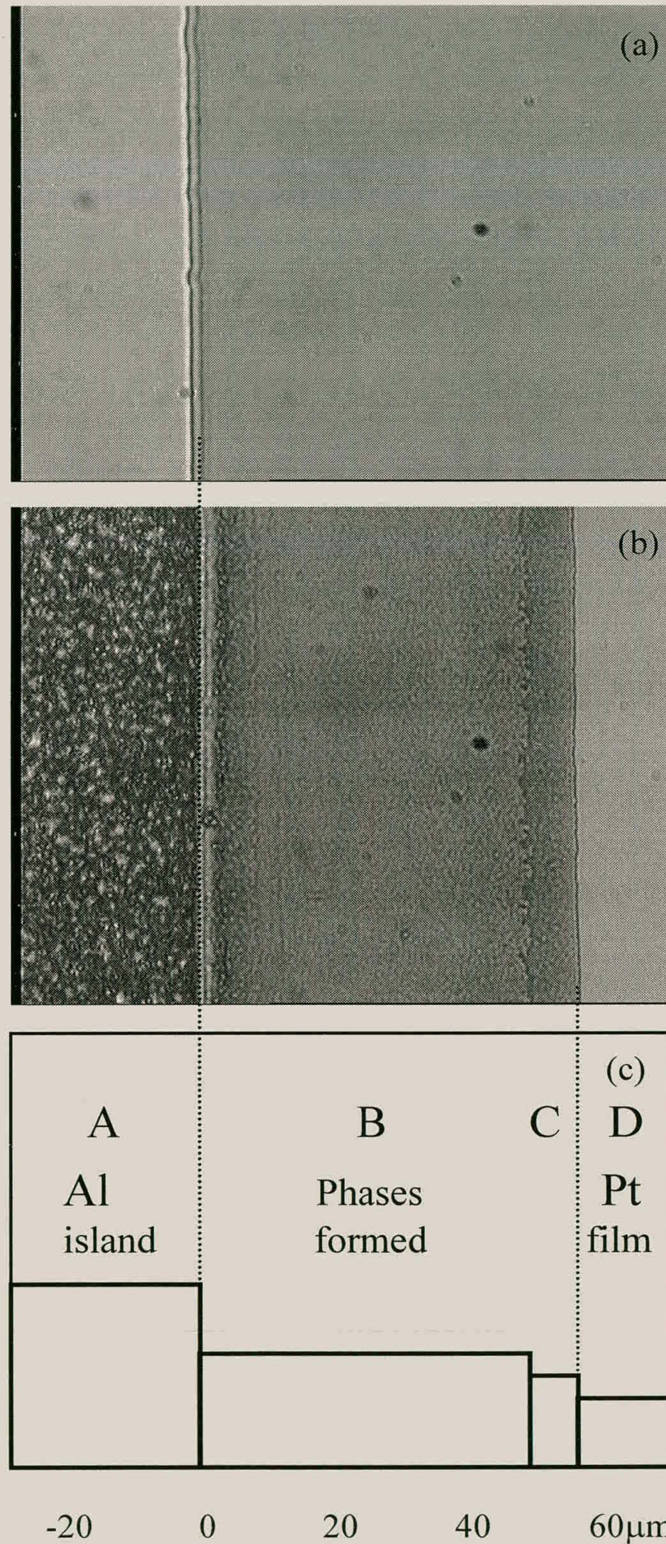

Fig. 5.12 Optical micrograph of the edge of an Al island (2500 Å) on a thin film (400 Å) of Pt (a) before heating and (b) after heating for 780 minutes at 500 °C showing lateral phase formation. (c) Schematic representation of the phase formation.

Stellenbosch University https://scholar.sun.ac.za

The fact that the position of the island edge stays in the same place indicates that the Al island is not being consumed from the edge as is the Ni island in the Ni-Si system [Zh-85]. The Al is therefore being supplied to the reaction zone from throughout the island. This would also explain the rough texture of the island surface, which is caused by voiding in the aluminium. This can be seen in **Fig. 5.13** where the RBS spectrum for the Al-island shows that the Pt signal front edge slopes forward almost to its surface position. This indicates a very non-uniform Al island. Void formation in aluminide thin film systems is well documented [Co-90]. The voiding usually occurs in the aluminium thin film due to very fast diffusion of the Al along grain boundaries and interfaces. The Al is selectively consumed in certain regions but the underlying aluminide thin film still grows uniformly.

Nuclear Microprobe study

The Nuclear Microprobe (NMP) was used to analyse composition as a function of position, by scanning a 2 MeV alpha beam over an area of the sample similar to that shown in **Fig. 5.12(b)** and carrying out Rutherford Backscattering Spectrometry (RBS). The beam size was 2 μm and the backscattering angle 176° (annular detector). **Fig. 5.13** shows an overlay of normalised RBS spectra from each of the 4 regions identified in **Fig. 5.12(b)**. A RUMP [Do-85] analysis of RBS measured in region A shows a very uneven film of Al covering 2400 Å of a film with composition Pt_5Al_{21}. The surface Al film varies in thickness from 300 Å to 2300 Å. This is not strange as aluminide thin film systems are well known for their uneven consumption of the Al thin film [Co-90, De-87]. RUMP analysis of spectra measured in regions B, C and D give a 1500 Å film of Pt_8Al_{21}, a 1300 Å film of $PtAl_2$ and 400 Å of Pt respectively. As shown in **Fig. 5.13** the Pt peak heights correspond with these phase compositions.

Fig. 5.14 and **5.15** show plots of the Pt and Al RBS signal heights as a function of lateral position measured with the NMP for a virgin and annealed (500 °C 780 minutes) sample. The original island edge was taken as the zero point position. In the reacted sample the zero point also stays at the edge of the Al-island because the island

Stellenbosch University https://scholar.sun.ac.za

edge does not recede as reaction takes place. It is therefore concluded that Al is the diffusing species during phase formation and that Al diffuses to the reaction region from the entire island and not just from the island edge. The Al diffuses non-uniformly from the bulk of the island passing through the underlying phase (composition Pt_5Al_{21}) and into the surrounding reaction region, which is confirmed by the rough surface of the entire island (**Fig. 5.12(b)**) and the non-uniformity shown by the RBS spectra of the Al film left on the island (see **Fig. 5.13**). After the composition of the different regions had been identified with RBS, optical microscopy was used to measure the width of the reaction regions for different annealing times (**Fig. 5.16**). The x-scale shows how far the Pt_8Al_{21} and $PtAl_2$ phases have grown laterally in micrometers as a function of time at a temperature of 500 °C. It is clear that both these phases grow with a parabolic time dependence, indicating diffusion limited growth kinetics.

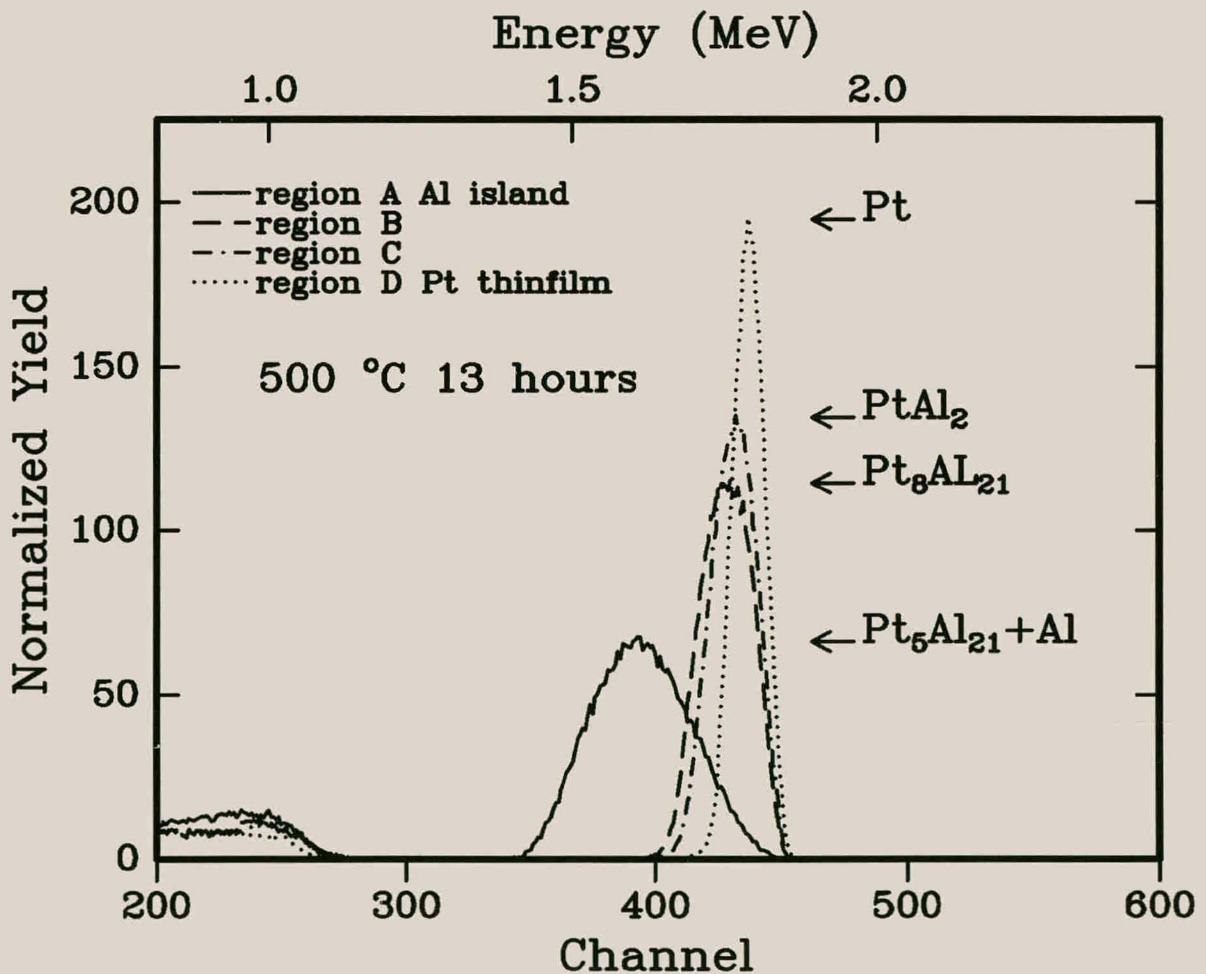

Fig. 5.13 RBS spectra of the three different regions labeled A, B, C and D in ***Fig. 5.16*** *acquired in the NMP. The horizontal arrows indicate the phases that Ru signal heights correspond to. The island consists of a Pt_5Al_{21} film covered by a non-uniform film of Al.*

Stellenbosch University https://scholar.sun.ac.za

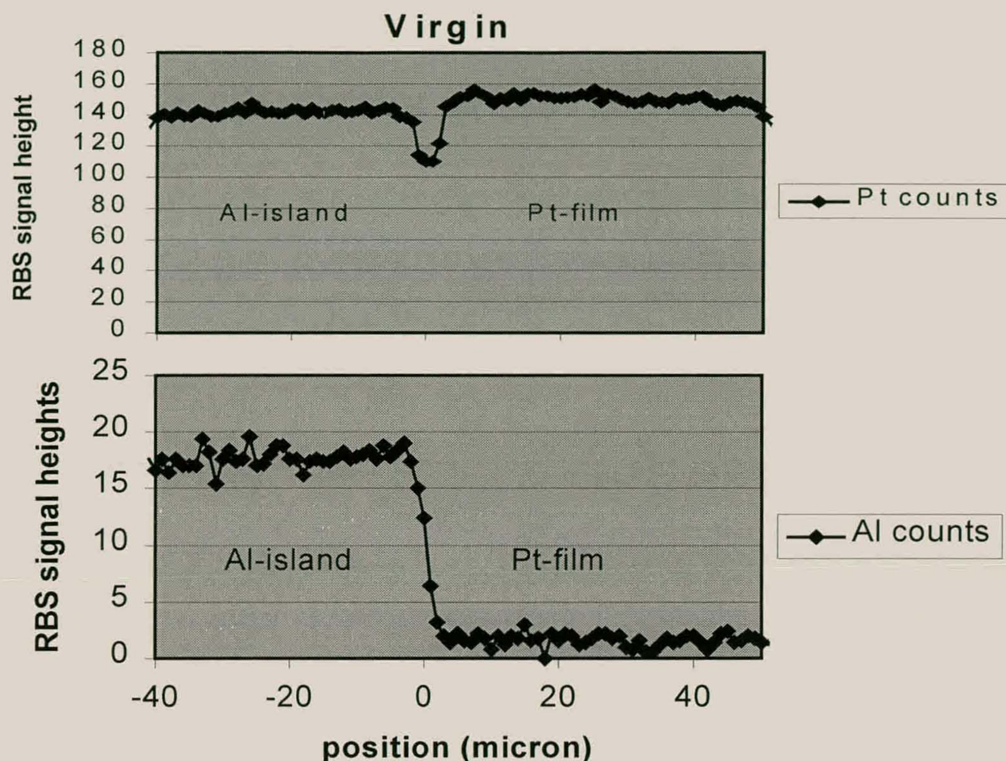

Fig. 5.14 Plot of Pt and Al RBS peak heights as a function of lateral beam position for a virgin sample. The origin of the horizontal scale is at the island edge.

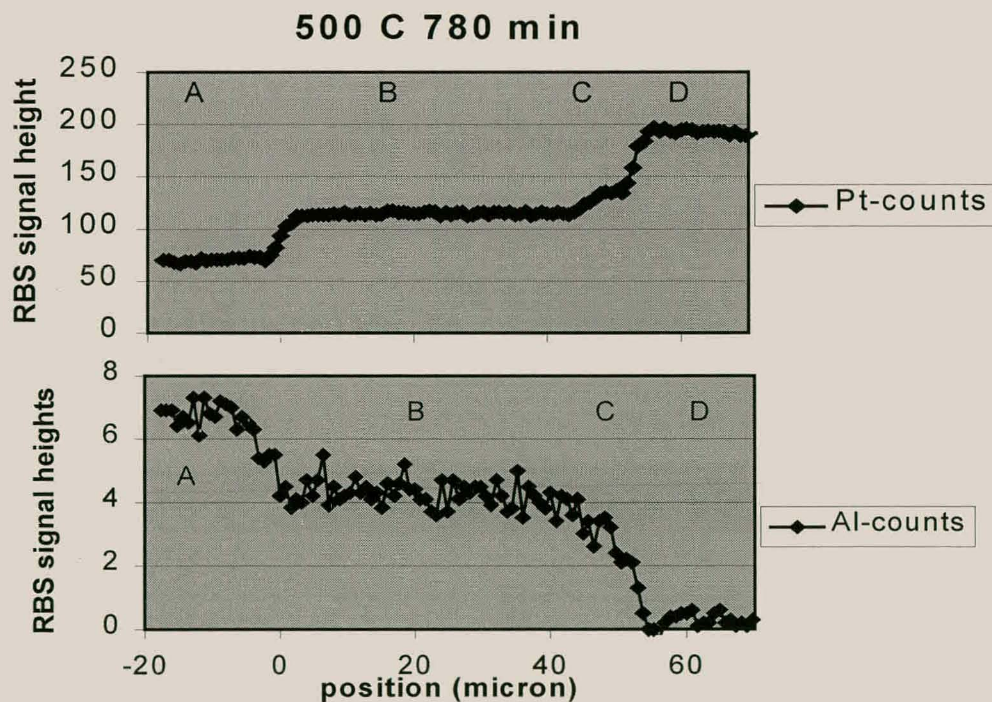

Fig. 5.15 Plot of Pt and Al RBS peak heights as a function of lateral beam position for a annealed sample. The origin of the horizontal scale is the position of the original island edge. Regions A, B, C and D are the same as in ***Fig. 5.12***.

Stellenbosch University https://scholar.sun.ac.za

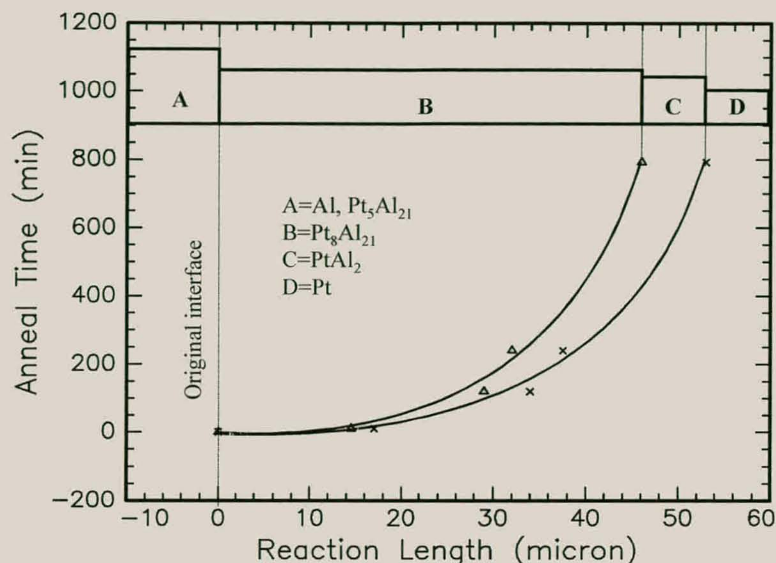

Fig. 5.16 Lateral thickness of Pt_8Al_{21} and $PtAl_2$ phases as measured using an optical microscope for different annealing times at 500 °C, showing a parabolic time dependence and therefore diffusion limited growth. The one curve shows how the phase (Pt_8Al_{21}) in region B grows relative to the original interface and the other curve, how the phase ($PtAl_2$) in region C grows relative to region B. The region between the two curves therefore corresponds only to the growth of $PtAl_2$.

Pt-island geometry

The Pt islands would not stay attached to the substrate after annealing. They pealed off together with the underlying Al-thin film. This could be because the Pt bonds well to the Al due to phase formation. As seen in the Cr-Si and Ru-Al system a crack or void forms around the island if the thin film is composed of the diffusing species. The stress in the thick Pt island (probably due to large differences in thermal expansion coefficients between the metals and the underlying SiO_2) then causes the island and underlying film to peal off.

Stellenbosch University https://scholar.sun.ac.za

5.4. Cr-Si system

5.4.1. Thin film couples

The Cr-Si binary system has four compound phases listed on the phase diagram (see **Fig. 5.17**). These are Cr_3Si, Cr_5Si_3, CrSi and $CrSi_2$. Of these only CrSi is a non-congruently melting phase. As usual in silicide systems the non-congruently melting phase does not form during thin film solid state interactions unless forced to do so stoichiometrically. The other phases all form with $CrSi_2$ always found as the first phase. The growth kinetics of $CrSi_2$ has been measured to be reaction limited with Si being the dominant diffusing species [Ei-83]. Subsequent phase formation is dependent on the relative amount of Cr and Si present in the sample. Excess Si would mean only $CrSi_2$ will form. If there is excess Cr then the other phases will form starting with Cr_5Si_3 and then Cr_3Si if there is enough excess Cr. If the atomic ratio of Cr to Si is 1:1 then CrSi will form as the final phase after Cr_5Si_3 (see Fig 5.18) [Pr-93].

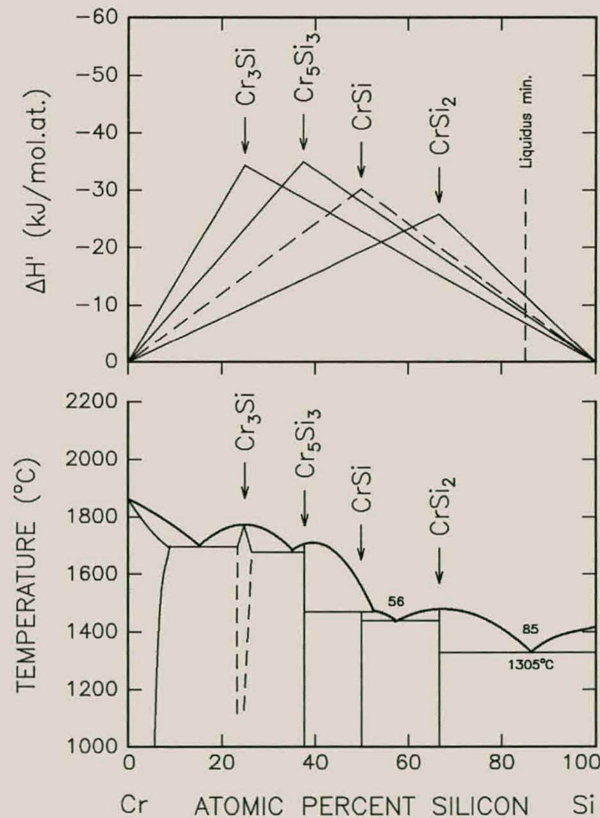

Fig. 5.17 EHF and phase diagram of the Cr-Si binary system. The EHF diagram gives the heats of formation of the different phases in KJ/mol.at as a function of composition.

Stellenbosch University https://scholar.sun.ac.za

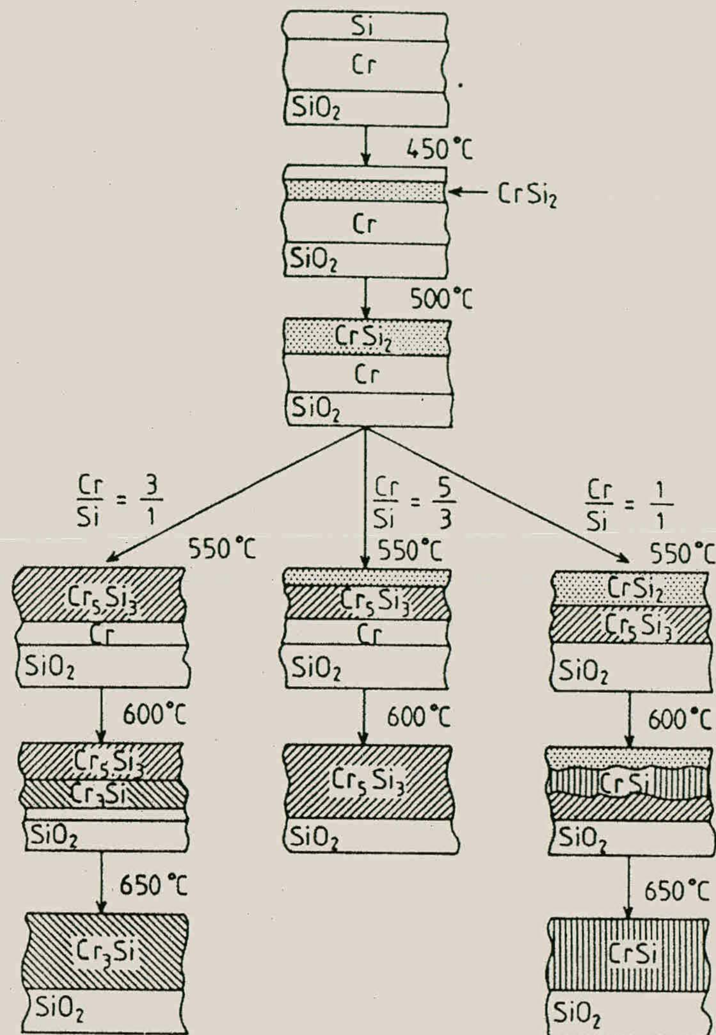

Fig. 5.18 Schematic diagrams of phase formation in the Cr-Si thin film system [Pr-93].

5.4.2. Lateral diffusion couples

Cr-island and Si-island lateral diffusion couples were deposited onto SiO_2 substrates. In both cases the planned island thickness versus thin film thickness was 2500 Å : 400 Å. RBS showed 10 at.% oxygen present in the Cr island and thin film after deposition. The samples were annealed at 600 °C for 3 hours in a vacuum furnace at 2×10^{-7} Torr.

Stellenbosch University https://scholar.sun.ac.za

Optical microscopy

Cr-island on Si-thin film

Fig. 5.19 shows the optical micrographs of the edge of the Cr island in a virgin and annealed sample. In both cases the Cr island is on the left. To the right of the edge the Si thin film onto which the island has been deposited is visible. **Fig. 5.19(a)** shows the micrograph of the virgin sample, while **Fig. 5.19(b)** shows the sample that has been annealed at 600 °C for 3 hours. As in the virgin sample the island edge is still well defined. None of the annealed samples in this sample group showed any lateral reaction under the optical microscope, even after annealing for 12 hours at 600 °C

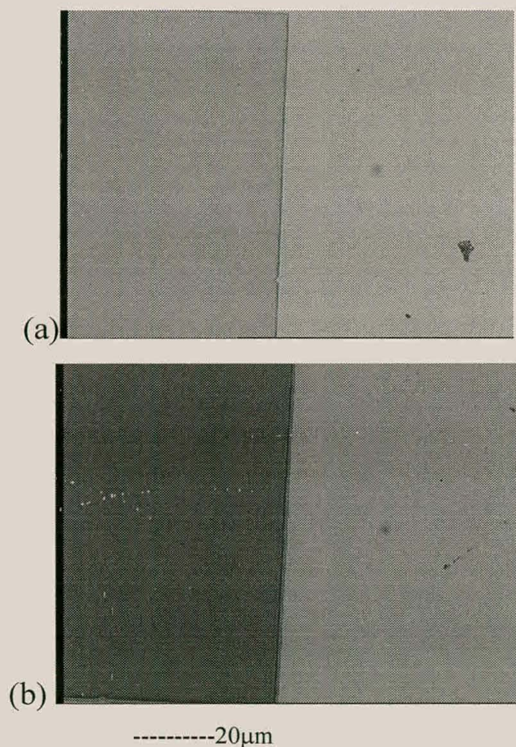

Fig. 5.19 Optical micrographs of the island edge (Cr island on Si thin film) in the virgin sample (a) and the 600 °C 3 hours annealed sample (b). In both cases the Cr island is on the left with the underlying Si thin film visible on the right. In the virgin sample the edge of the island is well defined and shows no lateral growth. As in the virgin sample no lateral reaction is visible at the edge of the island in the annealed sample.

Stellenbosch University https://scholar.sun.ac.za

Si islands on Cr thin film

Fig. 5.20 Shows optical micrographs of the edge of a Si island in a virgin and annealed sample. In both cases the Si island is on the left. To the right of the island edge the Cr thin film onto which the island has been deposited is visible. **Fig. 5.20** (a) shows the well-defined edge of the Si island in the virgin sample. **Fig. 5.20(b)** shows lateral reaction after annealing for 3 hours at 600 °C. The amount of reaction was not reproducible and in some cases there was no reaction, even after longer anneals. The Si island itself has shrunk and a reaction area with a width of about 30 μm has formed around the edge of the island. The reaction zone and surrounding Cr thin film are very rough. The rough surface complicates RBS analysis.

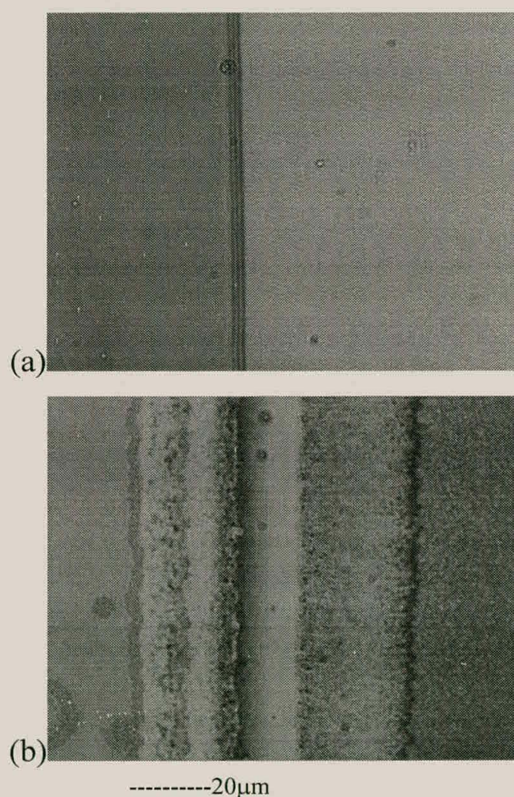

Fig. 5.20 Shows optical micrographs of the Si island edge in the virgin sample (a) and the 600 °C 3 hour annealed sample (b). In both cases the Si island is on the left. In the virgin sample the island edge is well defined and shows no lateral reaction. In the annealed sample a reaction zone has become visible at the island edge. The reaction zone and Cr thin film are rough compared to the smooth surface of the Si island on the left.

Stellenbosch University https://scholar.sun.ac.za

Nuclear microprobe study

The NMP was used to study the phase formation in both Cr-island and Si-island geometry. A 2 MeV apha beam (±2 μm) was scanned over a region on the edge of the island similar to the areas in the optical micrographs while the backscattered signal was aquired. RBS spectra could therefore be acquired from anywhere on the mapped area giving the composition as a function of position and depth.

Cr-island geometry (600 °C 3 hours)

In this geometry 3000 Å thick Cr islands were deposited onto a 400 Å Si thin film and annealed at 600 °C for 3 hours. **Fig. 5.21** shows that the Cr has not moved from the island. **Fig. 5.22** is a RBS spectrum acquired in a region on the island. A simulation of this spectrum shows that the Cr has reacted with all the underlying Si to form a film of Cr_5Si_3. The Cr that has not reacted to form the silicide has been oxidised to form a capping film of Cr_2O_3 which is the composition of the native Cr-oxide. The oxidation of the Cr has therefore prevented further phase formation and therefore the Cr rich Cr_3Si phase has not been formed. In **Fig. 5.21** the Si peak heights vary on and off the island region. This is not because the Si has moved but because of different Si compositions. The peak height in the island region corresponds to the Cr_5Si_3 phase and in the thin film region correspond to SiO_2. **Fig. 5.23** is a RBS spectrum from the thin film region off the island. The simulation shows that the Si thin film has been oxidised completely to form SiO_2. The dip and spike in **Fig. 5.21** shows that the Si in the region directly next to the island edge has diffused into the island leaving a crack or void in the Si thin film that runs around the island effectively cutting off any further Si supply.

Fig. 5.24 shows a diagram of the edge of the island. The oxidation of both the Si and the Cr has played a large role in limiting silicide formation. It does however seem that the void or crack that developed in the Si thin film at the edge of the island would have prevented any further Si moving laterally. The oxidation of the Si thin film

Stellenbosch University https://scholar.sun.ac.za

around the island would have prevented any lateral movement of the Cr out of the island.

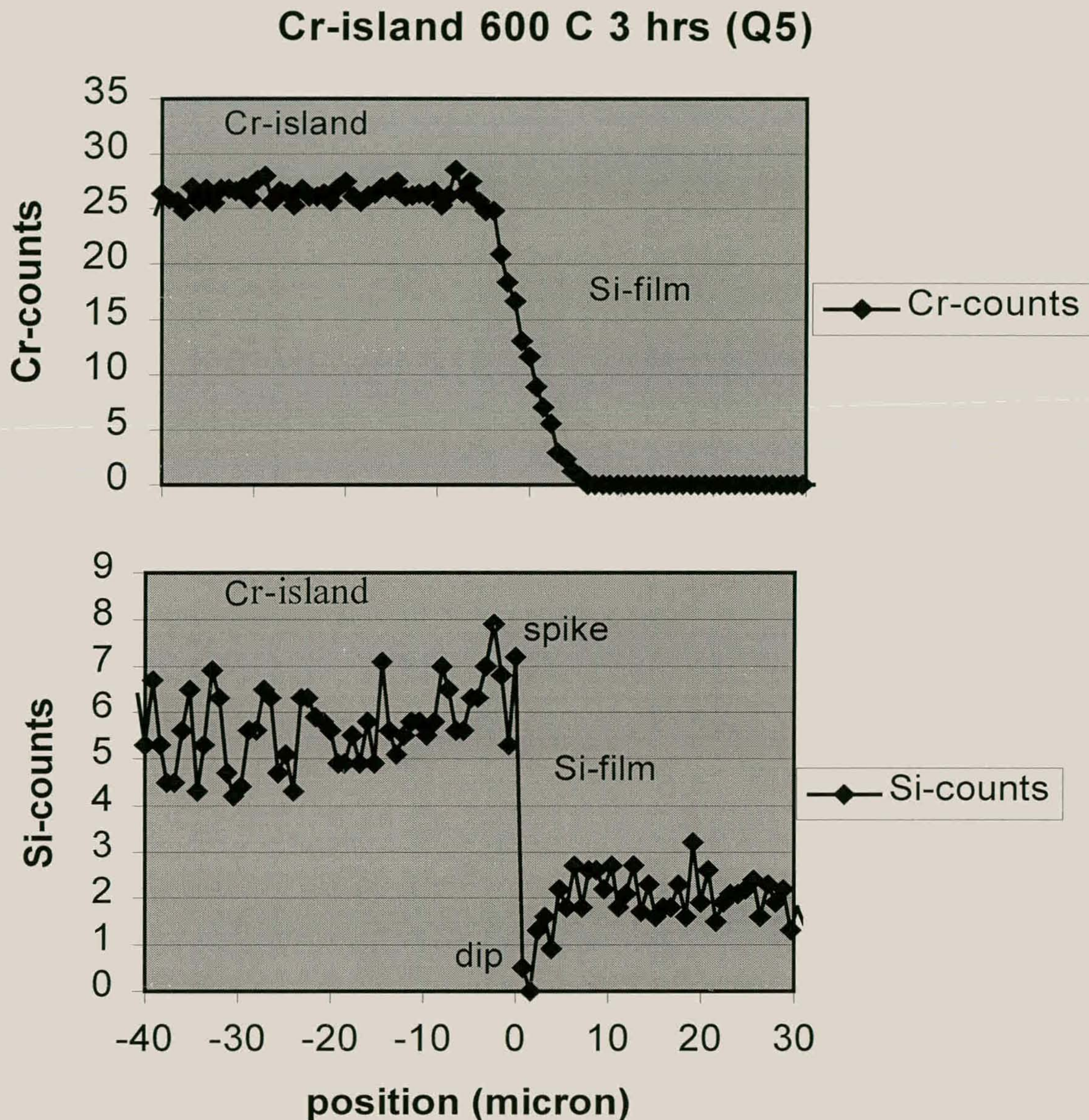

Fig. 5.21 Plot of RBS Cr and Si peak heights as a function of lateral position in an annealed sample. Simulations of RBS spectra from the Cr island show that the Cr height corresponds to a film of Cr_5Si_3 covered with Cr-oxide. The Si under the island has formed a silicide with composition Cr_5Si_3. From the spike and dip in Si counts at the island edge it can be concluded that some Si has moved into the island leaving a region of depleted Si just off the island edge. The rest of the Si thin film has reacted with oxygen to form SiO_2. The amount of silicon in SiO_2 is less than in Cr_5Si_3 and therefore the Si peak heights drop moving off the island.

Stellenbosch University https://scholar.sun.ac.za

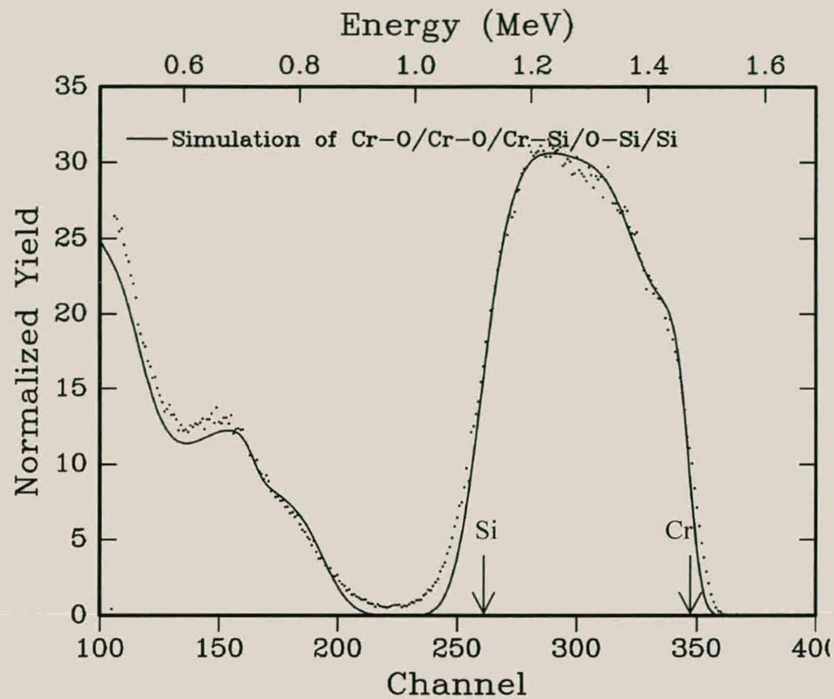

Fig. 5.22 RBS spectra generated from a 2D gate set on the Cr island. The sample has been annealed at 600 °C for 3 hours. The overlayed simulation has the following structure Si<>/8200 Å SiO_2/700 Å Cr_5Si_3/2500 Å Cr_6O_3/1800 Å Cr_2O_3. The arrows indicate the Si and Cr surface positions.

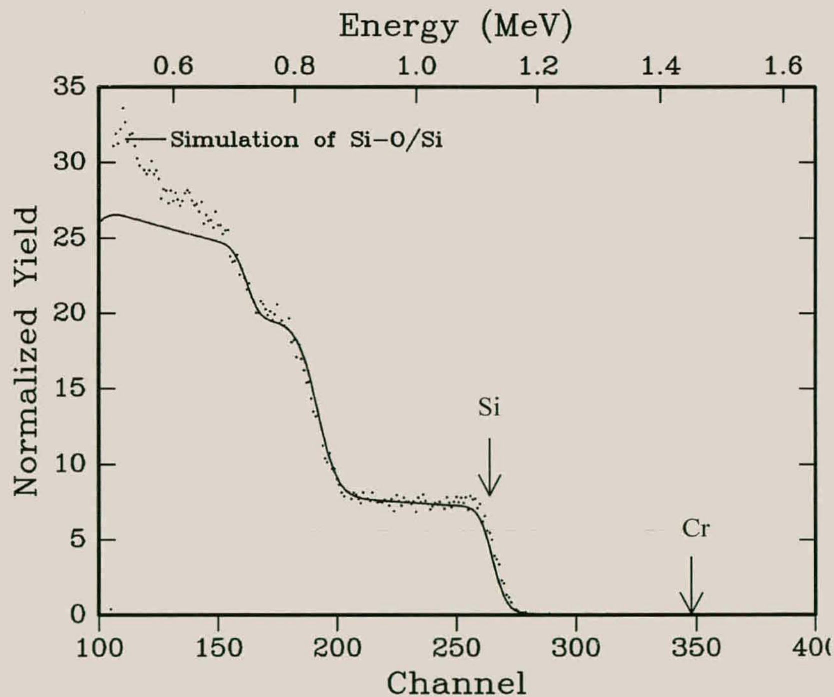

Fig.5.23 RBS spectra generated from a 2D gate set on the Si thinfilm with no Cr island ontop of it. Simulation overlay shows 8700Å of SiO_2 with no pure Si left. The virgin blanket samples had only 8200 Å of SiO_2. All the Si has been oxidised. The sample has been annealed at 600 °C for 3 hours. The arrows indicate the Si and Cr surface positions.

Stellenbosch University https://scholar.sun.ac.za

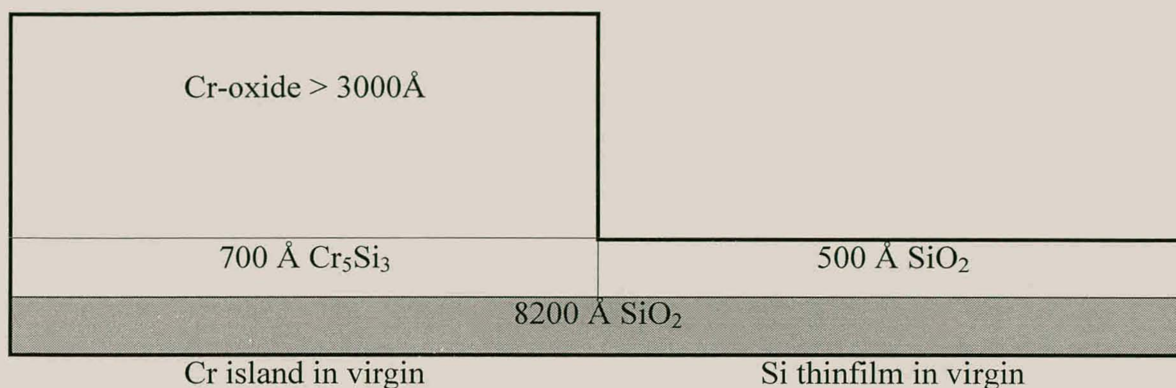

*Fig. 5.24 Diagram of the edge of a Cr island viewed from the side after annealing for 3 hours at 600 °C. The diagram has been constructed from the RBS spectra in **Fig. 5.22** and **5.23**.*

Si-island geometry (600 °C 3 hours)

In this geometry 2300 Å thick Si islands were deposited onto a 500 Å Cr thin film and then annealed at 600 °C for 3 hours. **Fig. 5.25** shows NMP RBS Cr and Si signal heights as a function of lateral position. The mapped area was at the edge of an island similar to the area in **Fig. 5.20(b).** The Cr signal height stayed relatively constant over the mapped area. The Si signal heights showed three regions of constant composition. They are on the island, in the lateral diffusion region and off the island in the thin film. **Fig. 5.26, 5.27** and **5.28** show RBS spectra and RUMP simulations from these three regions. From these simulations it can be seen that under the island the Si has reacted with the underlying Cr to form the most Si rich $CrSi_2$ phase. There is still excess Si left on the surface. In the reaction region the Si has also reacted with the underlying Cr to form $CrSi_2$ but there is less Si left on the surface in this region. The remaining Si contains 50 at.% oxygen in this region. The region off the island contains Si that must have come from the island edge where the Si film has become thinner. RBS shows that the composition in this region is non-uniform and contains oxygen. This could be the Cr and or the Si being oxidised. **Fig. 5.29** shows a schematic diagram of the island edge and lateral diffusion zone.

Stellenbosch University https://scholar.sun.ac.za

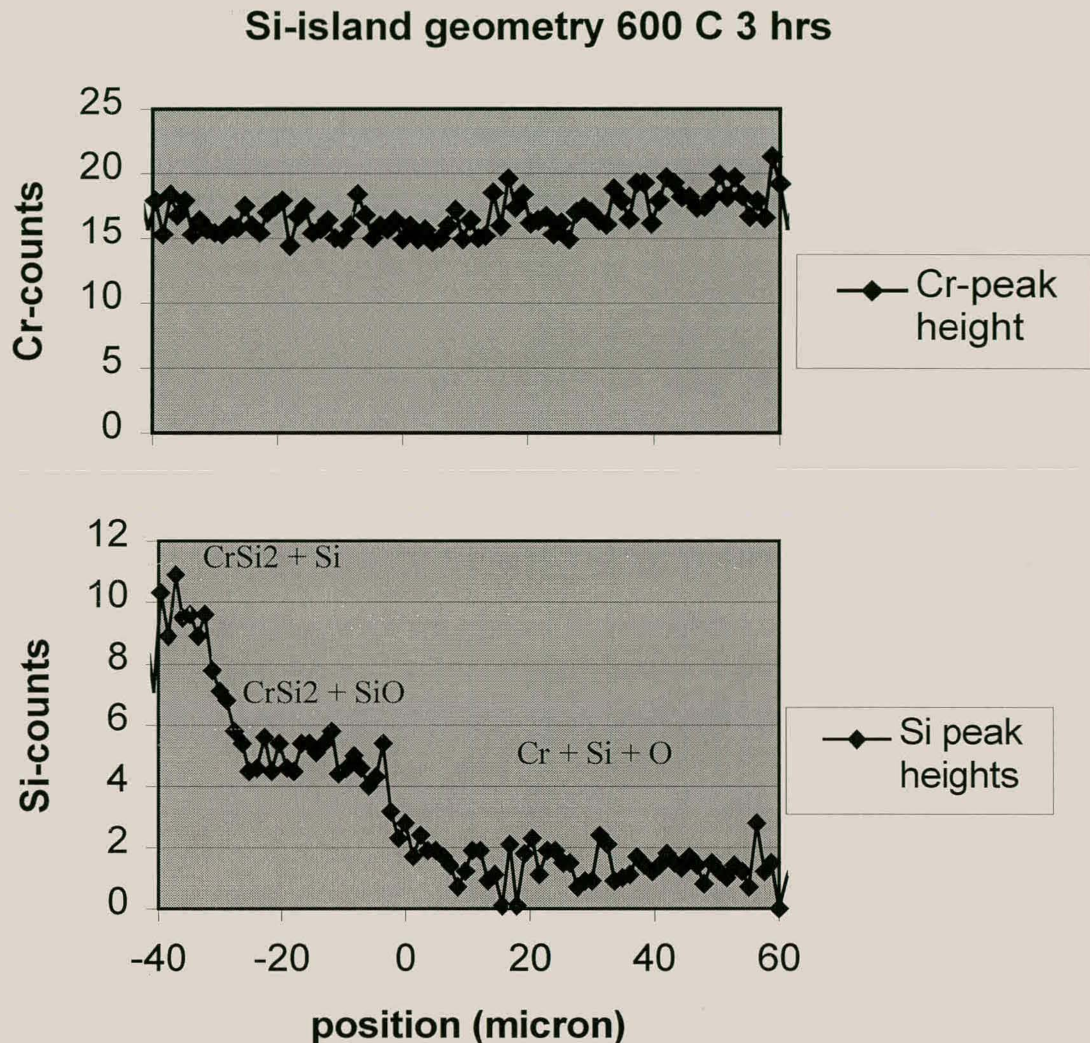

Fig. 5.25 Plot of RBS Cr and Si peak heights as a function of lateral position at the edge of a reacted Si island. The Cr peak height stays constant throughout the mapped area. From the Si peak heights three homogeneous regions can be identified.

Fig. 5.29 has been generated from simulations done on RBS spectra taken in the three constant composition regions using the NMP. The Si has reacted with all the underlying Cr to form the most silicon rich $CrSi_2$ phase. The Si island becomes thinner nearer the island edge as some of it diffuses into the surrounding thin film. The surrounding Cr has reacted with silicon and oxygen. Simulations of RBS spectra taken from the off island region shows a non-uniform mixture of Cr, Si and O.

Stellenbosch University https://scholar.sun.ac.za

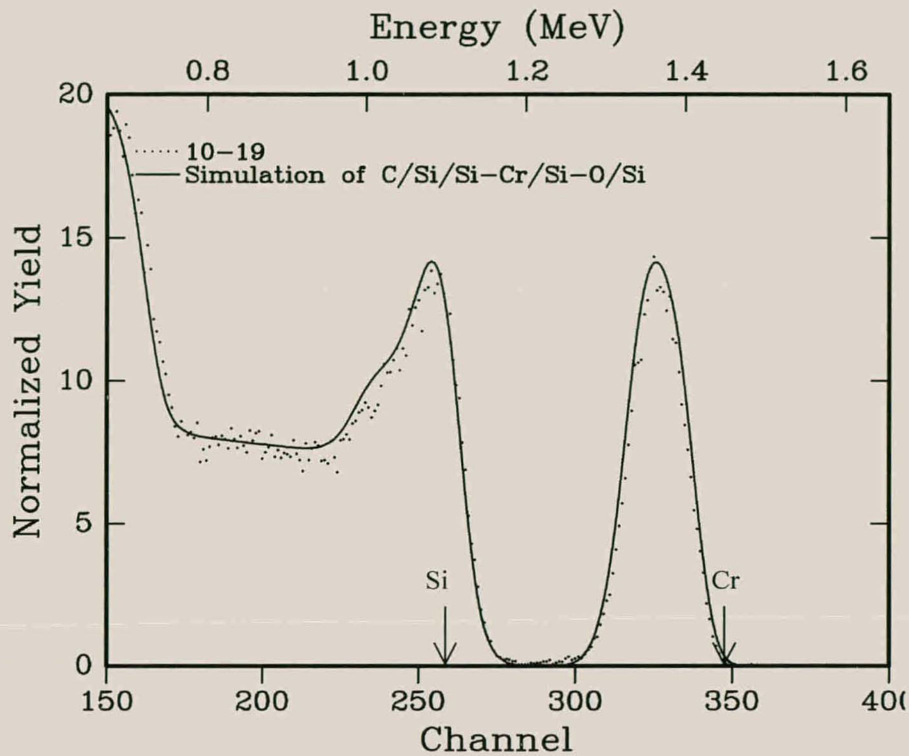

Fig. 5.26 RBS spectrum and overlaid RUMP simulation from a region on the Si island in a sample that has been annealed for 3 hours at 600 °C. The simulation was: SiO_2/1200 Å $CrSi_2$/1100 Å Si. The arrows indicate the Si and Cr surface positions.

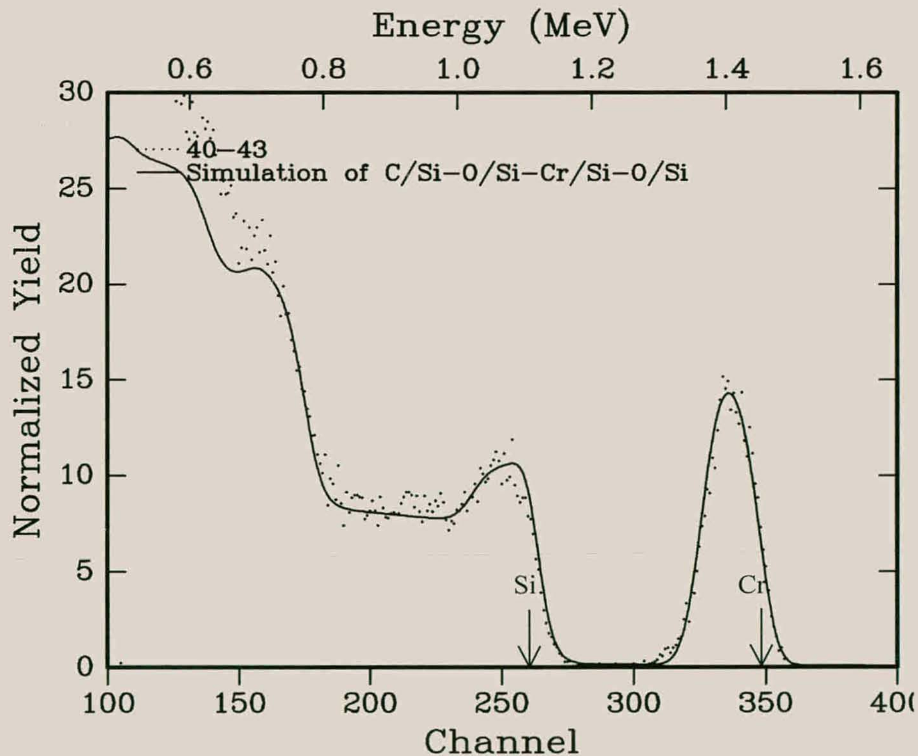

Fig. 5.27 RBS spectrum and overlaid simulation of the region on the edge of the island. The simulation was: SiO_2/1200 Å $CrSi_2$/400 Å Si_1O_1. The arrows indicate the Si and Cr surface positions.

Stellenbosch University https://scholar.sun.ac.za

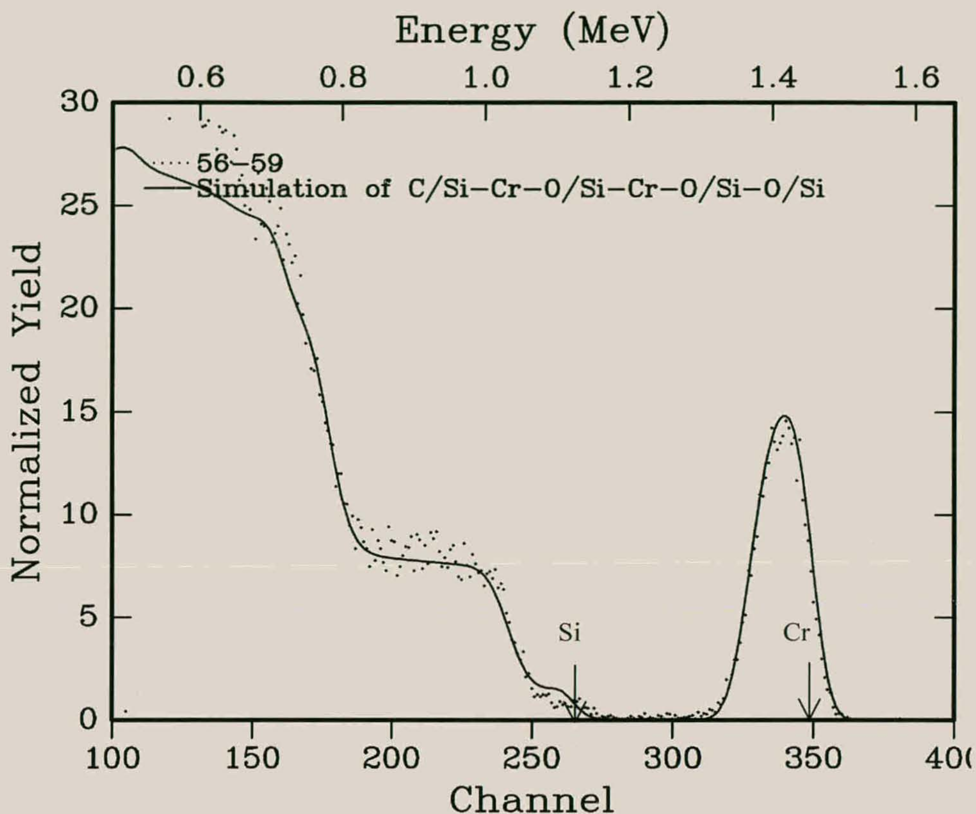

Fig. 5.28 RBS spectrum with the overlaid simulation from the thin film region off the island. The simulation was: SiO_2/1600 Å (Cr_2O_3+0.5SiO_2)/300 Å $Si_1Cr_{1.2}O_5$. The arrows indicate the Si and Cr surface positions.

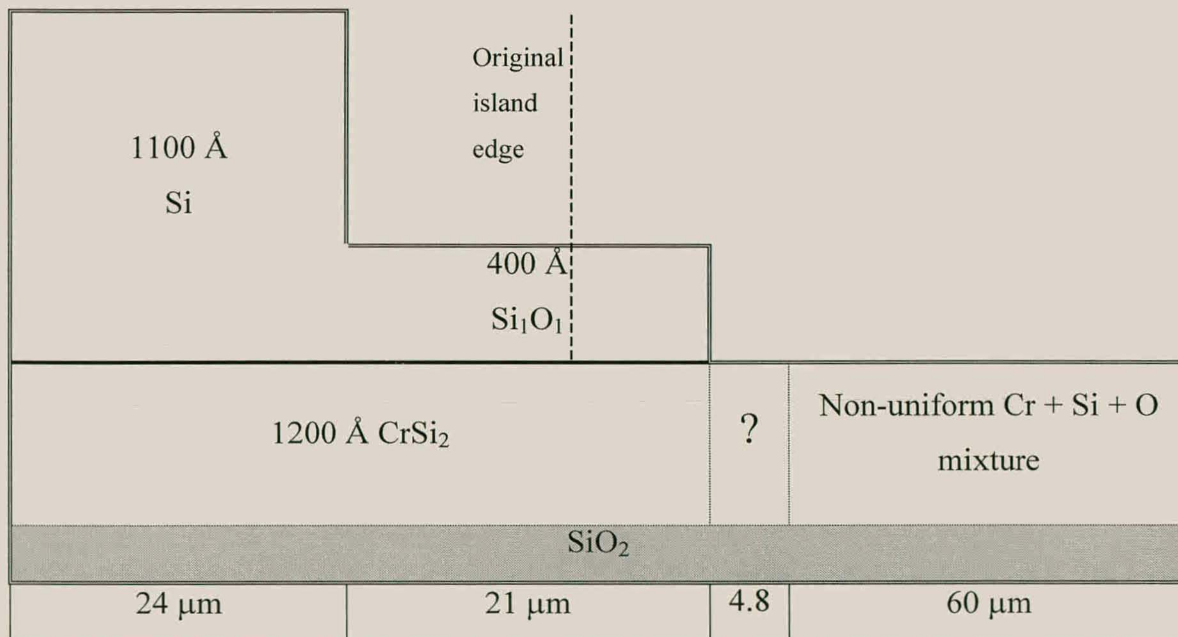

Fig. 5.29 Schematic showing structure of the edge of the Si island. Constructed from the RUMP simulations in ***Fig. 5.26*** *to* ***5.28****. The region marked "?" was too small to analyze accurately.*

Stellenbosch University https://scholar.sun.ac.za

The effect of different capping layers on lateral formation.

SiO_2 and Hf capping layers were used in an attempt to eliminate the effect of oxidation. The caps were deposited as blanket thin films onto Si-island geometry lateral diffusion couples. The samples were then annealed for 12 hours at 600°C. **Fig. 5.30** shows that there was very little or no lateral reaction in the samples with no cap and the SiO_2 cap. As mentioned before the uncapped samples did not always show lateral reaction even after long anneals. The samples with the Hf cap consistently showed lateral reaction. Hf has a high affinity for oxygen and getters the oxygen from the underlying Cr-thin film. RBS however showed extensive reaction between the Hf and the underlying Cr and Si. Ti caps have been known to improve silicide formation in Co-Si systems [Tu-95]. In this study we also showed that Ti-oxide caps led to faster $TiSi_2$ formation (see section 4.3.4).

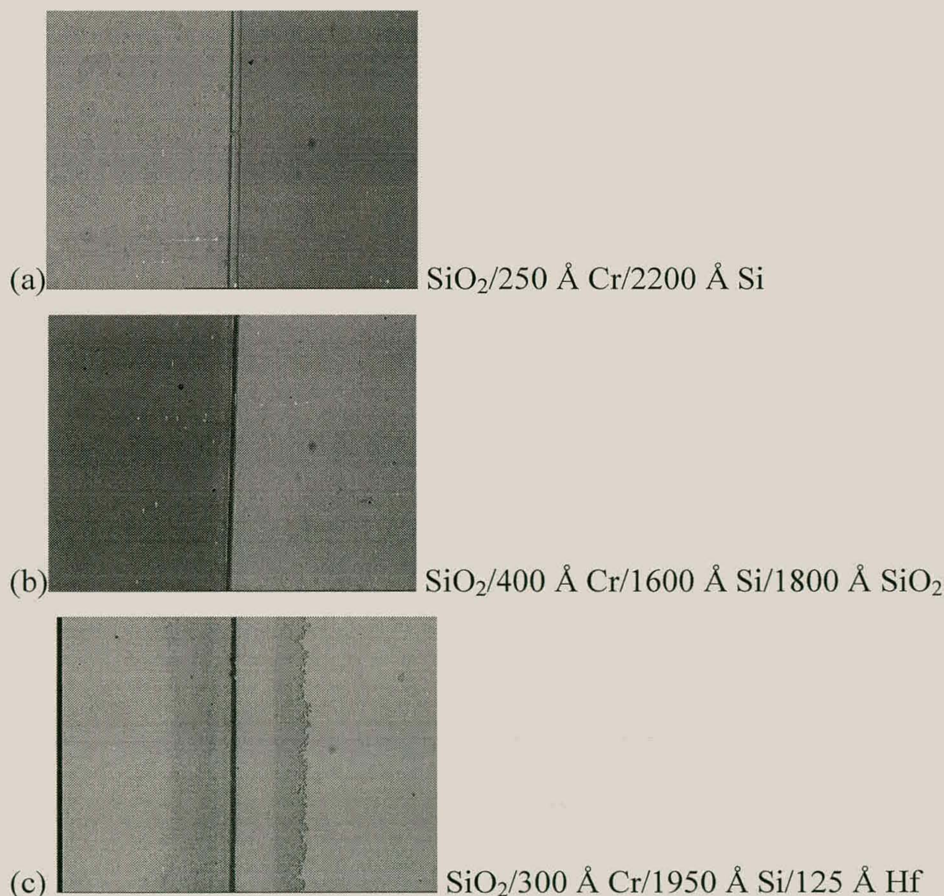

Fig. 5.30 Optical micrographs showing the improved lateral growth using a Hf-cap to prevent oxidation and getter oxygen from the underlying films. All the samples were annealed for 12 hours at 600 °C.

Stellenbosch University https://scholar.sun.ac.za

5.5. Summary and conclusion

In the thin film Ru-Al system it was found that if there is excess Al then $RuAl_2$ and Ru_4Al_{13} will form whereas if Ru is in excess then $RuAl_2$ and Ru_2Al_3 will form. In lateral diffusion couples two geometries, Al-island and Ru-island, were studied. In the Ru-island geometry where Ru is in excess there was no lateral diffusion but it was found that the Al was consumed around the island leaving a void or crack. In the Al-island geometry where Al is in excess, $RuAl_6$ formed under the island and Ru_4Al_{13} grew laterally (see **Table 5.4**). Voids were present over the entire island surface showing that the Al is consumed non-uniformly. The island edge did not move as is the case in the Cr-Si system. The laterally grown phase was uniform in thickness and composition and grew linearly (see **Fig. 5.9**) indicating reaction limited kinetics. The fact that the phase grows with reaction limited kinetics explains why only one phase namely Ru_4Al_{13} grows laterally. If the phase had grown with diffusion limited kinetics the effective Al concentration at the reaction interface would decrease as the phase grows and the diffusion length increases. After a critical thickness is reached the EHF model predicts that it will become energetically viable for a more Ru-rich phase (probably $RuAl_2$) to start growing.

As in the Ru-Al system both Pt-island and Al-island geometry's were studied. In the Pt-island geometry the islands pealed off after annealing. This was probably due to the same crack formation seen in the Ru-Al thin film around the Ru-island. The difference in thermal expansion coefficient between the metal films and the SiO_2 substrate caused stress in the island structure and the crack weakened the adhesion allowing the island and underlying film too peal off. In the Al-island geometry three phases grew simultaneously namely, Pt_5Al_{21}, Pt_8Al_{21} and $PtAl_2$ (see **Table 5.4**). Of these only $PtAl_2$ is found in thin film systems. The Pt_5Al_{21} phase is not reported in thin film studies but the metastable $PtAl_4$ phase is, which has very much the same composition [Co-90]. These three phases have more negative EHF values than Pt_2Al_3 that usually forms first in thin film couples (see **Fig. 5.11**). They also have very similar EHF values, which could explain why they grew simultaneously from the start. Both lateral phases were already present after 18 μm of lateral reaction. The relatively poor lateral resolution of the NMP could also mean that if Pt_2Al_3 did not grow to more than two micron it would not be detected. The island edge again did not

Stellenbosch University https://scholar.sun.ac.za

move while the entire island became rough indicating non-uniform Al consumption. Both lateral phases grew uniformly and non-linearly (see **Fig. 5.16**) indicating diffusion limited kinetics.

Table 5.4 Summary of lateral diffusion studies

System	Island	Lateral phase formation	Diffusing species	Diffusion mechanism	Island edge recedes	References
Ni-Si	Ni Si	NiSi, Ni_3Si_2, Ni_2Si, Ni_5Si_2, Ni_3Si Ni_2Si	Ni Ni	Vacancies and defects	yes yes	[Zh-83] [Zh-82]
Cr-Si	Cr Si	Voiding around island $CrSi_2$	Si Si	Vacancies and defects	yes	This work
Pt-Si	Pt Si	Pt_2Si Not reported	Pt -		yes	[Zhe-83]
Pd-Si	Pd Si	Pd_2Si Not reported	Pd + Si -			[Ch-84]
Pt-Al	Pt Al	Islands peeled off $PtAl_2$, Pt_8Al_{21}, Pt_5Al_{21}	- Al	Grain boundaries and interfaces	No (island forms voids)	This work This work
Ru-Al	Ru Al	Voiding around the island $RuAl_6$ and Ru_4Al_{13}	Al Al	Grain boundaries and interfaces	No (island forms voids)	This work This work
Pd-Al	Pd Al	Islands peeled off Pd_2Al_3 and $PdAl_3$	- Al	Grain boundaries and interfaces	Not reported	[Bl-92] [Bl-99]
Ni-Al	Ni Al	Not reported $NiAl_3$ and Ni_2Al_3	- Al<500°C Ni>500°C		no	[Li-88, Liu-88]
Pt-Ge	Pt Ge	No reaction $PtGe_2$, Pt_2Ge_3, $PtGe_2$	- Ge			[Ne-97] [Ne-97]
Ir-Ge	Ir	$IrGe_4$, Ir_3Ge_7, IrGe	?		yes	[Ha-99]

Oxidation was a big problem in the study of the Cr-Si system. Both Cr and Si oxidized in the vacuum furnace at 600°C. This is not strange for Cr but crystalline Si does not usually oxidize at 600°C and 10^{-7} Torr. The silicon thin film and islands in the lateral diffusion couples were deposited at room temperature in an e-beam system. Such films are amorphous and porous and are known to react much faster with oxygen due to the lower binding energy than crystalline Si and the large reactive surface area due to the porosity [Ad-89]. It is also possible that small undetectable

Stellenbosch University https://scholar.sun.ac.za

amounts of Cr diffused into the Si breaking the Si-Si bonds and making it energetically more viable for these Si atoms to react with oxygen. It has been found that Si dissolved in metals like Au and Ag is more reactive with oxygen than Si bound in a crystalline substrate [Ju-99]. This has also been found in previous studies where amorphous Si reacted faster and at lower temperature through gold to form SiO_2 than crystalline Si [Ju-99]. The Cr-island geometry samples showed no lateral reaction. There was a region of depleted Si forming a crack or void around the island. In the Si-island geometry $CrSi_2$ grew laterally. This is also the first phase in thin film diffusion couples. No kinetics could be measured due to the excessive oxidation in the system. The extent of reaction was not reproducible. In most annealed samples there was no lateral reaction. Unlike the aluminide systems the island area shrunk, meaning Si is sourced more from the edge and not from the entire island. Different caps were used to study their ability to limit oxidation. Hf was the most effective. This is probably because it has a higher affinity for oxygen than Cr and was able to act as a gettering site. Caps have previously been shown to improve silicide formation in the Co-Si [Tu-95] and Ti-Si (see section 4.3.2) systems.

The following are three areas where the study of lateral diffusion couples can improve the understanding of solid state interactions (see **table 5.4** for a summary of lateral diffusion studies).

1. Lateral diffusion couples can be used to study the transition between thin film and bulk diffusion. A good example of this is where the critical thickness of phases has been measured (eg. Ni_2Si and Al_3Pd_2 [Bl-92]). This is the thickness that a phase grows before another phase is thermodynamically favored at the reaction interface allowing both phases to grow simultaneously. Ni_2Si seems to have a critical thickness of about 30 μm at 600°C.
2. Information can be obtained about the diffusing species. If as in the Ru-Al and Pt-Al systems only one island geometry grows laterally it shows that the island species is the majority diffusing species in the formed phases. If a phase were to form where the thin film species is the dominant diffusing species then a crack can form as was seen in the Ru-island and Cr-island geometry's in this study. This happens because the growth interface is not at the thin-film/phase interface

Stellenbosch University https://scholar.sun.ac.za

meaning that as the thin film is consumed it separates from the phase. If several phases grow simultaneously as in the Ni-Si system the phases can also start to consume each other. In this situation it is not easy to draw conclusions on the diffusing species. Although Ni is reported as the dominant diffusing species in the metal rich and Si rich phases it is interesting that both the Ni-island and Si-island geometry show lateral formation of Ni_2Si [Zh-82]. From this it could be concluded that both Ni and Si diffuse readily through the phase.

3. The Si islands in the Cr-Si system and the Ni islands in the Ni-Si system shrink laterally indicating that the material is consumed from the edge of the island, while in the Pt-Al and Ru-Al systems the entire Al island is consumed and the island edge does not move. This gives information about the diffusion mechanism. Al is known to diffuse quickly along grain boundaries and interfaces in noble metal-aluminide systems [Co-90, De-97]. Diffusion of Ni through Ni_2Si and Si through $CrSi_2$ is via vacancies and defects. The latter two silicide systems do not have the very fast interfacial diffusion which enables the aluminide systems to supply Al to the reaction region from anywhere in the island without limiting the growth.

Stellenbosch University https://scholar.sun.ac.za

6. SUMMARY AND CONCLUSION

Instead of studying phase formation in conventional thin film binary diffusion couples, various unconventional thin film sample structures were used to investigate the influence of certain parameters on phase formation. Iron-silicide formation on Si(100) through metal alloy diffusion barriers (**chapter 3**), Ti-silicide formation on stressed Si(100) substrates (**chapter 4**) and phase formation in various lateral diffusion couples (**chapter 5**) was studied.

In **chapter 3** a variety of Fe-alloys were used as diffusion barriers (100 Å) through which Fe thin films (500 Å) reacted with Si(100). By decreasing the effective concentration of Fe at the growth interface it was hoped that the semiconducting $\beta FeSi_2$ phase could be formed directly. The barriers used were $Fe_{80}V_{20}$, $Fe_{30}V_{70}$, $Fe_{30}Ti_{70}$, $Fe_{30}Cr_{70}$ and $Fe_{30}Ni_{70}$. Some of these alloys ($Fe_{80}V_{20}$ and $Fe_{30}V_{70}$) were used as direct sources of Fe during Fe-Si interactions by depositing a thick (500 Å) film of the alloy onto a Si(100) substrate. Samples were also prepared with 500 Å of Fe deposited directly onto Si(100). In none of the samples did XRD ever show reflections from the metal alloyed with Fe. In some of the samples with excess Fe XRD did show Fe reflections when just the alloy was analysed. This indicates that a relatively stable phase forms between all these metals and Fe. Since no reflections other than Fe and Si were visible in the virgin samples it could be concluded that the co-deposited Fe-alloys which acted as diffusion barriers were amorphous.

In previous studies it has been shown that diffusion barriers can be used effectively to improve the quality of formed silicides and in some cases to increase the degree of epitaxiality. In some of these systems this was because the diffusion barrier affected the phase formation sequence (eg. Co-Si system with Ti diffusion barrier and Ni-Si system with NiZr diffusion barrier) [Pr-97], while in other cases it was ascribed to the way in which the diffusion barriers supplied the diffusing species to the reaction region (Fe-Si(111) system with Ni diffusion barrier) [Ky-94]. In the case of the Fe-Si system on Si(100) (this study) it was found that, while the diffusion barriers did improve the homogeneity of the formed silicides and also in some cases caused the formation of epitaxial silicides in combination with laser annealing, the phase formation sequence was not effected ($\varepsilon FeSi$ was the first phase see **Table 3.5**). The

Stellenbosch University https://scholar.sun.ac.za

effect of the diffusion barriers used in this study on the phase formation must therefore be solely due to the way in which Fe is supplied to the reaction region.

A number of different diffusion barriers were used between the Si(100) substrate and the Fe film. The diffusion barriers were always of the form of an Fe-M alloy where M was either Ni, V, Cr or Ti. Annealing the samples at 800°C for 10 minutes caused the formation of polycrystalline $\beta FeSi_2$. A second anneal at 800°C for 3 hours after the unused metals had been etched off still only showed the presence of polycrystalline $\beta FeSi_2$. The silicide formed in this way did however differ greatly from the samples where Fe reacted directly with Si(100). Even though no channelling was observed in the $\beta FeSi_2$ formed through the diffusion barriers the films were much more uniform (see **Fig. 3.8** and **3.13** to **3.15**) than those formed by reacting Fe directly with the Si(100) substrate (see **Fig. 3.9**).

Previous studies have shown that annealing a sample with a pulsed laser leads to improved epitaxial growth of silicides compared to conventional thermal annealing. It has also been shown that polycrystalline $\beta FeSi_2$ can be converted to epitaxial $Fe_{0.5}Si$[CsCl] on Si(111) substrates [Gr-92]. In this study, which was carried out on Si(100) substrates, it was found that the laser could be used to convert the already formed $\beta FeSi_2$ into epitaxial $Fe_{0.5}Si$[CsCl]. To our knowledge this is the first time that a continuous film of the metastable $Fe_{0.5}Si$[CsCl] has been formed epitaxially on Si(100). The samples in which the Fe reacted with the Si substrate through $Fe_{30}V_{70}$, $Fe_{30}Ni_{70}$ and $Fe_{30}Ti_{70}$ diffusion barriers, epitaxial $Fe_{0.5}Si$[CsCl] formed, while in the samples that used a $Fe_{30}Cr_{70}$ alloy as diffusion barrier the $Fe_{0.5}Si$[CsCl] showed no channelling and was therefore not epitaxial. Samples that were laser annealed without a second 800°C thermal anneal did not show any channelling irrespective of the diffusion barrier used. The second thermal anneal therefore improves the quality of the $\beta FeSi_2$ allowing the laser to transform it into epitaxial $Fe_{0.5}Si$[CsCl]. The diffusion barrier therefore influences not only the structure of the first phase but also all consequent phase formation. This can be seen under the optical microscope where the roughness of the $\beta FeSi_2$ and $Fe_{0.5}Si$[CsCl] films vary depending on the diffusion barrier used in the sample (see **Fig. 3.10** to **3.12**). Another interesting feature visible under the optical microscope is the cellular structure visible in all the samples that

Stellenbosch University https://scholar.sun.ac.za

form epitaxial $Fe_{0.5}Si$[CsCl] after laser annealing. The samples that do not form the cellular structure but have undergone the same energy density laser anneal (0.7 J/cm^2), form polycrystalline $Fe_{0.5}Si$[CsCl]. These cellular structures have been seen previously in laser annealed silicide systems [St-80]. The samples that formed the epitaxial silicide had the larger grain sizes (rougher texture). The cellular structures appeared only in those samples with larger grain sizes.

In **chapter 4** the effect of stress on Ti-silicide formation is reported. The stress is induced in the silicon by depositing either Si_3N_4 or SiO_2 onto the Back Side (BS) of the substrate. This back side film deforms the sample due to differences in thermal expansion coefficients. The deformation leads to strain and therefore stress throughout the substrate. The curvature of the samples was measured using a reflecting laser technique at room temperature before and after the Back Side (BS) deposition. The stress was then calculated from the curvature values using Stoney's equation (see **Appendix A** equation A.5). The curvature was also measured and the stress calculated after the Ti thin film, which was to react with the silicon, was deposited on the front side of the substrate. The samples with Si_3N_4 deposited on the back side all had relatively large tensile stresses in the back side film after deposition while those with SiO_2 deposited onto the back side had relatively large compressive stresses in the back side film. The stress was also calculated in the the Si substrate before and after the Ti film was deposited. As the substrate was much thicker than the back side films the stress in the substrates was much smaller (see **Appendix A**). The samples which had Si_3N_4 deposited (400 and 200 nm) onto the BS had tensile stresses in the Front Side (FS) of the Si wafer before the Ti deposition, while those that had SiO_2 deposited onto the BS (200 and 400 nm) had compressive stress in the FS of the wafer before Ti deposition. These samples were then heated for various times at temperatures ranging from 450 °C to 650 °C to induce Titanium-silicide formation. The phase formation and kinetics was studied using XRD and RBS. It was found that the samples with Si_3N_4 on the BS formed the $TiSi_2$(C49) phase below 650 °C. Above this temperature the $TiSi_2$(C54) phase formed. There was no marked difference in the $TiSi_2$(C49) kinetics in the two sets of samples. Of the two sets of samples with SiO_2 on the BS the 400 nm samples formed the $TiSi_2$(C49). The Arrhenius plot of this phase showed that the activation energy was within error the same as that of the $TiSi_2$ formed in the samples with Si_3N_4 deposited onto the BS (2.1eV). The reaction rate of the $TiSi_2$(C49)

Stellenbosch University https://scholar.sun.ac.za

formed in the BS:400 nm SiO_2 samples was about half that of the samples with Si_3N_4 deposited onto the BS. The compressive stress in the substrate therefore causes slower silicide formation. The fact that the activation energy stays the same indicates that the reaction mechanism does not change. The $TiSi_2$ was found to form with diffusion limited or non-linear kinetics for all three these sample groups. The fourth sample group with 200nm of SiO_2 deposited on the BS did not form the di-silicide but rather the Ti-rich Ti_5Si_3 phase at the same temperatures. The activation energy was 1.9eV and the reaction rate was slower than that of the $TiSi_2$ phase.

Cheng et. al. [Ch-99] also found that compressive stress in the substrate slowed the formation of $TiSi_2$ and tensile stress speeded it up. They argued that this slowing of reaction rate was because the compressive stress decreased the amount of vacancies in the growing silicide film and thus limited the diffusion. Tensile stress on the other hand speeded up the reaction because this led to the creation of extra vacancies and therefore enhanced diffusion. This interpretation is supported by previous work done by Botha et. al. [Bo-82] in which he showed that $TiSi_2$ grows by a silicon vacancy diffusion mechanism with a high mobility of silicon. The fact that the BS:200 nm SiO_2 samples formed the Ti_5Si_3 phase rather than $TiSi_2$ can be explained according to the EHF model. The EHF model predicts that because $TiSi_2$ forms as first phase the effective concentration at the reaction interface is on the Si-rich side of the phase diagram making $TiSi_2$ the thermodynamically more viable phase. As the number of vacancies decrease the silicon supply to the reaction interface is limited and this moves the effective concentration toward the Ti-rich side of the phase diagram where Ti_5Si_3 formation is thermodynamically prefered (see EHF diagram **Fig. 4.1**).

The third type of sample structure studied in this work were lateral diffusion couples. In **chapter 5** phase formation is studied in Ru-Al, Pt-Al and Cr-Si lateral diffusion couples. This chapter also contains a summary of all published lateral diffusion work as well as results obtained through private communications. A typical lateral diffusion couple consists of an island of one material on a thin film of another. After annealing reaction takes place and phases start to form laterally, growing away from the island. Lateral diffusion couples can give useful information concerning three major aspects of solid state interactions.

Stellenbosch University https://scholar.sun.ac.za

1. They can be used to study the transition between thin film and bulk diffusion. A good example of this is to determine the critical thickness that a phase grows before another phase begins to form. The EHF model forecasts that this would happen when the effective concentration at the reaction interface changes due to the long diffusion path that the diffusing species has to travel. As the diffusing species becomes limited the effective concentration is moved to a region in the EHF diagram where another phase becomes thermodynamically favoured.
2. Information can be obtained about the diffusing species. In the Ru-Al and Pt-Al systems it can clearly be seen that the Al moves out from the island into the reaction region while there is no net movement of either Pt or Ru indicating that Al is the dominant diffusing species. There is no lateral reaction in either of the systems when the island consists of the noble metal.
3. The Si island in the Cr-Si and the Ni island Ni-Si system shrink laterally during phase formation indicating that material is sourced to the reaction region from the edge of the islands while in the Pt and Ru-Al systems the entire Al island is consumed and the island edge does not move. This gives information about the diffusion mechanism. Al is well known to diffuse quickly along grain boundaries in noble-metal-aluminide systems [Co-90, De-97]. Diffusion of Ni through Ni_2Si and Si through $CrSi_2$ is via vacancies and defects. The latter two silicide systems do not have the very fast interfacial diffusion which enables the aluminide systems to supply Al to the reaction region from anywhere in the island without limiting the growth.

In the Ru-Al thin film system it was found that when Ru is in excess then $RuAl_2$ and Ru_2Al_3 will be the first phases to form. If on the other hand Al is in excess then $RuAl_6$ is the first phase to form followed by $RuAl_2$ and Ru_4Al_{13}. In the Al-island Ru-Al lateral diffusion couples $RuAl_6$ formed under the island and only the Ru_4Al_{13} phase grew laterally at 550 °C indicating that at 50 μm the phase had not yet reached the critical thickness. Although the Al island formed the characteristic voids the lateral grown phase was uniform in thickness and composition and grew linearly indicating reaction limited kinetics (see **Fig. 5.9**). The fact that the Ru_4Al_{13} phase grows with reaction limited kinetics explains why it has not reached its critical thickness. The EHF model predicts that if the phase grows with diffusion limited kinetics it will

Stellenbosch University https://scholar.sun.ac.za

reach a critical thickness where the effective Al concentration will drop enough to thermodynamically favour a more Ru-rich phase. In this case the diffusion length does not effect the availability of Al and therefore the Ru_4Al_{13} continues growing without other phases forming. In the Ru-island geometry there was no lateral reaction but the Al was consumed in a region around the Ru-islands.

In the Pt-Al system the Al islands reacted laterally and three phases grew simultaneously namely, Pt_5Al_{21}, Pt_8Al_{21} and $PtAl_2$. Of these three phases only the $PtAl_2$ phase is found in conventional thin film systems where Pt_2Al_3 is usually found as first phase. The Pt_5Al_{21} phase formed under the Al island and the other two phases grew laterally. These two phases grew non-linearly indicating diffusion limited kinetics (see **Fig. 5.16**). All three these phases have very similar EHF values on the Al-rich side of the phase diagram where the liquidus minimun is situated which means that thermodynamically all three phases are equally likely to form and this explains why all three phases grew simultaneously. Even if one of the phases were to nucleate first as it grows with diffusion limited kinetics it would only grow to a relatively small lateral thickness before the critical thickness is reached allowing the next phase to nucleate and grow.

Oxidation was a big problem in the study of the Cr-Si system. Both Cr and Si oxidized in the vacuum furnace at 600 °C. This is not strange for Cr but crystalline Si does not usually oxidize at 600 °C and 10^{-7} Torr. The thin film and islands in the lateral diffusion couples were deposited at room temperature in an e-beam system. Such Si films are amorphous and porous and are known to react much faster with oxygen due to the lower binding energy than crystalline Si and the large reactive surface area due to porosity [Ad-89]. It is also possible that small amounts of Cr diffusion into the Si could break the Si-Si bonds making it energetically more viable for these Si atoms to react with oxygen. It has been found that Si dissolved in metals like Au and Ag is more reactive with oxygen than Si bound in a crystalline substrate [Ju-99]. This has also been found in previous studies where amorphous Si reacted faster and at lower temperature through gold to form SiO_2 than crystalline Si [Ju-99]. The Cr-island geometry showed no lateral reaction. There was a region of depleted Si forming a crack or void around the island indicating that the Si had diffused into the Cr-island. In the Si-island geometry $CrSi_2$ grew laterally. This is also the first phase in

Stellenbosch University https://scholar.sun.ac.za

thin film diffusion couples. No kinetics could be measured due to the excessive oxidation in the system. The amount of reaction was not reproducible. In most annealed samples there was no lateral reaction. Different caps were used to study their ability to limit oxidation. Hf was found to be the most effective, probably due to its higher affinity for oxygen than Cr and was therefore able to act as a gettering site for the oxygen. Caps have also been shown to improve silicide formation in the Co-Si [Tu-95] and Ti-Si (see **chapter 4**) systems.

Stellenbosch University https://scholar.sun.ac.za

Appendix A Stress calculations in thin films using Stoney's equation

Biaxial stress in thin films

When a thin film is deposited onto a planar substrate the stress in the thin film due to differences in thermal expansion is biaxial with both components in the plane of the film. There is no stress in the direction normal to the plane, and yet there is strain in the direction normal to the film. In a three dimensional isotropic system the stress σ and the strain ε are related to each other by the following equations.

$$\begin{aligned} \varepsilon_x &= \frac{1}{Y}\left[\sigma_x - \nu\left(\sigma_y + \sigma_z\right)\right] \\ \varepsilon_y &= \frac{1}{Y}\left[\sigma_y - \nu\left(\sigma_x + \sigma_z\right)\right] \\ \varepsilon_z &= \frac{1}{Y}\left[\sigma_z - \nu\left(\sigma_x + \sigma_y\right)\right] \end{aligned} \qquad \text{(A.1)}$$

Where Y and ν are the Young's modulus and Poisson's ratio respectively. In thin film systems which do not have a stress component in the direction normal to the plane (z-direction) the equations simplify to the following.

$$\begin{aligned} \varepsilon_x &= \frac{1}{Y}\left(\sigma_x - \nu\sigma_y\right) \\ \varepsilon_y &= \frac{1}{Y}\left(\sigma_y - \nu\sigma_x\right) \\ \varepsilon_z &= \frac{-\nu}{Y}\left(\sigma_x + \sigma_y\right) \end{aligned} \qquad \text{(A.2)}$$

From these equations we have

$$\varepsilon_x + \varepsilon_y = \frac{1-\nu}{Y}\left(\sigma_x + \sigma_y\right) \qquad \text{(A.3)}$$

If a thin film of Al were deposited onto a Si wafer at liquid nitrogen temperature and then allowed to reach room temperature then the wafer would bend because Al has a larger thermal expansion coefficient than silicon. Assuming good adhesion the Al thin film is constrained by the substrate and will be compressed. **Fig. A.1** shows a schematic of the cross section through such a curved sample. The following derivation assumes that the thin film thickness t_f is much less than that of the substrate t_s, so that the neutral plane where there is no stress can be taken in the middle of the substrate. **Fig. A.1(b)** shows the stress distribution in the thin film and substrate and the corresponding forces and moments. At equilibrium the moment produced by the stress in the film must be equal to that produced by the stress in the substrate. Since the film

Stellenbosch University https://scholar.sun.ac.za

is very thin the tress σ_f is uniform across the film thickness. The moment M_f (force times perpendicular distance) due to the force in the thin film with respect to the neutral plane is

$$M_f = \sigma_f W t_f \frac{t_{Si}}{2}$$

where W is the width of the film and t_f is the thickness of the film.

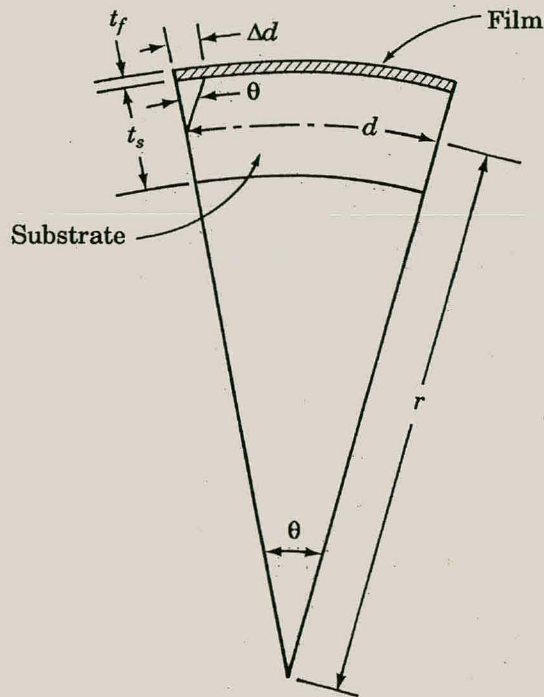

(a)

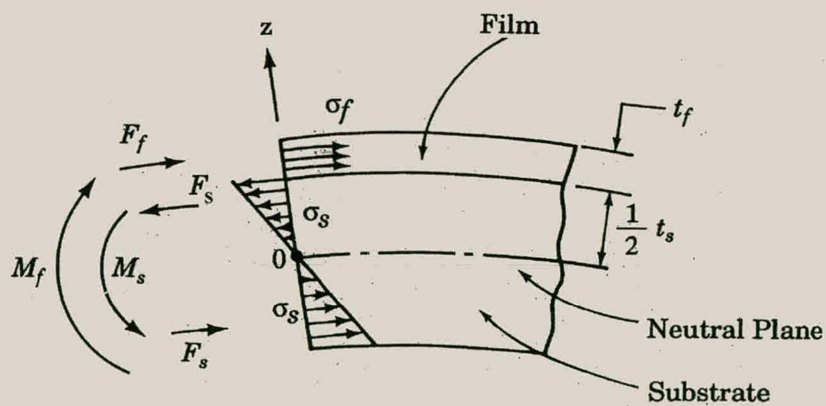

(b)

Fig. A.1 (a) Cross sectional view of a thin film under compressive stress on a bent substrate. (b) A schematic showing the stress distribution in the film and substrate and the corresponding forces and moments.

Stellenbosch University https://scholar.sun.ac.za

To calculate the moment in the substrate the following geometrical relations can be derived.

$$\frac{d}{r} = \frac{\Delta d}{\left(\frac{t_{Si}}{2}\right)}$$

therefore

$$\frac{1}{r} = \frac{\Delta d}{\left(\frac{t_{Si} d}{2}\right)} = \frac{\varepsilon_{max}}{\left(\frac{t_{Si}}{2}\right)}$$

Where r is the radius of curvature of the substrate measured to the neutral plane, d is an arbitrary length of the substrate measured at the neutral plane and $\Delta d/d = \varepsilon_{max}$ is the strain measured at the outer surface of the substrate. In the substrate the stress and therefore the strain is zero at the neutral plane. The strain increases linearly with distance z measured from the neutral plane (i.e. it obeys Hookes law and increases linearly with stress) so that

$$\frac{\varepsilon_{Si}(z)}{z} = \frac{\varepsilon_{max}}{\left(\frac{t_{Si}}{2}\right)} = \frac{1}{r}$$

where $\varepsilon_{Si}(z)$ is the strain in a plane parallel to and at a distance z from the neutral plane. By assuming biaxial stress in the substrate (equation A.3) the following equation gives

$$\sigma_{Si}(z) = \left(\frac{Y}{1-\nu}\right)_{Si} \varepsilon_{Si}(z) = \left(\frac{Y}{1-\nu}\right)_{Si} \frac{z}{r} \qquad \text{(A.4)}$$

the stress in the substrate as a function of distance z from the neutral plane. Using A.4 one can determine the moment produced by the stress in the substrate.

$$M_{Si} = W \int_{-t_{Si}/2}^{t_{Si}/2} z\sigma_{Si}(z)dz = W \int_{-t_{Si}/2}^{t_{Si}/2} \left(\frac{Y}{1-\nu}\right)_{Si} \frac{z^2}{r} dz$$

$$= \left(\frac{Y}{1-\nu}\right)_{Si} \frac{W t_{Si}^3}{12r}$$

In equilibrium $M_f = M_{Si}$ which gives Stoney's equation,

$$\sigma_f = \left(\frac{Y}{1-\nu}\right)_{Si} \frac{t_{Si}^2}{6 r t_f} \qquad \text{(A.5)}$$

Stellenbosch University https://scholar.sun.ac.za

This equation shows that by measuring the curvature and thicknesses of the film and substrate the biaxial stress in the film can be calculated. In this study the curvature was measured by a reflected laser technique. Usually the undeposited wafer is not completely flat. For this reason the change in radius is taken into consideration and equation A.4 and A.5 (Stoney's equation) take the form

$$\sigma_f = \left(\frac{Y}{1-\nu}\right)_{Si} \frac{t_{Si}^2}{6t_f}\left(\frac{1}{r}-\frac{1}{r_0}\right) \quad (A.6)$$

$$\sigma_{Si}(z) = \left(\frac{Y}{1-\nu}\right)_{Si}\left(\frac{1}{r}-\frac{1}{r_0}\right)z \quad (A.7)$$

where r_0 is the radius before the film is deposited and r the radius after. In our experimental setup we measured the bow b of the sample (see **Fig. 2.9**). The bow can be related to the radius by

$$r = \frac{L^2}{8b}$$

This means that if b_0 is the bow before deposition and b is the bow after deposition then

$$\left(\frac{1}{r}-\frac{1}{r_0}\right) = \frac{1}{r_{eff}} = \frac{8}{L^2}\Delta b \quad (A.8)$$

with $\Delta b = b - b_0$. **Tables A.1** and **A.2** show the result of the bow measurements on the set of samples used in this study. The values used for the Youngs modulus (Y) and the Poisson ratio (ν) for Si were 160 GPa and 0.28 respectively (see **Appendix D**). The final column is the stress calculated at the surface of the sample where the Ti film is deposited using equation A.4.

Table A.1 Stress measurement results for the different samples used in this study after the BS deposition. The final column is the stress σ_S calculated at the surface of the substrate.

Sample	BS film	Δb (μm)	r_{eff} (m)	σ_f (MPa)	σ_S (Mpa)
A	400nmSi_3N_4	91.88	24.79	1459	2.78
B	200nmSi_3N_4	42.38	53.75	1345	1.28
C	400nmSiO_2	-24.28	-93.82	-385	-0.73
D	200nmSiO_2	-13.83	-164.72	-439	-0.42

Stellenbosch University https://scholar.sun.ac.za

Table A.2 Stress measurement results for the different samples used in this study after the FS deposition. The final column is the stress σ_S calculated at the surface of the substrate.

Sample	BS film	Δb (μm)	r_{eff} (m)	σ_f (MPa)	σ_S (Mpa)
A	400nmSi_3N_4	2.11	1080	33.2	0.06
B	200nmSi_3N_4	3.11	733	97.9	0.09
C	400nmSiO_2	-0.52	-4381	-8.2	-0.02
D	200nmSiO_2	1.5	1518	47.3	0.05

Stellenbosch University https://scholar.sun.ac.za

Appendix B X-ray and Crystallographic data of phases

Table B.1 Crystal parameters of different Ti-silicide and oxide phases.

Compound	Crystal system	Space group	Prototype	Lattice constants (Å)		
				a	b	c
Si	Cubic	Fd 3m	C	5.4		
αTi	Hexagonal	$P6_3/mmc$	Mg	2.950		4.686
Ti_5Si_3	Hexagonal	$P6_3/mmc$	Mn_5Si_3	7.444		5.143
Ti_5Si_4	Tetragonal	$P4_12_12$	Zr_5Si_4	6.713		12.190
Ti_5Si_4(HT)	Orthorhombic	Pcnm	Ge_4Sm_5	6.645	6.506	12.69
TiSi	Orthorhombic	Pcnma	FeB	6.544	3.638	4.997
$TiSi_2$(C49)	Orthorhombic	Cmcm	$ZrSi_2$	3.62	13.76	3.85
$TiSi_2$(C54)	Orthorhombic	Fddd	$TiSi_2$	8.27	8.55	4.80
Ti_6O	Hexagonal	P31c		5.14	5.14	9.48

Table B.2 Characteristic lines used for phase identification in the Ti-silicide system. If the phase was not detected in this study the two or three strongest powder diffraction lines are quoted.

Phase	Strong lines in 2θ	hkl values	Intensity in powder (%)
Ti	40.17	101	100
	38.42	002	30
Ti_5Si_3	40.1	211	100
	42.7	112	60
	34.9	002	10
Ti_5Si_4	37.2	213	100
	38.6	221	100
	41.7	115	100
	43.1	302	100
TiSi	36.9	210	100
	46.2	112	85
$TiSi_2$(C49)	41.2	150	15
$TiSi_2$(C54)	30.0	220	10
	39.1	311	100
	42.2	040	43
	49.7	331	45
Ti_6O	39.9	-1-12	100

Stellenbosch University https://scholar.sun.ac.za

Table B.3 Crystal parameters of different Ru-aluminide phases.

Compound	Crystal system	Space group	Prototype	Lattice constants (Å)		
				a	b	c
Ru	Hexagonal	$P6_3/mmc$	Mg	2.706		4.282
Al	Cubic	Fm3m	Cu	4.049		
$RuAl_6$	Orthorhombic	Cmcm		7.467	6.556	8.961
Ru_4AL_{13}	Monoclinic	C2/m		15.862	8.188	12.736
$RuAl_2$	Orthorhombic	Fddd	$TiSi_2$	8.012	4.717	8.785
Ru_2Al_3	Tetragonal	14/mmm	Al_3Os_2	3.079		14.33
RuAl	Cubic	Pm3m	CsCl	2.95		

Table B.4 Characteristic lines used for phase identification in the Ru-aluminide system. If the phase was not detected in this study the two or three strongest powder diffraction lines are quoted.

Phase	Strong lines in 2θ	hkl values	Intensity in powder (%)
Ru	38.4	100	40
	44.0	101	100
	69.5	110	25
	78.5	103	25
Al	38.6	111	100
	78.3	311	24
$RuAl_6$	56	314	8
Ru_4Al_{13}	24.7	-220	100
	26.9	221	100
$RuAl_2$	30.2	202	60
	57.1	115	10
Ru_2Al_3	43.1	105	100
RuAl	30.29	100	55
	43.4	110	100

Stellenbosch University https://scholar.sun.ac.za

Table B.5 Crystal parameters of different Fe-silicides.

Compound	Crystal system	Space group	Prototype	Lattice constants (Å)		
				a	b	c
Si	Cubic	Fd 3m	C	5.4		
αFe	Cubic	Im3m		2.8664		
Fe_3Si	Cubic	Im3m	W	2.841(5)		
Fe_2Si	Cubic	Pm3m	CsCl	2.81		
Fe_5Si_3	Hexagonal	$P6_3/mcm$	Mn_5Si_3	6.759(5)		4.720(5)
εFeSi	Cubic	$P2_13$		4.48798		
FeSi[CsCl]	Cubic	Fm 3m	CsCl	2.7		
$\alpha FeSi_2$	Tetragonal	P4/mmm		2.69392		5.1361
$\beta FeSi_2$	Orthorhombic		$FeSi_2$	9.879	7.799	7.839
$\gamma FeSi_2$	Cubic	Fm 3m	CaF_2	5.4		
$Fe_{0.5}Si$[CsCl]	Cubic	Fm 3m	CsCl	2.7		

Stellenbosch University https://scholar.sun.ac.za

Appendix C Standard Mössbauer parameters of Fe-silicide phases

Table C.1 Mössbauer parameters of the stable and metastable Fe-silicides. Isomer shifts, δ, are quoted relative to αFe. H is the hyperfine field and ΔE_Q is the quadrupole splitting.

Phase	H(T)	δ(**mm/s**)	ΔE_Q**(mm/s)**	**Reference**
εFe	-33.2(1)	-0.87 ✪	0	[Ma-95]
		+0.87 ✪	0	
εFiSi	0	0.26(1)	0.51(2)	[Ma-95]
FeSi[CsCl]	0	0.26	0	[Ma-95]
$\beta FeSi_2$	0	0.076	0.525	[Fa-95]
	0	0.091	-0.315	
$Fe_{0.5}Si$[CsCl]	0	0.15(1)	0.59(1)	[Ro-96]
$Fe_{0.5}Si$[CsCl]	0	0.198	0.589	[De-95]
$\gamma FeSi_2[CaF_2]$	The cubic symmetry of this hypothetical phase would give rise to a singlet			
$\alpha FeSi_2$	0	0.23(2)	0.47(2)	[Ma-95]
	0	0.26(2)	0.7(2)	

✪ The –33.2T internal magnetic field can be simulated by a series of singlets of which the inner two are situated symmetrically around a defined zero reference point at a position of 0.87mm/s.

Stellenbosch University https://scholar.sun.ac.za

Appendix D Mechanical properties of some materials

Table D.1 Modulus of elasticity (Young's modulus), Poisson's ratio and coefficient of thermal expansion for some materials.

Material	Modulus of elasticity (GPa)	Poisson's ratio	Coefficient of thermal expansion ($10^{-6}/^{o}C$)
Al and Al-alloys	69	0.33	23.6
Cr	248		
Cu	110	0.34	17.0
Au	78	0.42	14.2
Fe	208		
Mo	320		4.9
Ni and Ni-alloys	207	0.31	12.9-13.3
Pt	172	0.39	9.5
Rh	319		
Ti and Ti-alloys	104-116	0.34	7.6-9.8
Al_2O_3	393	0.22	6.5-7.6
Diamond	1035	0.10-0.29	0.8
Silica, fused	73	0.165	0.4
SiO_2, thermally grown	84	0.17	0.6
Si<100> direction	160	0.28	2.5
Si_3N_4	200	0.22	2.7-3.7
$MgAl_2O_4$	260		7.6-8.8
Nylon 6,6	1.58-3.79	0.39	144
Polyvinyl chloride (PVC)	2.4-4.1	0.38	90-180

Stellenbosch University https://scholar.sun.ac.za

References

[Ad-89] D. Adams, Laser induced epitaxy of deposited amorphous silicon thin films. M.Sc. thesis, University of Western Cape, South Africa (1989).

[Ba-94] P. Baeri, Pulsed laser induced modification of metal silicide layers, Thin Solid Films. 241(1994)142.

[Be-82] R. W. Bene`, First phase nucleation rule for solid-state nucleation in metal-metal thin-film systems, Appl. Phys. Lett. 41(1982)529.

[Bl-92] B. Blanpain, Lateral diffusion couples and their contribution to understanding thin film reactions, Crucial Issues in Semiconductor Materials and Processing Technologies. (Kluwer academic publishers) 222(1992)421.

[Bl-99] B. Blanpain, Private communication.

[Bo-82] A. P. Botha and R. Pretorius, $CoSi_2$, $ZrSi_2$ and $TiSi_2$ formation studied by a radioactive ^{31}Si marker technique, Thin Solid Films 93 (1982) 127.

[Ch-78] W. K. Chu, J. W. Mayer and M. Nicolet, Backscattering Spectrometry, (Academic Press, New York), (1978).

[Ch-84] S. H. Chen, L. R. Zheng, J. C. Barbour, E. C. Zingu, L. S. Hung, C. B. Carter and J. W. Mayer, Lateral diffusion couples studied by transmission electron microscopy, Materials Letters 2(1984)469.

[Ch-85] H. C. Cheng. T. R. Yew and L. J. Chen, Epitaxial growth of $FeSi_2$ in Fe thin films on Si with a thin interposing Ni layer, Appl. Phys. Lett. 47(1985)128.

[Ch-85] S. H. Cheng, L. R. Zheng, C. B. Carter and J. W. Mayer, Transmission electron microscopy studies on the lateral growth of nickel silicides, J. Appl. Phys. 57(1985)258.

[Ch-93] J. Chevrier, P. Stocker, V. Le Thanh, J. M. Gay and J. Derrien, Epitaxial growth of alpha-$FeSi_2$ on Si(111) at low temperatures, Europhys. Lett. 2(1993)449.

Stellenbosch University https://scholar.sun.ac.za

[Ch-99] S. L. Cheng, H. Y. Huang, Y. C. Peng, L. J. Chen, B. Y. Tsui, C. J. Tsai, S. S. Guo, Y. R. Yang and J. T. Lin, Effects of stress on the growth of $TiSi_2$ thin films on (001)Si, Appl. Phys. Lett. 74(1999)1406.

[Cl-92] L. A. Clevenger, J. M. E. Harper, C. Cabral, C. Nobili, G. Ottaviani and R. Mann, Kinetic analysis of C49-$TiSi_2$ and C54-$TiSi_2$ formation at rapid thermal annealing rates, J. Appl. Phys. 72(1992)4978.

[Co-87] E. G. Colgan, Phase formation and dissociation in the thin film Pt/Al system, J. Appl. Phys. 62(1987)1224.

[Co-90] E. G. Colgan, A review of thin-film aluminide formation, Materials Science Reports 5(1990)1.

[Co-94] E. G. Colgan, L. A. Clevenger and C. Cabral, Activation energy for C49 and C54 TiSi2 formation measured during rapid thermal annealing, Appl. Phys. Lett. 65(1994)2009.

[De-88] F. R. de Boer, R. Boom, W. C. M. Mattens, A. R. Miedema and A. K. Niessen, Cohesion in metals, North Holland Publishers (1988).

[De-90] R. de Reus, H. C. Tissink and F. W. Saris, Low temperature epitaxial $NiSi_2$ formation on Si(111) by diffusing Ni through amorphous Ni-Zr, J. Mater. Res. 5(1990)341.

[De-95] J. Desimoni, F. H. Sanchez, M. B. Fernandez van Raap, H. Bernas, C. Clerc and X. W. Lin, Mossbauer characterisation of $\gamma FeSi_2$ precipitates in Si(100), Phys. Rev. B. 51(1995)86.

[De-97] H. S. de Waal, R. Pretorius, V. M. Prozesky, C. L. Churms, The study of voids in the Au-Al thin-film system using the nuclear microprobe, Nucl. Instr. and Meth. B130(1997)722

[Di-94] P. J. Ding, R. Talevi, W. A. Lanford, S. Hymes and S. P. Murarka, Use of a rastered microbeam to study lateral diffusion of interest to microelectronics, Nucl. Instr. and Meth. B 85(1994)167.

Stellenbosch University https://scholar.sun.ac.za

[Do-85] L. R. Doolittle, Algorithm for the rapid simulation of Rutherford backscattering spectra, Nucl. Instr. and Meth. B9(1985)344.

[Ei-83] N. M. Einspruch and G. B. Larrebee, VLSI Electronics Microstructure Science volume 6, Academic press (1983).

[Fa-95] M. Fanciulli, C. Rosenblad, G. Weyer, A. Svane and N. E. Christensen, Conversion Electron Mossbauer Spectroscopy study of epitaxial beta-$FeSi_2$ grown by molecular beam epitaxy, Phys. Rev. Lett. 75(1995)1642.

[Ge-91] K. M. Geib, John E. Mahan, Robert G. Long, Menachem Nathan and G. Bai, Epitaxial orientation and morphology of $\beta FeSi_2$ on (001) silicon, J. Appl. Phys. 70(1991)1730.

[Gr-92] M. G. Grimaldi, P. Baeri, C. Spinella and S. Lagomarsino, Liquid phase epitaxy of cubic $FeSi_2$ on Si(111) induced by pulsed laser, Appl. Phys. Lett. 60(1992)1132.

[Ha-99] A. Habanyama, C. Comrie, private comunications.

[Hs-91] S. L. Hsia, T. Y. Tan, P. Smith and G. E. McGuire, Formation of epitaxial $CoSi_2$ films on (001) silicon using Ti-Co alloy and bimetal source materials, J. Appl. Phys. 70(1991)7579.

[Hu-83] L. S. Hung, J. Gyulai and J. W. Mayer, Kinetics of $TiSi_2$ formation by thin Ti films on Si, J. Appl. Phys. 54 (1983) 5075.

[Ju-99] B. A. Julies, Head of the Electron Microscope Unit at the University of the Western Cape, South Africa, Private correspondence (1999).

[Ku-79] O. Kubaschewski and C. B. Alcock, Metallurgical Thermochemistry (Pergamon press, Oxford), (1979)268.

[Ky-94] K. Kyllebek Larsen, A. Lauwers, K. Maex and M. Van Rossum, Formation of β and $\alpha FeSi_2$ films on (100) silicon using Fe-Si and Fe-Ti-Si diffusion couples, Materials Research Society Symposium Proceedings vol. 320(1994)85.

Stellenbosch University https://scholar.sun.ac.za

[La-91] M. L. A. Dass, D B. Fraser, Chih-Shih Wei, Growth of epitaxial $CoSi_2$ on (100)Si, Appl. Phys. Lett. 58(1991)1308.

[Li-88] Joyce C. Liu, J. W. Mayer and J. C. Barbour, Kinetics of $NiAl_3$ and Ni_2Al_3 phase growth on lateral diffusion couples, J. Appl. Phys. 64(1988)656.

[Liu-88] Joyce C. Liu, J. W. Mayer and J. C. Barbour, Phase formation of $NiAl_3$ in lateral diffusion couples, J. Appl. Phys. 64(1988)651.

[Ma-95] K. Maex and M. Van Rossum, Properties of metal silicides, emis datareviews series no. 14 IEEE 1995.

[Ma-96] R. L. Maltez, L. Amaral, M. Behar, A. Vantomme, G. Langouche and X. W. Lin, Mossbauer study of the magnetic character and ordering process of the cubic $\gamma FeSi_2$ phase obtained by Fe implantation into a Si(100) matrix, Phys. Rev. B. 54(1996)11659.

[Mi-95] L. Miglio, F. Tavazza and G. Malegori, Stability hierarchy of the pseudomorphic $FeSi_2$ phases: α, γ and defected CsCl, Appl. Phys. Lett. 67(1995)2293.

[Ne-97] R. Nemutudi, Study of Pt-Ge interaction using thin film and lateral diffusion couples, MSc thesis University of Cape Town, South Africa (1997).

[Ni-83] M. A Nicolet and S. S. Lau, Formation and characterization of transition-metal silicides, in materials and process characterization. Edited by N. G. Einspruch and G. B. Larrabee (Academic Press, New York) (1983) 329.

[On-93] N. Onda, H. Sirringhaus, S. Goncalves-Conto, C. Schwarz, E. Muller-Gubler and H. von Kanel, MRS. Proc. 280(1993)581.

[Pi-88] C. A. Pico and M. G. Lagally, Kinetics of titanium silicide formation on single crystal Si, J. Appl. Phys. 64 (1988) 4957.

[Pr-84] R. Pretorius, Prediction of silicide first phase and phase sequence from heats of formation, MRS Proc, 25(1984)15.

Stellenbosch University https://scholar.sun.ac.za

[Pr-93] R. Pretorius, T. K. Marais and C. C. Theron, Thin film compound phase formation sequence: An effective heat of formation model, A review, Materials Science and Engineering, 10(1993)1.

[Pr-97] R. Pretorius and J. W. Mayer, Silicide formation by concentration controlled phase selection, J. Appl. Phys. 8(1997)2448.

[Pr-99] R. Pretorius, Private communication.

[Re-92] H. Reuther, E. Wieser, D. Panknin, R. Grotzschel, W. Skorupa and G. Querner, Investigation of ion beam synthesised iron silicide by RBS, XRD and Mossbauer spectroscopy, Nucl. Instr. and Meth. B68 (1992)241-244.

[Ro-96] C. Rosenblad, A Mössbauer investigation of iron-silicide phases formed on silicon by molecular beam epitax, pulsed laser deposition and solid state interactions, M.Sc. thesis University of Aarhus, Denmark (1996).

[St-80] W. T. Stacy, G. J. Van Gurp, G. E. J. Eggermont, V. Tammingo and J. R. M. Giysbers, The microstructure of laser-irradiated metal-silicon systems, Proceedings of the symposium on thin film interfaces and interactions, The Electrochemical Society, (1980)442.

[Th-97] C. C. Theron, *In situ* real time characterization of solid state reaction in thin films, PhD thesis, University of Stellenbosch (1997).

[Th-98] C. C. Theron, J, A, Mars, C. L. Churms, J. Farmer and R. Pretorius, In-Situ, Real-Time RBS measurement of solid-state reaction in thin-films, Nucl. Instr. and Meth. B 139(1998)213.

[Ts-81] B. Y. Tsaur, S. S. Lau, J. W. Mayer and M. A. Nicolet, Sequence of phase formation in planar metal-Si reaction couples, Appl. Phys. Lett. 38(1981)922.

[Tu-92] King-Ning Tu, J. W. Mayer, L. C. Feldman, Electronic Thin Film Science for Electrical Engineers and Material Scientists, (Macmillan Publishing Company, New York) 330.

[Tu-95] R. T. Tung and F. Schrey, Increased uniformity and thermal stability of $CoSi_2$ thin films by Ti capping, Appl. Phys. Lett. 67(1995)2164.

Stellenbosch University https://scholar.sun.ac.za

[Va-99] Private comunications, A. Vantomme, Katholieke Universiteit Leuven.

[Vo-92] H. von Kanel, K. A. Mayer, E. Muller, N. Omda and H. Sirringhaus, Structural and electronic properties of meta-stable epitaxial FeSi films on Si(111), Phys. Rev. B 45 (1992)13807.

[Vo-94] H. Von Kanel, U. Kafader, P. Sutter, N. Onda, H. Sirringhaus, E. Muller, U. Kroll, C. Schwarz and S. Goncalves-Conto, Epitaxial semiconducting and metallic iron silicides, MRS proceedings, vol. 320 (1994)73

[Vo-95] H. Von Kanel, N. Onda and L. Miglio, Heteroepitaxy in science and technology of thin films (World Science) 1995.

[Wa-76] R. M. Walser, R. W. Bene', First phase nucleation in silicon-transition-metal planar interfaces, Appl. Phys. Lett. 28(1976)624.

[Wa-95] S. Q. Wang, S. Hong, A, White, C. Hoener and J. W. Mayer, Interfacial reactions in the SiO_2/Ru and SiO_2/Ru/Al-Si structures, J. Appl. Phys. 77(1995)5751.

[Zh-82] L. R. Zheng, L. S. Hung, J. W. Mayer, G. Majini and G. O. Havioni, Lateral diffusion of Ni and Si through Ni_2Si in Ni/Si couples, Appl. Phys. Lett. 41 (1982) 646.

[Zh-83] L. R. Zheng, L. S. Hung and J. W. Mayer, Silicide formation in lateral diffusion couples, J. Vac. Sci. Technol. A 1(1983)758.

[Zhe-83] L. R. Zheng, L. S. Hung and J. W. Mayer, Lateral diffusion of platinum through Pt_2Si in Pt/Si couples, Thin Solid Films, 104(1983)207.